ISSN number 0971 - 9709

The Journal of Indian Geophysical Union

AN OPEN ACCESS BIMONTHLY JOURNAL OF IGU

VOLUME 26, ISSUE 1, January 2022

EDITORIAL OFFICE

Indian Geophysical Union, NGRI Campus, Uppal Road, Hyderabad- 500 007
Telephone: 91-4027012739, 27012332; Telefax:+91-04-27171564
Email: jigu1963@gmail.com, website: http://iguonline.in/journal/

The Journal with six issues in a year publishes articles covering
Solid Earth Geosciences; Marine Geosciences; and Atmospheric, Space and Planetary Sciences.

Annual Subscription

Individual Rs -1000/- per issue and Institutional Rs- 5000/- for six issues
Payments should be sent by DD drawn in favour of "The Treasurer, Indian Geophysical Union", payable at Hyderabad,
Money Transfer/NEFT/RTGS (Inter-Bank Transfer), Treasurer, Indian Geophysical Union, State Bank of India, Habsiguda Branch, Habsiguda, Uppal Road, Hyderabad- 500 007
A/C: 52191021424, IFSC Code: SBIN0020087, MICR Code: 500002318, SWIFT Code: SBININBBHO9.
For correspondence, please contact, Hon. Secretary, Indian Geophysical Union, NGRI Campus, Uppal Road,
Hyderabad - 500 007, India; Email: igu123@gmail.com; Ph: 040 27012332

ISSN: 0257-7968 (Clarivate Analytics)
ISSN: 0971-9709 (NISCAIR)
Approved as bimonthly ESCI journal by Clarivate Analytics
Cited in Indian Citation Index (ICI), New Delhi
Evaluated by NISCAIR, New Delhi

CONTENTS

Research Articles

Invited Article

J. Ind. Geophys. Union, 26(1) (2022), 1-7

Seismic Attribute Analysis of 3D seismic data: A case study from Taranaki basin, New Zealand

Pradeep Mahadasu* and Kumar Hemant Singh
Department of Earth Sciences, Indian Institute of Technology Bombay-400076.
*Corresponding author: pradeepgeophysics@gmail.com

ABSTRACT

Seismic attributes are the elements of seismic data that are extracted from the seismic reflection data to create seismic characteristics that emphasize certain physical, geological, or reservoir property aspects. Seismic characteristics derived from reflection data are based on a variety of physical processes. Wave properties, including amplitude, frequency, phase, and velocity, vary significantly when seismic waves propagate through earth's strata. Because of their restricted horizontal and vertical distribution, traditional seismic interpretation cannot always anticipate the geometry and spatial distribution of structural and stratigraphical features. The quantitative interpretation through seismic attributes enables a unique use of seismic characteristics to understand better fault systems, paleochannels, and spatial reservoir distribution. Seismic attributes, such as coherence, local structural dip, curvature, sweetness, RMS attribute, and envelope, are effective tools to understand the detailed geometry and variation in structural and stratigraphical features. Comparative seismic attribute analysis is undertaken to understand better the geometries of structural and stratigraphic features using 3D marine seismic data from Parihaka (Taranaki basin, New Zealand). The results can significantly improve the structural and stratigraphical interpretation and exploration objectives.

Keywords: Seismic attributes, Paleochannels, Faults, Coherence, Curvature, Sweetness, Quantitative interpretation.

INTRODUCTION

Hydrocarbon exploration aims to find and map structural and stratigraphic characteristics related to hydrocarbon production, deposition, movement, and entrapment (Omoja and Obiekezie, 2019). These structural and stratigraphic traps might be quite subtle, making accurate mapping challenging. However, advances in the 3D seismic reflection technique have made it feasible to map such structural and stratigraphic configurations with great precision and dependability, lowering the risk factor associated with hydrocarbon exploration. Seismic characteristics have been increasingly being employed in hydrocarbon exploration and reservoir characterisation studies for many years, and seismic interpretation procedures frequently include them (Marfurt and Kirlin, 2001). Geoscientists study and analyse the subsurface features like buried paleochannels, faults, and reservoir zones revealed by subsurface geophysical data using three-dimensional seismic datasets (Hossain, 2020).The study of seismic attributes is an essential element of seismic interpretation, and they have been used to identify the spatial distribution of reservoir's, structural and stratigraphical features (Fomel, 2007). In this study, different seismic attributes are extracted and analysed to understand the spatial distribution of structural, stratigraphical and hydrocarbon potential zones.

DATA

3D marine seismic data set is used for this study. New Zealand Crown Minerals provided the data set from Parihaka, Taranaki Bain, New Zealand. Kirchhoff time migrated, full angle, prestack is used for this study. Figure 1 shows the Parihaka 3D grid, about 324.79 sq km in area, is centered approximately 28 km to the northwest of New Plymouth, in the Taranaki Basin. It is a large sedimentary basin in the North Island, New Zealand. The Taranaki Basin covers an area of about 100,000 square kilometres, with the majority of the basin lying offshore at depths between 50 and 250 metres (Mattos et al., 2019). The Taranaki Basin is a central hydrocarbon-producing region in New Zealand that has a 150-year history of oil and gas exploration. The study area encompasses the southwestern end of the North Taranaki Graben, which is a prominent geological feature. The North Taranaki Graben is an under-explored, yet good location for oil and gas development, according to New Zealand Petroleum and Minerals (Shalaby et al., 2020).

SEISMIC ATTRIBUTE ANALYSIS

The seismic attribute is a quantity retrieved or produced from seismic data that may be studied to improve more subtle information in a typical seismic image, leading to improved geological or geophysical interpretation of the data (Li and Zhao, 2014a). Geometry, kinematics, dynamics, and statistical properties of seismic waves are extracted or generated from prestack and poststack seismic data via mathematical transformations (Li and Zhao, 2014a). Reservoir features and advanced 3D seismic interpretation are based on seismic attribute analysis, which allows us to extract information about lithology and reservoir heterogeneity from the seismic data (Li and Zhao, 2014b). Seismic characteristics are increasingly being employed in oil and gas exploration and production, and they have been incorporated into the seismic interpretation process. Seismic characteristics have evolved into several different forms, including structural and stratigraphic features (Chopra and Marfurt, 2005). Although amplitude data is the most basic form of seismic data, seismic attributes can disclose features that are not readily apparent in amplitude data (Hossain, 2020).

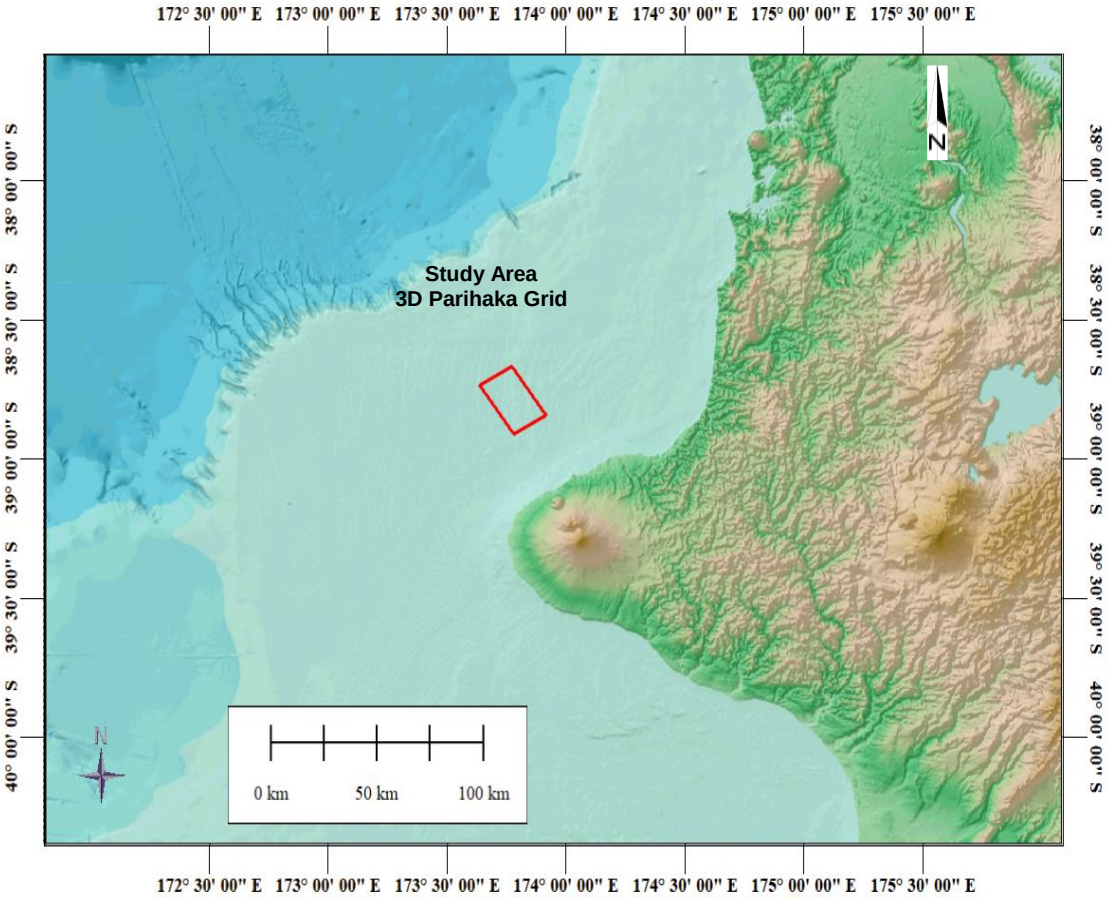

Figure 1. Shaded relief and general bathymetry of the western part of the North Island, New Zealand, indicating location map of the study area (red polygon) in the Taranaki Basin.

The seismic attribute approach should improve our capacity to understand a formation geologically, especially in thin-bed reservoir settings. A seismic waveform's amplitude, frequency, time, shape, and location are generally described as seismic characteristics (Novak Zelenika et al., 2018). Seismic attribute analysis has been used to identify prospects, determine depositional environments (e.g., paleo channels, carbonate build ups, buried reefs, subsurface mounds), discover and improve faults and fracture sets to unravel structural history, and even give direct hydrocarbon indications from seismic data (Burnett et al., 2003; Chopra and Marfurt, 2005; Hossain, 2020; Li and Zhao, 2014a). Seismic attribute analysis work flow to understand various structural and stratigraphical characteristics using 3D marine seismic data within the study area is detailed below (Figure 2).

Coherence attribute

One of the most often utilised attributes in seismic interpretation is coherence (Alaudah and AlRegib, 2017). Coherency or similarity is an edge approach that quantifies the degree of vertical and lateral discontinuity or coherence of reflections to assess deviations from a mean value (Pigott et al., 2013).Coherency refers to the similarity of adjacent traces (Chuai et al., 2014). This approach is used to map the lateral extent and emphasise faults, sedimentary structures (channels, fans, etc.) (Chopra and Marfurt, 2018).A coherency cube of the Parihaka 3D volume is generated from the 3D seismic data.

Local structural dip attribute

Local structural dip is a property that computes the best-fit plane (3D) or line (2D) between each trace's immediate neighbour traces on a horizon and outputs the amount of dip (gradient) of plane or line in degrees for each trace (Seismic Attribute Analysis, 2014). On a horizon slice, this may be used to make a pseudo paleogeologic map. Structural dip, also known as dip deviation, is an edge detection method for identifying rapid changes in local dips, such as fractures and channel edges. The structural dip characteristic effectively recognizes features like fault edges and flaws from reflected dip (Pigott et al., 2013).

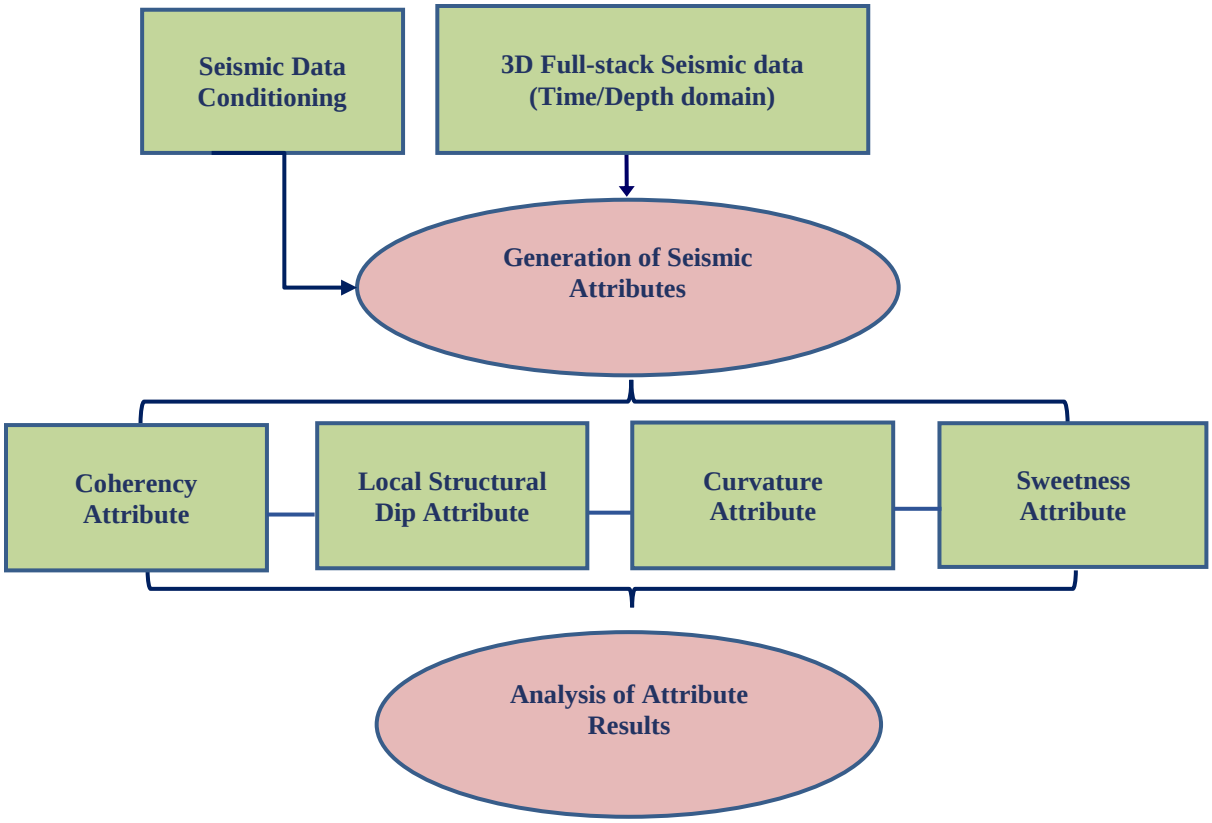

Figure 2. Work flow used for sesmic attribute analysis using 3D seismic data

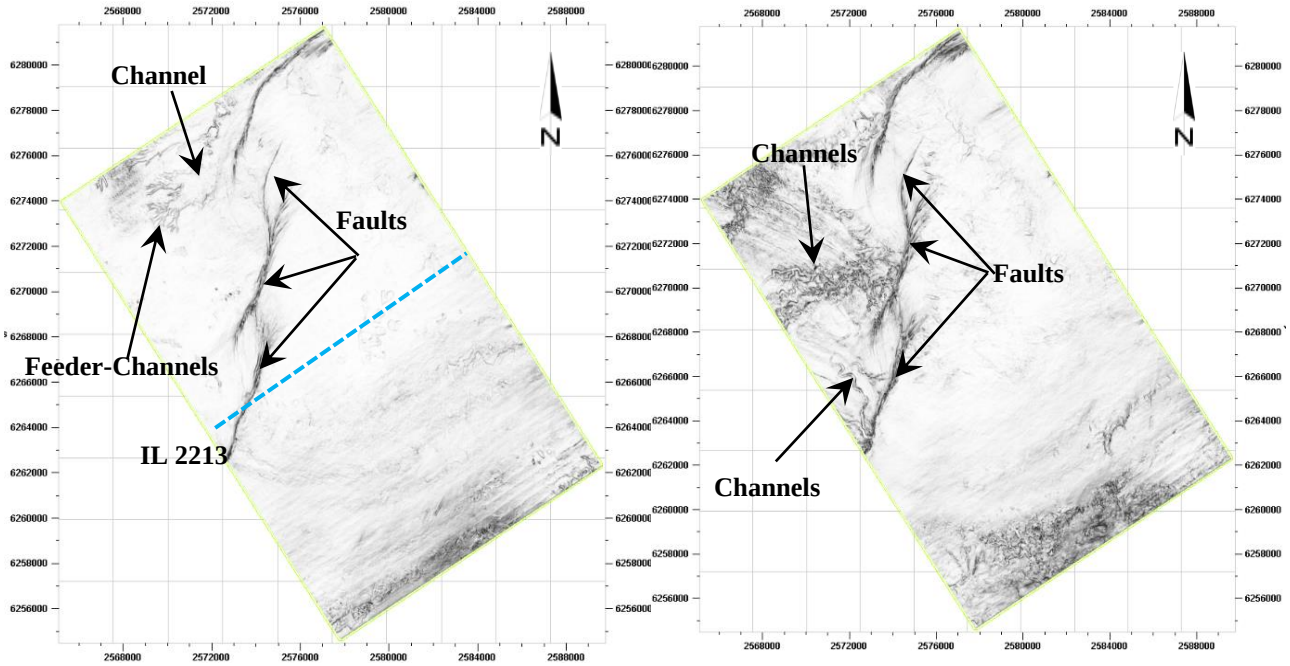

Figure 3a. Coherency attribute maps showing faults and paleo channels within the study area; Time slices 0.96 sec (left) and 1.09 sec (right).

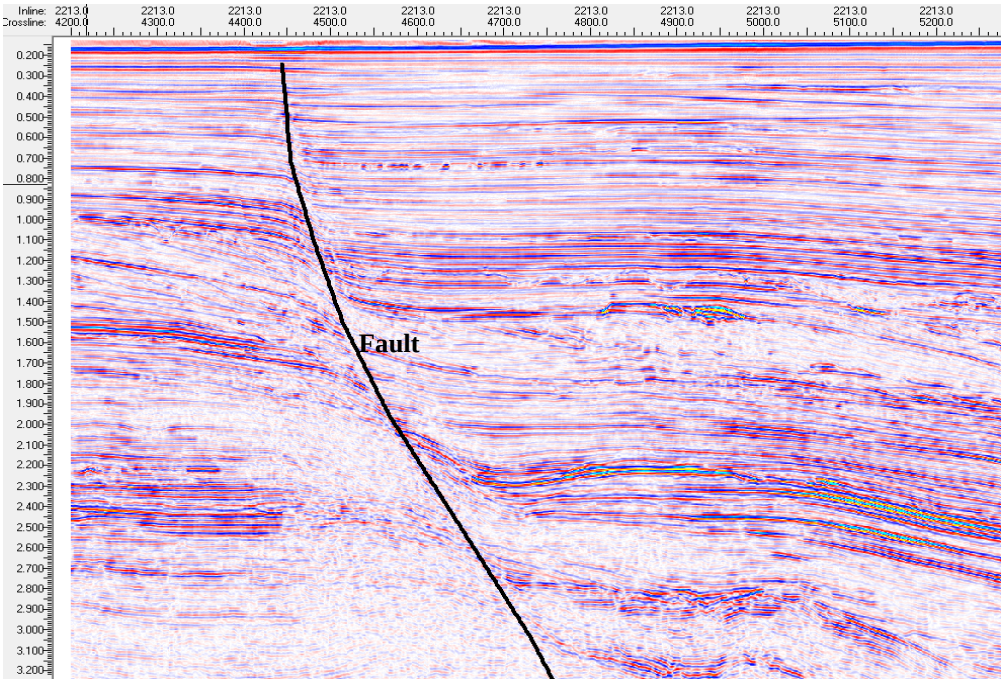

Figure 3b. Seismic cross-section for Inline 2213 showing the interpreted fault on coherency volume

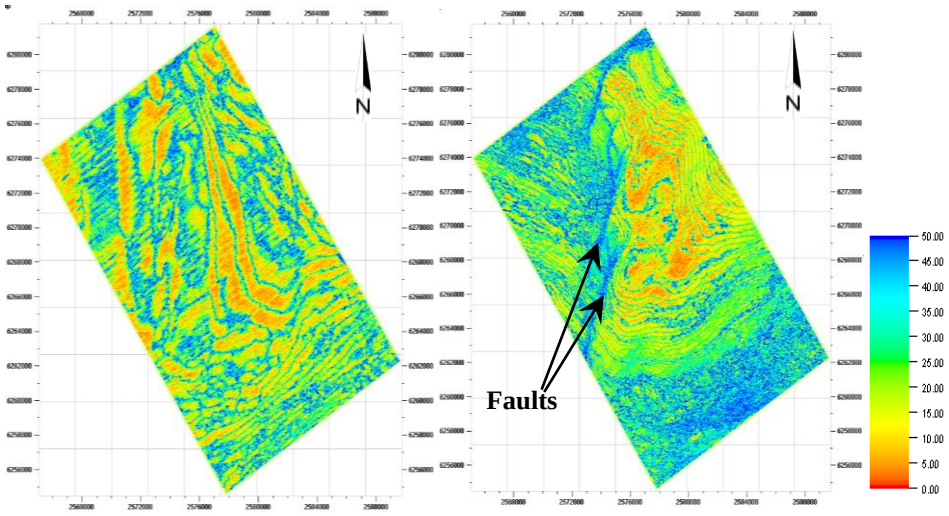

Figure 4. Structural dip attribute maps show dip severity across time slices at 0.4 sec (left) and 1.2 sec (right). The color bar shows dip variations.

Curvature attribute

Curvature attribute maps are helpful for interpreting and visualising structural characteristics (Sigismondi and Soldo, 2003). Faults and lineaments can be identified using curvature attributes (Roberts, 2001). The curvature of a particular horizon is used to compute a set of post-stack characteristics. The magnitude or direction of maximum curvature, the magnitude of curvature along the horizon's azimuth (dip) direction, the magnitude of curvature along the horizon's strike direction, and the magnitude of curvature of a contour line along a horizon are some of these attributes (Chopra and Marfurt, 2007). Curvature is a helpful attribute in 3D seismic interpretation that describes the geometry of seismic reflectors and has been frequently utilised to locate faults in the subsurface (Gao, 2013)

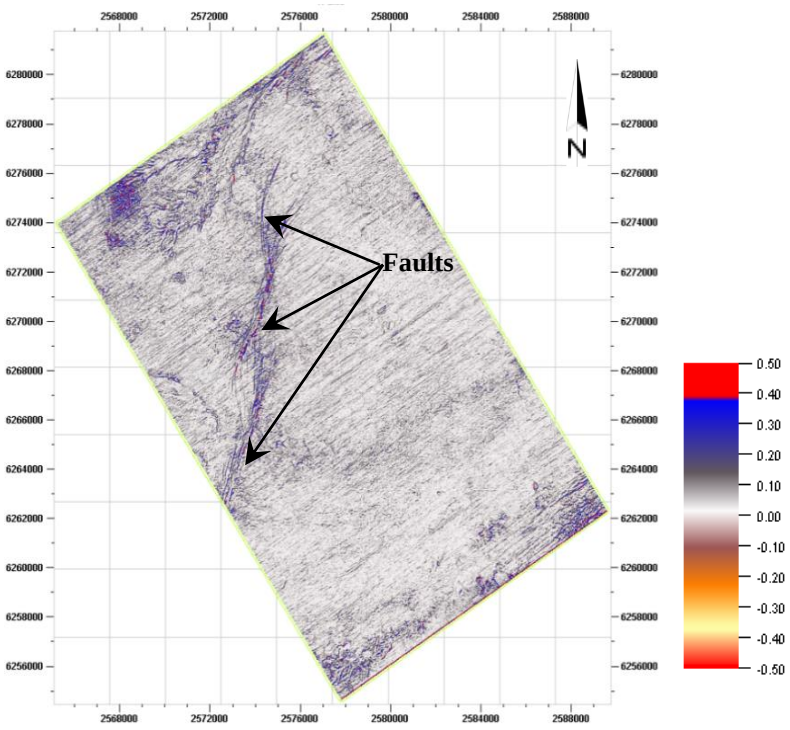

.**Figure 5.** Curvature attribute map showing the structural features ontime slice 0.96 sec. The color bar shows curvature radient (1/m) variations

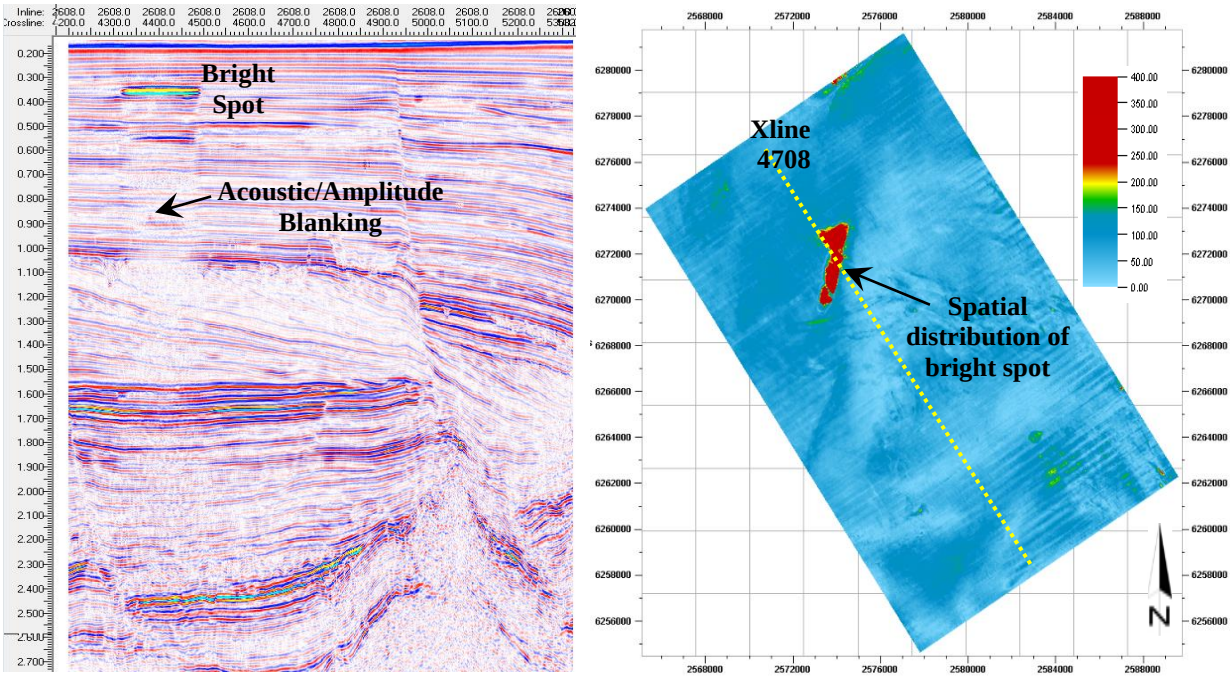

Figure 6. Sweetness attribute map showing the shallow gas anomalies on time slice 285ms (right) and seismic cross-section for Xline 4708 (left)

Sweetness attribute

As the amplitude envelope divided by the instantaneous frequency, the seismic sweetness attribute is commonly used as a sand/shale indication. The sweetness attribute is also used to understand the spatial distribution of bright spots associated with possible hydrocarbon origins (Chopra and Marfurt, 2005). When contrasted to seafloor reflections, the bright spots appear as increased amplitude reflections with reverse polarity. Seismic anomalies with bright amplitudes possibly occur when hydrocarbons are present (Cox et al., 2020). These anomalies are typically seen above acoustic blanking zones/gas chimneys and appear to be linked to subsurface fractures/faults, suggesting that the source of hydrocarbon build up in the area may be linked to deeper structures (Kluesner and Brothers, 2016; Liu et al., 2020). Gas-charged sediments and possible gas or fluid movement routes within the studied region can thus be linked to the existence of high amplitude and low-frequency anomalies (Andreassen et al., 2007; Kim et al., 2020). Gas-related seismic anomalies are predicted to have "bright" and anomalously high negative amplitudes due to a drop in the bulk modulus (due to the exceptionally low density of gas) and a substantially negative polarity along the boundary at the top of the gas-bearing reservoir (Cox et al., 2020; Nanda, 2016). Regions associates with high sweetness values are most likely to indicate possible hydrocarbon origins (Radovich and Oliveros, 1998).

Figure 6. Sweetness attribute map showing the shallow gas anomalies on time slice 285ms (right) and seismic cross-section for Xline 4708 (left).

RESULTS AND DISCUSSIONS

Four seismic attributes such as coherence, local structural dip, curvature, and sweetness attribute volumes are generated from 3D seismic data using Emerson-paradigm and OpendTect software to identify structural and stratigraphical features within the study area. The coherency attribute data shows sharp imaging of NE-SW oriented Fault zones, buried paleochannels, and meandering channelling systems. At the channel-head of several of the channels, there are some feeder channels observed. Figure 3a shows seismic coherency attributes time slices and some of the faults and paleochannels, which are observed within the study area. Figure 3b shows the seismic cross-section with fault interpretation along coherency attribute volume for inline 2213. Low to moderate seismic amplitudes, chaotic, discontinuous, dipping, and parallel seismic events characterise paleochannels in seismic cross-sections. Many deeper and shallow faults are observed within the study area. Structural dip attribute maps are extracted to identify subsurface dip variations within the study area. These maps showing the dip severity across time slices at 0.4 and 1.2 secs in Figure 4. Because of their enormous reflector displacement, significant faults are easily detectable in dip attribute maps. Dips are increased in the NE-SW trend and clearly showing the failure of slope sediments across the faults. Curvature attribute maps are also extracted in terms of seismic gradient (1/m). The resulted attribute maps the fault patterns very clearly on time slices (Figure 5). Similarly, seismic sweetness attribute maps are extracted from 3D seismic data used to investigate the physical features of anomalies, typically isolated bright spots or brightening over single horizons, as well as their spatial and stratigraphic distribution. Seismic recordings in the research region show some acoustic blanking or potential gas chimneys, as well as high amplitude anomalies. As such, within the study area, 3D seismic data revealed several zones of acoustic blanking/gas chimneys and high amplitude anomalies. On the seismic section, these zones appear as severely dimmed or acoustically transparent reflection zones. They often appear beneath increased reflections and end at various stratigraphic levels. Thin vertical columnar disruptions can also be seen (Figure 6). Acoustic blanking, characterised by strong, persistent top reflection and a wipe out below, is prominent in some regions (Figure 6). The amplitudes of the reflections are dimmed in deeper regions, and there is weak horizontal continuity (Figure 6).These acoustic blanking zones are found to correspond to the existence of possible shallow gas or fluid movement from deeper horizons. The amplitude or frequency loss is due to the absorption of seismic propagated energy within the gas-charged sediment layers. The high-frequency component of the seismic wave is attenuated because gas is a poor conductor of seismic energy. High-amplitude reflections, which are termed enhanced reflections, are observed with reverse polarity in the shallow sediments. These reflections appear to extend laterally and have sharp cut-off edges. The reflections are usually located directly above acoustic blanking zones or gas chimneys and are seemingly associated with near-surface fractures or faults, suggesting that the origin of gas accumulation in the area could be related to deeper structures. Some of igneous bodies also exhibits as high amplitude anomalies with normal polarity. Sweetness attribute maps illustrate the geographical distribution of shallow high amplitude anomalies (Figure 6).

CONCLUSIONS

Seismic attribute analysis was carried out using 3D marine seismic data to spatially extract structural and stratigraphical features in the Parihaka study area of the Taranaki basin, New Zealand. Features such as faults, complex of paleochannels, and bright spots associated with shallow hydrocarbon anomalies were identified using 3D seismic

attributes. The detailed results of 3D seismic attribute analysis are helpful in the geological interpretation and prospect evaluation. The present study has detailed the application of various seismic attributes to understand the spatial distribution of structural and stratigraphical features.

ACKNOWLEDGMENT

The authors of this article express their thanks to Emerson-Paradigm and OpendTect for providing software access and ongoing assistance, which enabled them to conduct this research.

Compliance with Ethical Standards

The authors declare that they have no conflict of interest and adhere to copyright norms.

REFERENCES

Alaudah, Y. and AlRegib, G., 2017. A directional coherence attribute for seismic interpretation, in: SEG Technical Program Expanded Abstracts 2017. Society of Exploration Geophysicists, 2102–2106. https://doi.org/10.1190/segam2017-17739097.1

Andreassen, K., Nilssen, E.G. and Ødegaard, C.M., 2007. Analysis of shallow gas and fluid migration within the Plio-Pleistocene sedimentary succession of the SW Barents Sea continental margin using 3D seismic data. Geo-Marine Lett., 27, 155–171.

Burnett, M.D., Castagna, J.P., Méndez-Hernández, E., Rodríguez, G.Z., García, L.F., Vázquez, J.T.M., Avilés, M.T. and Villaseñor, R.V., 2003. Application of spectral decomposition to gas basins in Mexico. Lead. Edge, 22, 1130–1134.

Chopra, S., and Marfurt, K.J., 2005. Seismic attributes — A historical perspective. Geophysics, 70, 3SO-28SO.

Chopra, S., and Marfurt, K., 2007. Curvature attribute applications to 3D surface seismic data. Lead. Edge, 26, 404–414.

Chopra, S. and Marfurt, K.J., 2018. Coherence attribute applications on seismic data in various guises — Part 1. Interpretation, 6, T521–T529.

Chuai, X., Wang, S., Yuan, S., Chen, W. and Meng, X., 2014. A seismic texture coherence algorithm and its application. Pet. Sci., 11, 247–257.

Cox, D.R., Knutz, P.C., Campbell, D.C., Hopper, J.R., Newton, A.M.W., Huuse, M. and Gohl, K., 2020. Geohazard detection using 3D seismic data to enhance offshore scientific drilling site selection. Sci. Drill., 28, 1–27.

Fomel, S., 2007. Local seismic attributes. Geophysics, 72, A29–A33.

Gao, D., 2013. Integrating 3D seismic curvature and curvature gradient attributes for fracture characterization: Methodologies and interpretational implications. Geophysics, 78, O21–O31.

Hossain, S., 2020. Application of seismic attribute analysis in fluvial seismic geomorphology. J. Pet. Explor. Prod. Technol., 10, 1009–1019.

Kim, Y.J., Cheong, S., Chun, J.H., Cukur, D., Kim, S.P., Kim, J.K. and Kim, B.Y., 2020. Identification of shallow gas by seismic data and AVO processing: Example from the southwestern continental shelf of the Ulleung Basin, East Sea, Korea. Mar. Pet. Geol., 117, 104346.

Kluesner, J.W.and Brothers, D.S., 2016. Seismic attribute detection of faults and fluid pathways within an active strike-slip shear zone: New insights from high-resolution 3D P-Cable^{TM} seismic data along the Hosgri Fault, offshore California. Interpretation, 4, SB131–SB148.

Li, M. and Zhao, Y., 2014a. Seismic Attribute Analysis, in: Geophysical Exploration Technology. Elsevier, pp. 103–131.

Li, M. and Zhao, Y., 2014b. Prestack Seismic Inversion and Seismic Attribute Analysis, in: Geophysical Exploration Technology. Elsevier, 199–219.

Liu, B., Chen, J., Waseem Haider, S., Deng, X., Yang, L. and Duan, M., 2020. New high-resolution 2D seismic imaging of fluid escape structures in the Makran subduction zone. China Geol., 3, 1–14.

Marfurt, K.J. and Kirlin, R.L., 2001. Narrow- band spectral analysis and thin- bed tuning. Geophysics, 66, 1274–1283.

Mattos, N.H., Alves, T.M., Scully, A., 2019. Structural and depositional controls on Plio-Pleistocene submarine channel geometry (Taranaki Basin, New Zealand). Basin Res. 31, 136–154.

Nanda, N.C., 2016. Direct Hydrocarbon Indicators (DHI), in: Seismic Data Interpretation and Evaluation for Hydrocarbon Exploration and Production. Springer International Publishing, Cham, 103–113.

Novak Zelenika, K., Novak Mavar, K. and Brnada, S., 2018. Comparison of the Sweetness Seismic Attribute and Porosity–Thickness Maps, Sava Depression, Croatia. Geosciences, 8, 426.

Omoja, U.C. and Obiekezie, T.N., 2019. Application of 3D Seismic Attribute Analyses for Hydrocarbon Prospectivity in Uzot-Field, Onshore Niger Delta Basin, Nigeria. Int. J. Geophys., 2019, 1–11.

Pigott, J.D., Kang, M.-H. and Han, H.-C., 2013. First order seismic attributes for clastic seismic facies interpretation: Examples from the East China Sea. J. Asian Earth Sci., 66, 34–54.

Radovich, B.J. and Oliveros, R.B., 1998. 3-D sequence interpretation of seismic instantaneous attributes from the Gorgon Field. Lead. Edge, 17, 1286–1293.

Roberts, A., 2001. Curvature attributes and their application to 3D interpreted horizons. First Break, 19, 85–100.

Seismic Attribute Analysis, 2014. , in: Harness Oil and Gas Big Data with Analytics. Wiley, 63–106.

Shalaby, M.R., Binti Sapri, S.H., and Islam, M.A., 2020. Integrated reservoir characterization and fluid flow distribution of the Kaimiro Formation, Taranaki Basin, New Zealand. J. Pet. Explor. Prod. Technol. 10, 3263–3279.

Sigismondi, M.E.and Soldo, J.C., 2003. Curvature attributes and seismic interpretation: Case studies from Argentina basins. Lead. Edge, 22, 1122–1126.

Received on: 01.12.2021; Revised on: 10.12.2021; Accepted on: 04.01.2022

J. Ind. Geophys. Union, 26(1) (2022), 8-22

Comparison of improved particle swarm optimization with Marquardt Algorithm for simulation of sedimentary basin with parabolic density contrast using gravity data

Soudeh Loni and Mahmoud Mehramuz*
Department of Earth Sciences, Science and Research Branch, Islamic Azad University, Tehran, Iran
* Corresponding author: m.mehramooz@srbiau.ac.ir

ABSTRACT

In this paper, Improved Particle Swarm Optimization (IPSO) and Marquardt algorithms are used to estimate the depth of the sedimentary basin, leading to the determination of the basement and simulation of sedimentary basin. In these methods, the sedimentary basin is simulated by using the density contrast that changes parabolically with depth and several prisms aligned with the same width and different lengths. The proficiency of the mentioned algorithms has been investigated by considering a hypothetical sedimentary basin. Depth estimation of the sedimentary basin using the calculated gravity field is performed by both mentioned methods and their results compared. By comparing the observed model parameters range with the calculated value of the model parameters and also by analyzing the misfit between the observed and calculated gravity, we concluded that the IPSO algorithm is a reliable method for estimating the sedimentary basin depth and simulating it. The IPSO algorithm has also been applied for the gravity inverse modeling of a sedimentary basin in the Northeast region of Iran.

Keywords: Marquardt algorithm, IPSO, sedimentary basin, gravity anomaly, 2.5-D rectangular prism

INTRODUCTION

Gravity inversion is a conventional tool that is used for evaluating the structure of sedimentary basins in applied geophysics. The primary aim of the inversion of gravity is to determine the parameters of the subsurface anomalies, for example, amplitude coefficient, location of origin, depth, and parameter of shape. Nowadays, because of the progression of software engineering and artificial intelligence, the developmental algorithm based on collective intelligence is intended to upgrade building forms superior to conventional methods (Kennedy and Eberhart, 1995). Gravity inversion of sedimentary basin basement can be suggested as a 2-D or 3-D issue, depending on the design of the model. The 2-D model is extremely popular and includes the reversal of at least one different profiles along the basin to reach its most extreme depth. While the basin is extended, a typical methodology for the semi 3-D model involves the reversal of several orthogonal profiles with the longest lengths. The 2-D technique considers the anomalous body with an infinite extension that is perpendicular to a gravimetric profile. The literature has suggested different nonlinear modeling approaches for simulating the sedimentary basin:

The construction of sedimentary basin has been simulated using juxtaposed rectangular prisms with specific density (Chakravarthi, 1995; Barbosa et al., 1997; Silva et al., 2006), polygons with arbitrary vertices (Chakravarthi et al., 2001), polynomial functions (Martín Atienza, 2001), or a trapezoid (Rao, 1990). To resolve this ambiguousness in gravity anomaly, the source of an anomaly with a particular density contrast can be assumed to have an appropriate geometric shape (Rao and Murthy, 1978). In order to depict the sedimentary basin with 2-D cross-segment, Bott (1960) utilized the cubic model and Tolwani et al. (1959) utilized the polygon model. Chakravarthi and Sundarajan (2005, 2007) modeled a 2.5-D sedimentary basin using the Marquardt algorithm and variable density contrast with depth. Additionally, the sedimentary basin was simulated using the cubic density function (García-Abdeslem, 2005), quadratic density function (Gallardo-Delgado et al., 2003), and exponential density function (Cordel, 1973). Karcol (2018) generalized the solution for the gravitational potential and its derivatives of the right rectangular prism with depth-dependent density that can be approximated by an *n*-th degree polynomial.

The PSO algorithm utilizes the principle of community optimization to solve issues in different contexts and can be used to improve issues that are relatively irregular and change over time. The PSO is used in different fields. Based on the neuro-fuzzy network, an immune PSO for image backlight amends with a functional link was suggested by Lin and Liu (2009). In order to accomplish the threshold of optimality for multi-level image distribution, Zahara et al. (2005) utilized the PSO. Zhang et al. (2010a) suggested a versatile turbulent PSO to the categorization of the magnetic resonance brain image. Samanta and Nataraj (2009) incorporated Artificial Neural Networks (ANN) into PSO and Support Vector Machine (SVM) for fault detection, and results of the PSO were better than genetic algorithm results. A neural network for remote-sensing image categorization was suggested by Zhang et al. (2010b) using the PSO.

The PSO algorithm is a new method that has been effectively utilized in some of the fields of geophysics, such as inversion of self-potential of idealized bodies' anomalies (Monteiro Santos, 2010), gravity assessment of a fault, and estimation of its parameters such as angle of the fault, thickness of the sheet, and left and right distances to

the middle of the sheet using PSO (Toushmalani, 2013a,b), the application of the members of PSO family to the 2-D and 3-D gravity inversion and uncertainty assessment of basement relief in sedimentary basins (Pallero et al., 2015 and 2017), focus on the use of a PSO algorithm to sample the region of equivalence in nonlinear inverse problems (Pallero et al., 2018), usage of PSO to gravity inversion of 2.5-D sedimentary basins (Singh and Singh, 2017), inversion of residual gravity anomalies utilizing tuned PSO (Roshan and Singh, 2017) and interpretation of gravity data using PSO (Essa and El-hussein, 2018). In this paper, the depth of the sedimentary basin is estimated by IPSO and Marquardt algorithms using gravity data and their results are compared.

METHOD

Gravity Anomaly of a Sedimentary Basin

Figure 1 illustrates the geometrical form of the 2.5-D rectangular prism. Several juxtaposed 2.5-D rectangular prisms can be used to simulate the sedimentary basin. A gravity anomaly can be obtained at each point of observation, $P(x_k,0)$, that cover the sedimentary basin (Chakravarthi and Sundarajan, 2006) as:

$$g_b = \sum_{i=2}^{NI} g_i(x_k,0) + Ax_k + B \qquad (1)$$

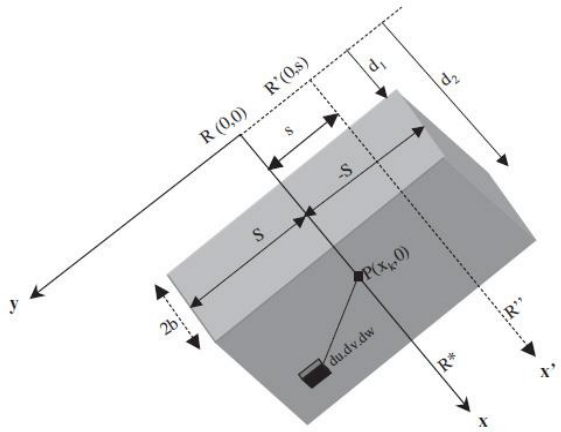

Figure 1. A 2.5-D rectangular prism that its strike length, width and offset distance of profile, RR', is 2*S*, 2*b*, *s*

Where *N*, *A*, and *B* are the number of gravity observation points, the regional gravity gradient and a constant on the profile, RR*, and $g_i(x_k, 0)$ is the gravity anomaly of the i_{th} prism at any point that was introduced by Chakravarthi and Sundararajan (2005) as:

$$g(x_k,0) = \int_{w=d_1}^{d_2}\int_{v=-S}^{S}\int_{u=-b}^{b} \frac{G\Delta\rho(w)\,du\,dv\,dw}{\left[(u-x_k)^2+v^2+w^2\right]^{3/2}} \qquad (2)$$

Where *G* is the universal gravitational constant and *dudvdw* is a volume element of prism. 2*S*, 2*b* are the strike length and width of the prismd_1 and d_2 are upper and lower depth of the prism, respectively. $\Delta\rho(w)$is the parabolic density contrast that was developed by Chakravarthi et al. (2001) as:

$$\Delta\rho(w) = \frac{\Delta\rho_0^{\,3}}{(\Delta\rho_0 - \alpha w)^2} \qquad (3)$$

$\Delta\rho_0$ is the density contrast evaluated at the ground surface and α is the rate of variation of density contrast expressed in length units.$\Delta\rho_0$ and α can be determined by fitting the field data of density contrast vs. depth in the least square sense to Eq. (3) (Rao et al., 1995). Substituting Eq. (3) in Eq. (2), the calculated gravity is obtained as:

$$\begin{aligned} g(x_k,0) = -2G\,\Delta\rho_0^{\,3}\Bigg\{ & \frac{\alpha x_k S}{t_4}\left(\frac{1}{t_4}+\frac{1}{t_3}\right) ln\frac{t_5}{t_6} + \frac{S}{2t_2} \\ & \times ln\frac{(R+x_k)}{(R-x_k)} + \frac{x_k}{2t_3} ln\frac{(R+S)}{(R-S)} \\ & + \frac{\Delta\rho_0}{\alpha}\Bigg[\frac{1}{t_2}tan^{-1}\frac{SR}{wx_k} + \frac{1}{t_3}tan^{-1}\frac{x_kR}{wS}\Bigg] \\ & - \frac{1}{\alpha t_5}tan^{-1}\frac{Sx_k}{wR}\Bigg|_{x_k-b}^{x_k+b}\Bigg|_{d_1}^{d_2}\Bigg\} \end{aligned} \qquad (4)$$

Here

$R=x_k^2+S^2+w^2$

$t_1=x_k^2+S^2$

$t_2=S^2\alpha^2+\Delta\rho_0^{\,2}$

$t_3=x_k^2\alpha^2+\Delta\rho_0^{\,2}$

$t_4=\sqrt{t_1\alpha^2+\Delta\rho_0{}^2}$

$t_5=\Delta\rho_0{}^2-\alpha w$

$t_6=-2(\alpha R t_4+t_1\alpha^2+\Delta\rho_0\alpha w)$

Theory of the Marquardt Optimization Method

Using the gravity anomaly at any point of observation, x_k, the Marquardt method starts and the initial depth of each observation point on the sedimentary basin is calculated (Chakravarthi et al., 2001) as:

$$z_i=\frac{g_{obs}(x_i)\Delta\rho_0}{41.89\Delta\rho_0{}^2+\alpha g_{obs}(x_i)} \quad , \quad i=2,3,\ldots,N-1 \quad , \quad z_1=z_N=0 \qquad (5)$$

The calculated gravity anomaly and initial depths are determined by using Using Eq. (1) and Eq. (5), respectively. A misfit function can clarify the difference between the observed and the calculated gravity anomalies (Chakravarthi and Sundarajan, 2006):

$$J=\sum_{k=1}^{N}[g_{obs}(k)-g_{cal}(k)]^2 \qquad (6)$$

Where N is the number of unknown parameters (N-2 depths and 2 coefficients of the regional anomaly (A, B)). The difference between observed and calculated gravity anomalies is utilized to upgrade the N-2 calculated depth of the basin and 2 regional background coefficients by solving the standard equation method using the Marquardt (1963) algorithm as:

$$\sum_{k=1}^{N}[g_{obs}(k)-g_{cal}(k)]\frac{\partial g_{cal}}{\partial P_{j'}}=\sum_{k=1}^{N}\sum_{k=1}^{N}\frac{\partial g_{cal}}{\partial P_{j'}}\frac{\partial g_{cal}}{\partial P_k}\times(1+\delta_{j'k}\lambda)dP_k,\ j'=1,2,..,N \qquad (7)$$

$$P_{K-1}=z_k,\ k=1,2,\ldots,N-1$$

$$P_{N-1}=A,\ P_N=B$$

Where λ is the damping factor.

Chakravarthi and Sundarajan (2006) appraised the utilization of the Marquardt algorithm (Marquardt, 1963). To stop the algorithm automatically, must one of the following terms happens: the current misfit function is less than expected error or when the number of iteration is over or the damping factor is considered an unconventionally large value.

PSO Algorithm

The PSO method simulates the social behavior of particles; it optimizes their situation based on artificial intelligence. During the assessment procedure, the situation of every particle may vary with every iteration. In the other words, during the trend of iteration, the particle position is renovated so that the particle finds the best of its position, *pbest*, and the best of its position among the collection of particles, *gbest*. Consequently, to find the best position, each particle tries to change its current velocity to optimize its position. The velocity of particle is modified to reach a new position utilizing the following equations provided by Sweilam et al. (2007) as:

$$V_i^{t+1}=wV_i^t+c_1 rand(\ )(pbest_i-X_i^t)+c_2 rand(\ )(gbest_i-X_i^t) \qquad (8)$$

$$X_i^{t+1}=X_i^t+V_i^{t+1} \qquad (9)$$

V_i^t, X_i^t are current velocity and position of i_{th} particle at the t_{th} iteration, *r and* () function generates random numbers between 0-1, c_1,c_2 are learning factors with constant and positive values that control both the personal and the social behavior and w is an inertial coefficient with a magnitude generally marginally below 1 (Monteiro Santos, 2010).

Easiness and simplicity of execution are the advantages of the PSO algorithm but falling into the local minimum and premature convergence are its disadvantages (Yi, 2016). In this paper, we suggest an Improved Particle Swarm Optimization (IPSO) algorithm that adjusts inertia weight (w) and learning factors (c_1,c_2) to solve this problem.

IPSO Algorithm: Improvement of Inertia Weight (w) and Learning Factors (c_1,c_2)

In order to avoid premature convergence to local optimality and increase convergence speed, the IPSO algorithm is being used. For this purpose, the inertia weight (w) coefficient and learning factors (c_1,c_2) are improved. The various inertia weighting strategies are categorized into three classes: constant and random inertia weight, time-varying inertia weight, and adaptive inertia weight (Nikabadi et al., 2011). In this paper, we use time-varying inertia in order to determine the value of w based on the iteration number. This method can be linear or non-linear and decreasing or increasing. Here, the linearly decreasing

technique is used to modify the inertia weight of particle in the following equation (Xin et al., 2009):

$$w=\frac{T_{max}-t_{it}}{T_{max}}\times(w_{max}-w_{min})+w_{max} \quad (10)$$

Where t_{it} and T_{max} are the number of current and maximum iteration. The value of w decreases from w_{max} to w_{min}. Based on the results obtained (Shi and Eberhart, 1998) the performance of linearly decreasing strategy can be improved significantly when w_{max}=0.9 and w_{min}=0.4.

The learning factors (c_1,c_2) are traditionally both equal to 2 (Sweilam et al., 2007). However, utilizing recent literature, electing c_1 more predominant than c_2 and $c_1+c_2\leq 4$ may lead to the present better conclusions (Parsopoulos and Vrahatis, 2002). In order to improve the proficiency of PSO, the values of two operators c_1 and c_2 are updated by two dynamic linear equation, respectively, at each iteration (Yi, 2016) as follows:

$$c_1=2.4-\frac{1.4t_{it}}{T_{max}} \quad (11)$$

$$c_2=0.9+\frac{1.6t_{it}}{T_{max}} \quad (12)$$

With this strategy, c_1 can be decreased and $c_2$can be increasedby increasing the number of iterations. The global investigation capability of particles can be improved by this approach in the whole search space.

When the differences between the observed and calculated gravity data is minimized, the best exact values of the particles (model parameters) are obtained. For this purpose, we use the following simple objective function (Monteiro Santos, 2010):

$$Q=\frac{2\Sigma_i^N|g_i^o-g_i^c|}{\Sigma_i^N|g_i^o-g_i^c|+\Sigma_i^N|g_i^o+g_i^c|} \quad (13)$$

Where N is the number of the gravity measurement points, g_i^o,g_i^c are the observed and calculated gravity anomaly at the point $P(x_i)$, respectively.

The misfit between observed and calculated gravity data is estimated through the average relative error, which is computed by the following equation:

$$ms=\frac{100}{N}\sqrt{\Sigma_i^N\left(\frac{g_i^o-g_i^c}{g_i^o}\right)^2} \quad (14)$$

The optimization process repeats until the required number of iteration is completed or the current value of the objective function, Eq. (13), reaches below a predetermined allowable error.

Synthetic Model

Figure 2 displays a view from above of a theoretical sedimentary basin structure which has been approximated by a series of rectangular prisms positioned in adjacency and having the same widths as top of each prism. The values of $\Delta\rho_0$,α are assumed as -0.5 g/cm^3 and 0.025 g/cm^3/km, respectively. The characteristics of each prism have been brought in Table 1.

According to the defined search ranges for the depth and gravity parameters, as shown in Table 2, 100 primary models were randomly constructed. These ranges include the values assumed for the initial model. The number of iterations and predefined error are considered as 140 and 0.06, respectively. The code has performed 140 iterations before the objective function error between the calculated and synthetic gravity falls below the allowable error.

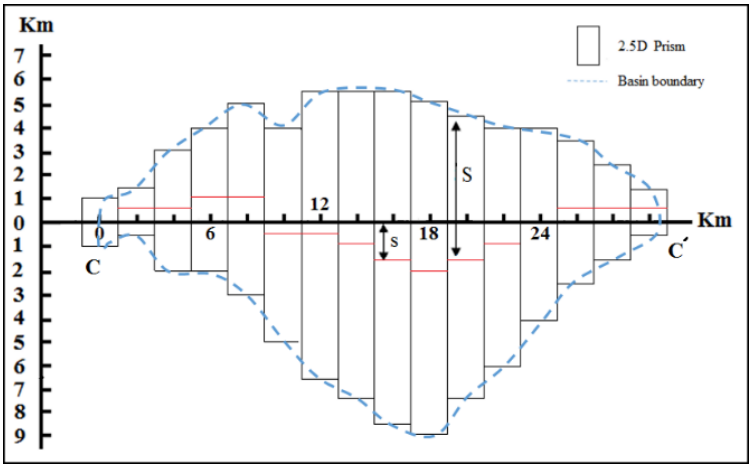

Figure 2. A sedimentary basin that has been made by series of rectangular prisms

Table 1. Specifications of each numbered prism shown in Figure 2

Prism	Depth(km)	*S* (km)	*s*(km)	Prism	Depth(km)	*S* (km)	*s*(km)
1	0	1	0	**9**	5	7	1.5
2	0.5	1	-0.5	**10**	4.5	7	2
3	1	2.5	-0.5	**11**	4	6	1.5
4	2	3	-1	**12**	3.5	5	1
5	2.5	4	-1	**13**	3	4	0
6	3	4.5	0.5	**14**	2	3	-0.5
7	4	6	0.5	**15**	1	2	-0.5
8	5	6.5	1	**16**	0	1	-0.5

Table 2. The values of assumed ranges for depths and inverted depths using IPSO, while the data are noise-free and corrupted with noise

Parameter		**Range**		**Initial depth (km)**	**Estimated depth (km) (noise-free)**	**Percent error**	**Estimated depth (km) (with 10% noise)**	**Percent error**	**Estimated depth (km) (with 15% noise)**	**Percent error**
Depth	**Gravity**	**Depth (km)**	**Gravity (mGal)**							
z_2	g_2	0 - 1	-8 , -15	0.5	0.51	2	0.41	18	0.41	18
z_3	g_3	0 - 2	-15 , -25	1	1	0	0.91	9	0.9	10
z_4	g_4	0.5 - 3.5	-25 , -35	2	2	0	1.89	5.5	1.9	5
z_5	g_5	1 - 4	-35 , -44	2.5	2.48	0.8	2.4	4	2.39	4.4
z_6	g_6	1 - 5	-41 , -50	3	2.97	1	2.88	4	2.88	4
z_7	g_7	2 - 6	-46 , -55	4	3.96	1	3.87	3.25	3.87	3.25
z_8	g_8	3 - 7	-50 , -60	5	4.94	1.2	4.85	3	4.86	2.8
z_9	g_9	3 - 7	-51 , -61	5	4.94	1.2	4.85	3	4.86	2.8
z_{10}	g_{10}	2.5 – 6.5	-50 , -60	4.5	4.45	1.1	4.63	3.1	4.36	3.1
z_{11}	g_{11}	2 - 6	-47 , -56	4	3.96	1	3.87	3.25	3.87	3.25
z_{12}	g_{12}	1.5 – 5	-44 , -54	3.5	3.47	0.86	3.37	3.7	3.37	3.71
z_{13}	g_{13}	1 - 5	-36 , -45	3	2.97	1	2.88	4	2.88	4
z_{14}	g_{14}	0.5 – 3.5	-28 , -38	2	2	0	1.89	5.5	1.89	5.5
z_{15}	g_{15}	0 - 2	-17 , -26	1	1	0	0.91	9	0.9	10

The generated gravity anomaly using IPSO inversion has been displayed in Figure 3a. Figure 3b depicts the assumed depths and estimated ones using IPSO for each prism. Figure 3c shows the error variation versus iteration number. The numerical outputs of the IPSO inversion are listed in Table 2. The estimated misfit by the Eq. (14) at the last iteration is 0.0674%.

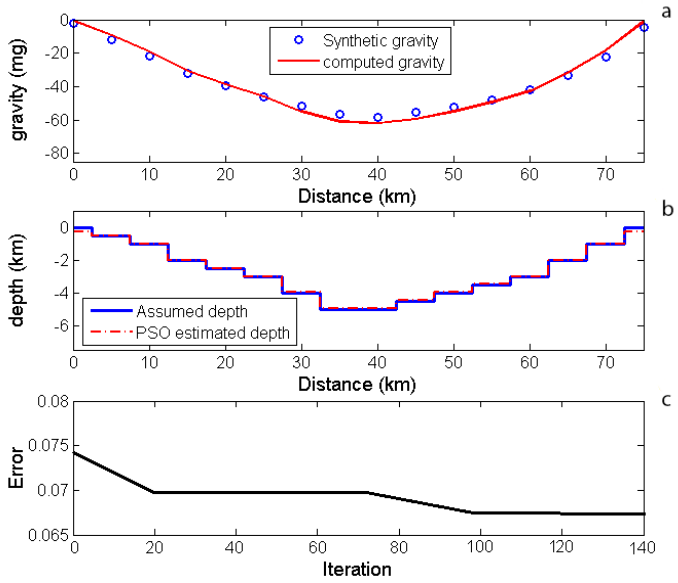

Figure 3. **(a)** Synthetic and computed gravity due to **(b)** assumed and interpreted basement model by IPSO. **(c)** Error changes estimated by objective function versus iteration number

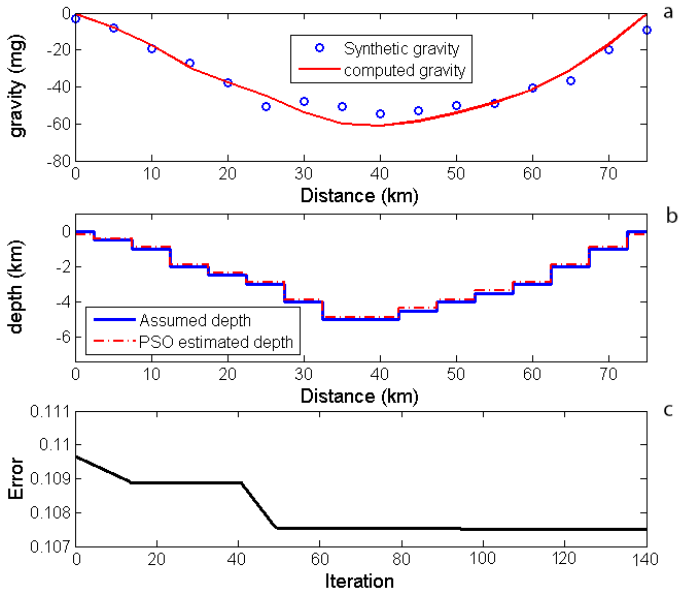

Figure 4. **(a**) Synthetic gravity data with 10% added noise and computed gravity due to **(b)** assumed and interpreted basement model by IPSO. **(c)** Error changes estimated by objective function versus iteration number

We assess the effect of error on the ability of the IPSO by adding 10% and 15% noise to the gravity response of the sedimentary basin model (Figures 4a, 5a) by the following equation:

$$g_{noise}(x_i)=g(x_i)+M(rand(i)-0.5) \quad (15)$$

Where $g_{noise}(x_i)$ is the noisy gravity anomaly value at x_i, M controls the noise level and *r and* (i) is a pseudo-random number that its range varies between 0 to 1.

The gravity response corresponding with the inverted depth using IPSO has been displayed in Figures 4a, 5a. Figures 4b, 5b depict the assumed depths and estimated ones using IPSO for each prism by the contaminated gravity data with 10% and 15% added noise. Figures 4c, 5c show the error change versus iteration number. The numerical results of the IPSO inversion for noisy data are given in Table 2. The estimated misfit at the last iteration is 0.1075 and 0.1397 percent.

The generated gravity anomaly using the Marquardt method is shown in Figure 6a. Figure 6b illustrates the assumed and estimated depths using the Marquardt method for each prism. The generated gravity anomaly using the Marquardt method with 10% and 15% added noise was shown in Figures 7a, 8a. Figures 7b, 8b illustrate the assumed and estimated depths for each prism using the Marquardt method. The Marquardt inversion numerical outputs (with and without noise) are summarized in Table 3. Percent error of calculated and observed gravity, using the Marquardt method, for noise-free data, 10 %, and 15% noise is 0.006, 0.126, and 0.174 respectively.

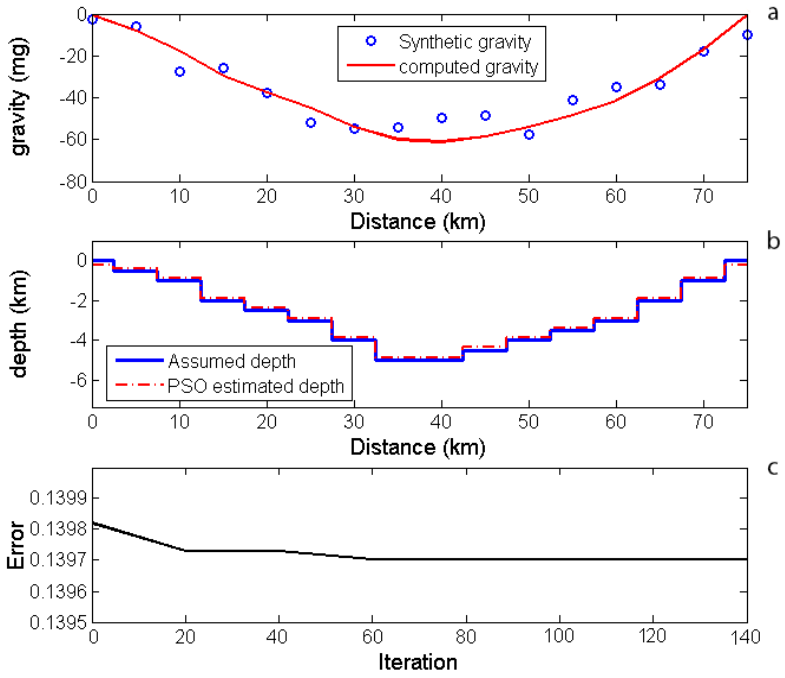

Figure 5. **(a**) Synthetic gravity data with 15% added noise and computed gravity due to **(b)** assumed and interpreted basement model by IPSO. **(c)** Error changes estimated by objective function versus iteration number

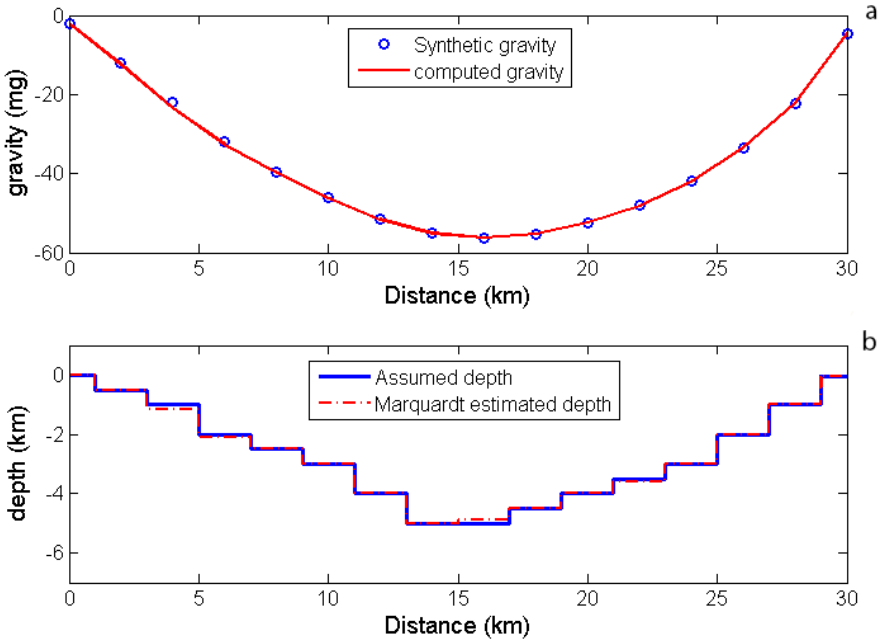

Figure 6. **(a)** Synthetic and computed gravity due to **(b)** assumed and interpreted basement model by Marquardt

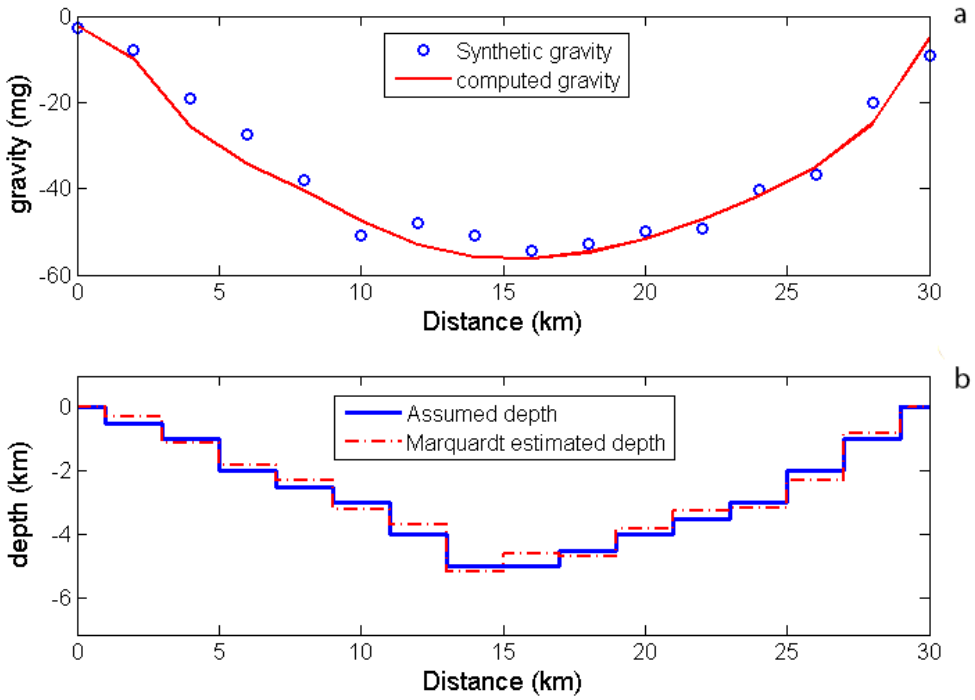

Figure 7. **(a)** Synthetic gravity data with 10% added noise and computed gravity due to **(b)** assumed and interpreted basement model by Marquardt

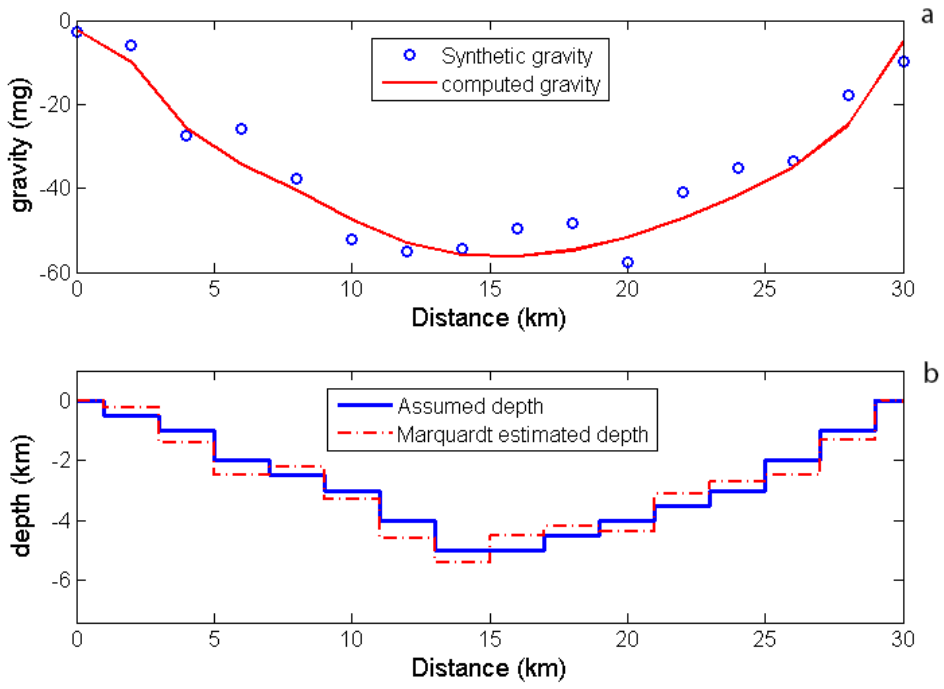

Figure 8. **(a)** Synthetic gravity data with 15% added noise and computed gravity due to **(b)** assumed and interpreted basement model by Marquardt

Table 3. The values of assumed ranges for depths and inverted depths using Marquardt, while the data are noise-free and corrupted with noise

Prism	Initial depth (km)	Estimated depth (km) (noise-free)	Percent error	Estimated depth (km) (with 10% noise)	Percent error	Estimated depth (km) (with 15% noise)	Percent error
z_2	0.5	0.5	0	0.3	40	0.25	50
z_3	1	1.15	15	1.1	10	1.4	40
z_4	2	2.1	5	1.8	10	2.5	25
z_5	2.5	2.5	0	2.3	8	2.2	12
z_6	3	3	0	3.2	10	3.3	10
z_7	4	4	0	3.7	7.5	4.6	15
z_8	5	5	0	5.15	3	5.4	8
z_9	5	4.9	2	4.6	8	4.5	10
z_{10}	4.5	4.5	0	4.7	4.4	4.2	6.67
z_{11}	4	4	0	3.8	5	4.35	8.75
z_{12}	3.5	3.6	2.86	3.25	7.14	3.1	11.4
z_{13}	3	3	0	3.15	5	2/7	10
z_{14}	2	2	0	2.3	15	2.5	25
z_{15}	1	1	0	0.8	20	1.3	30

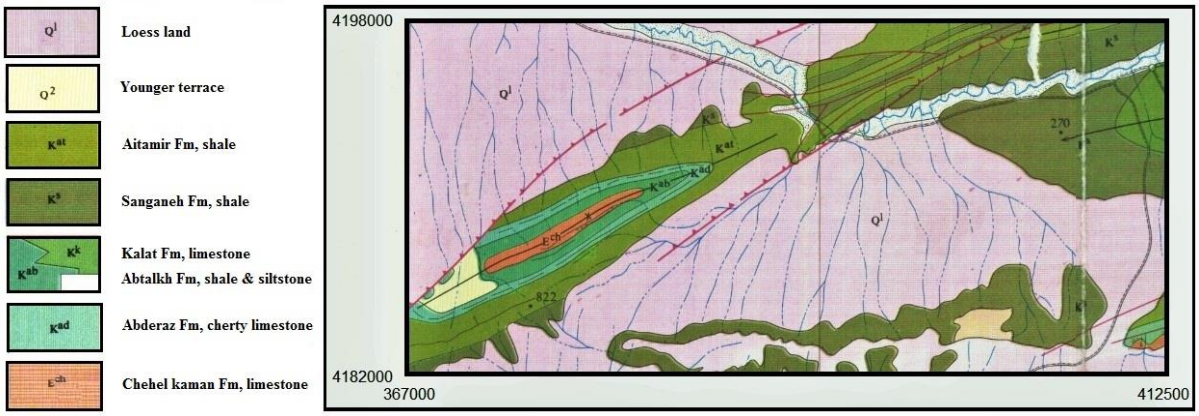

Figure 9. Geological map of studied area. Scale 1:250000 (Geological survey and mineral exploration of Iran)

Field Example

The region under investigation is located in Golestan Province, northeastern Iran onto UTM zone 40N, between 367000-412500m E and 4182000-4198000m N. This region lies on the Kopet-Dagh basin and structural unit covered by the quaternary thick sediments and rock units of Cretaceous Period. The Figure 9 shows a geological map of the studied area. The Cretaceous sediments of the Kopet-Dagh basin comprise Shurijeh, Trigan, Sarcheshmeh, Sanganeh, Aitamir, Abderaz, Abtalkh, Neyzar and Kalat formations. This general stratigraphy has been shown in Figure 10. The Tirgan formation is mainly formed by oolitic and bioclastic limestone with subordinate layers of marl, marine

limestone, and calcareous shale. It forms the basement of the sedimentary basin because of its rigidity and erosion resistance.

In order to study the geological structures such as anticline and syncline (that can capture pockets of hydrocarbons in the bend of the arch) and determine the thickness of the sediments, the gravity data sampling was done along 2 profiles with the interval of 1.5 km along profiles A, B by using LaCoste and Romberg gravimeter with an accuracy of 0.01 mGal. The distance between profiles is approximately 2 km. The values of $\Delta\rho_0, \alpha$ are assumed as -0.65 g/cm^3 and 0.08 g/cm^3/km, respectively using geological information.

Figure 11 shows the Bouguer gravity anomaly map of the studied region. The residual gravity anomaly was obtained by separating the effect of the regional gravity anomaly from the Bouguer gravity anomaly (Figure 12)

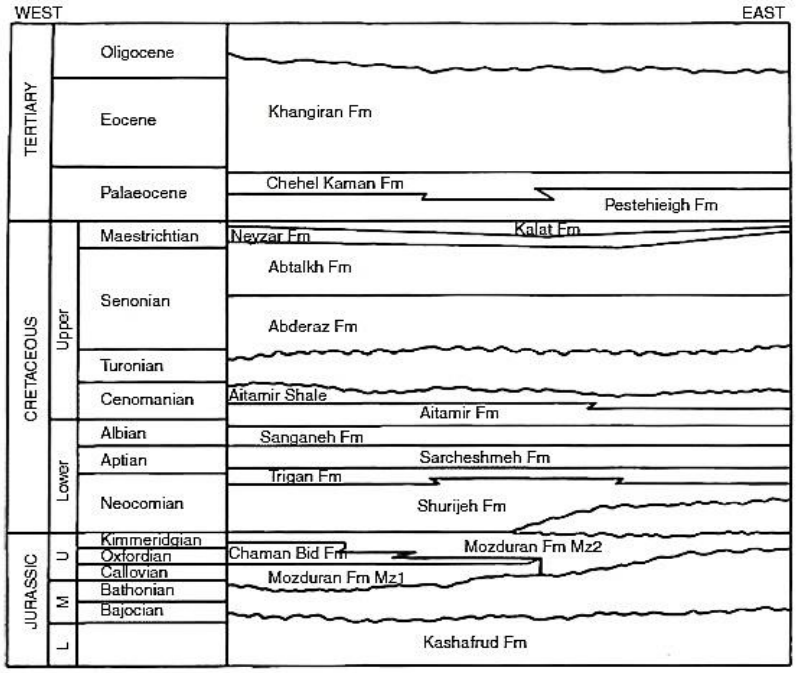

Figure 10. General stratigraphy of the Kopet-Dagh basin (Margottini et al., 2013)

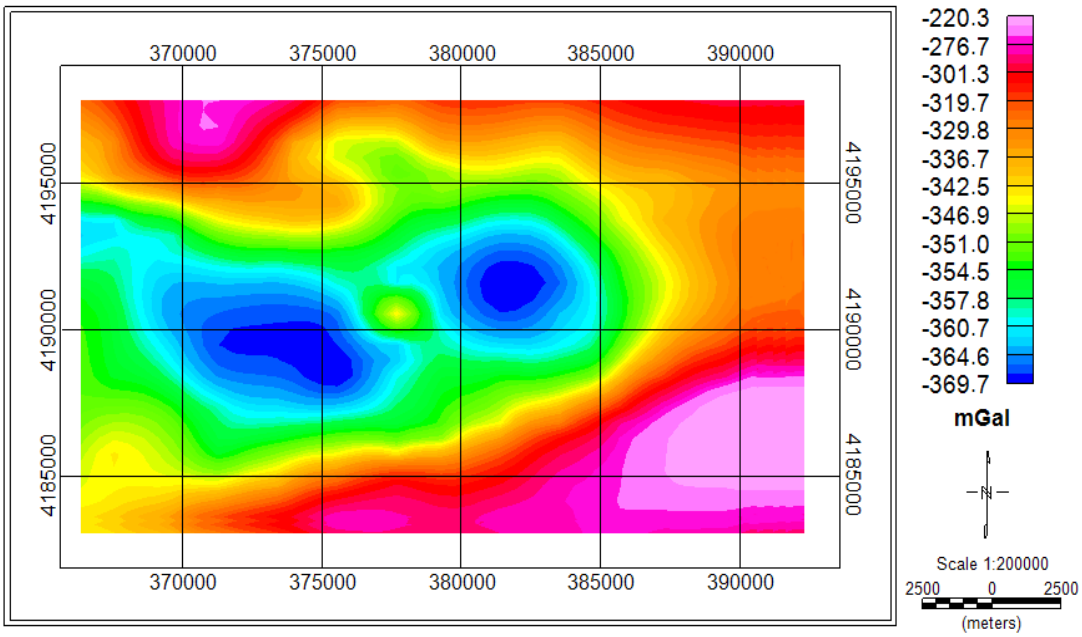

Figure 11. The Bougure gravity anomaly map of the understudied region

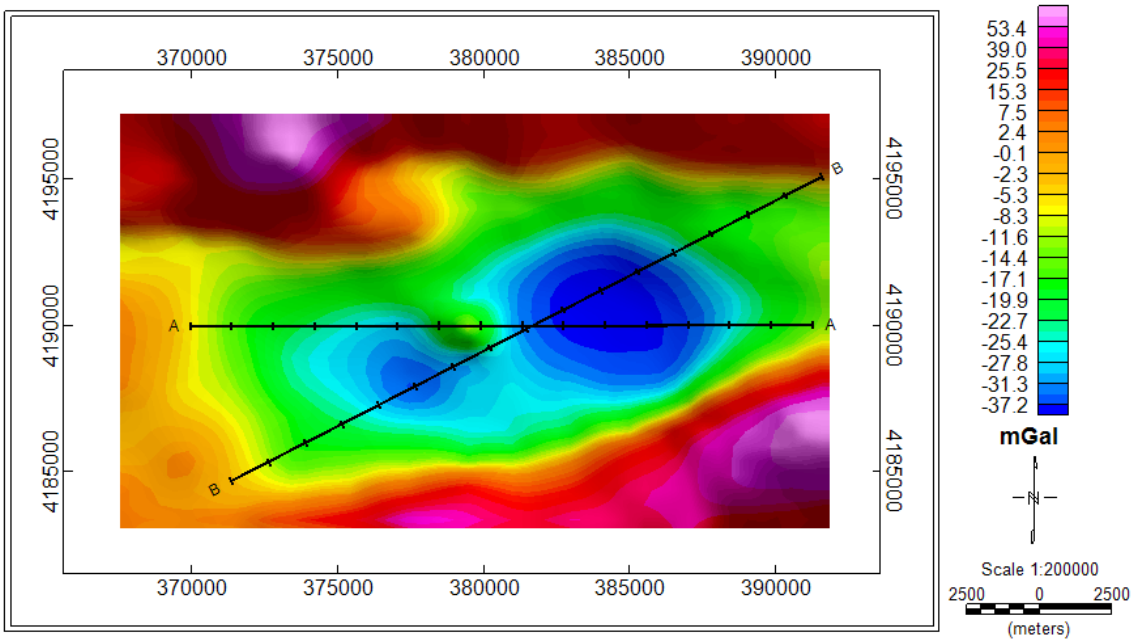

Figure 12. The residual gravity anomaly map (the position of profile A and prisms have been shown)

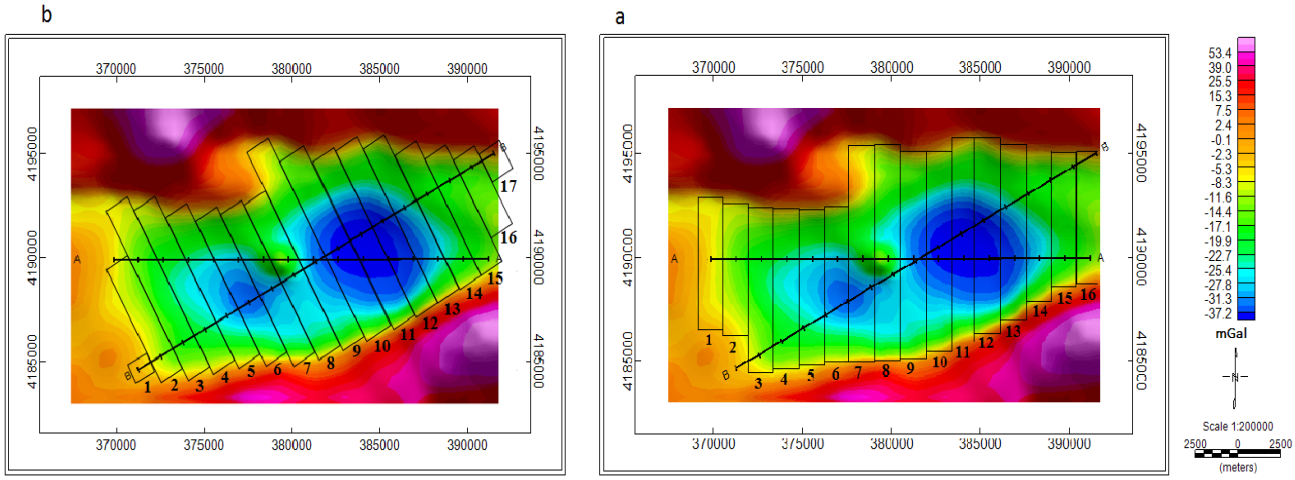

Figure 13. The simulation of the sedimentary basin using juxtaposed prisms along **(a)** profile A, **(b)** profile B

The extensive negative anomaly noticeable in the residual gravity map center is related to a sedimentary basin structure. Two profiles (A, B) are considered on negative anomaly for modeling the shape and basement depth with lengths 24.5 and 22 km. Figure 13 shows the simulation of the sedimentary basin using juxtaposed prisms along profiles A, B. The gravity data sampling was carried out at 16, 17 stations with an interval of 1.5 km along profiles A, B for inverse modeling using IPSO algorithm. The considered ranges for the depth of each prism along profiles A, B have been given in Tables 4 and 5. The number of iterations and predefined error of gravity are considered as 100 and 0.01 mGal, respectively. The generated gravity anomaly using IPSO algorithm has been demonstrated in Figures 14a, 15a along profiles A, B. Figure 14b, 15b illustrated the assumed and estimated depths for each prisms using IPSO algorithm. The inverted depths using IPSO have been written in Tables 4 and 5. Figure 14c and 15c, show the changes of error estimated by objective function versus the number of iteration. The estimated misfit at the last iteration is 0.141 and 0.0782 percent along profiles A, B respectively.

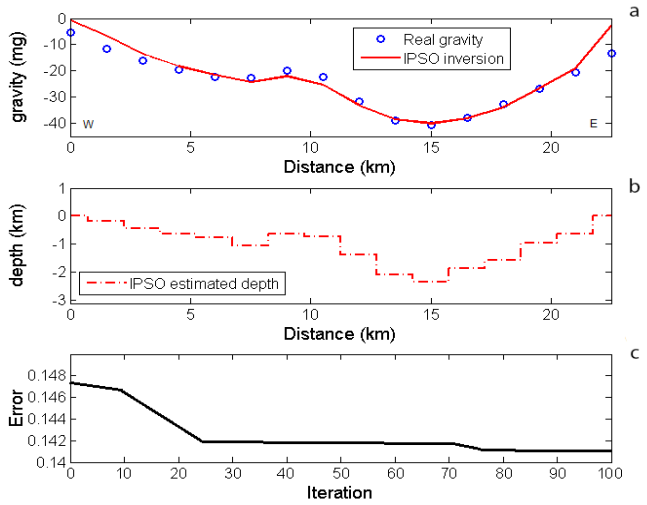

Figure 14. (a) Real gravity along profile A and computed gravity **(b)** interpreted basement model by IPSO. **(c)** Changes of error estimated by objective function versus number of iteration

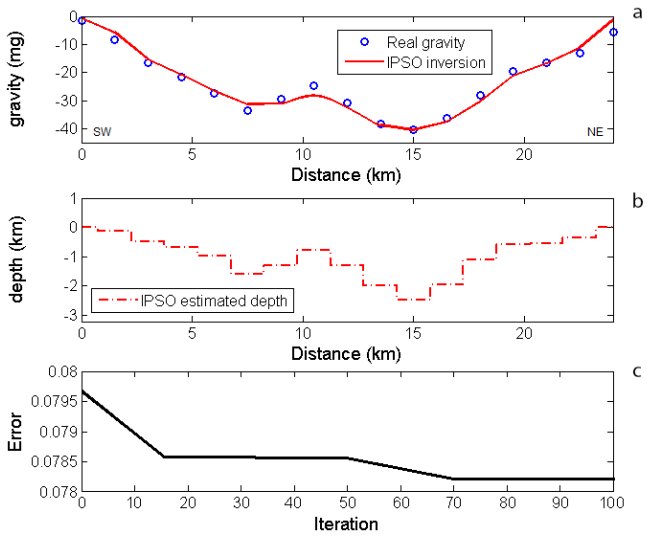

Figure 15. (a) Real gravity along profile B and computed gravity **(b)** interpreted basement model by IPSO. **(c)** Changes of error estimated by objective function versus number of iteration

Table 4. Depth ranges used in IPSO inversion of the real gravity and obtained results along profile A.

Prism	Range (km)	Result (km)	Prism	Range (km)	Result (km)
1	-	0	**9**	0.5 - 3	1.37
2	0 - 1	0.17	**10**	0.7 - 3.5	2.1
3	0.1 - 2	0.44	**11**	0.7 - 3.5	2.35
4	0.2 - 2	0.64	**12**	0.5 - 3.5	1.85
5	0.3 - 2.5	0.77	**13**	0.5 - 3	1.55
6	0.5 - 2.5	1.05	**14**	0.5 - 2.5	0.95
7	0.3 - 2.5	0.63	**15**	0.3 - 2.5	0.63
8	0.3 - 2.5	0.74	**16**	-	0

Table 5. Depth ranges used in IPSO inversion of the real gravity and obtained results along profile B.

Prism	Range (km)	Result (km)	Prism	Range (km)	Result (km)
1	-	0	**10**	0.7 - 3.5	2
2	0 - 1	0.12	**11**	0.7 - 4	2.47
3	0.1 - 2	0.49	**12**	0.5 - 3.5	1.98
4	0.2 - 2	0.69	**13**	0.5 - 3	1.11
5	0.3 - 2.5	0.99	**14**	0.5 - 2.5	0.59
6	0.5 - 3.5	1.61	**15**	0.3 - 2.5	0./54
7	0.3 - 2.5	1.31	**16**	0.1 - 2	0.34
8	0.3 - 2.5	0.79	**17**	-	0
9	0.5 - 3	1.308			

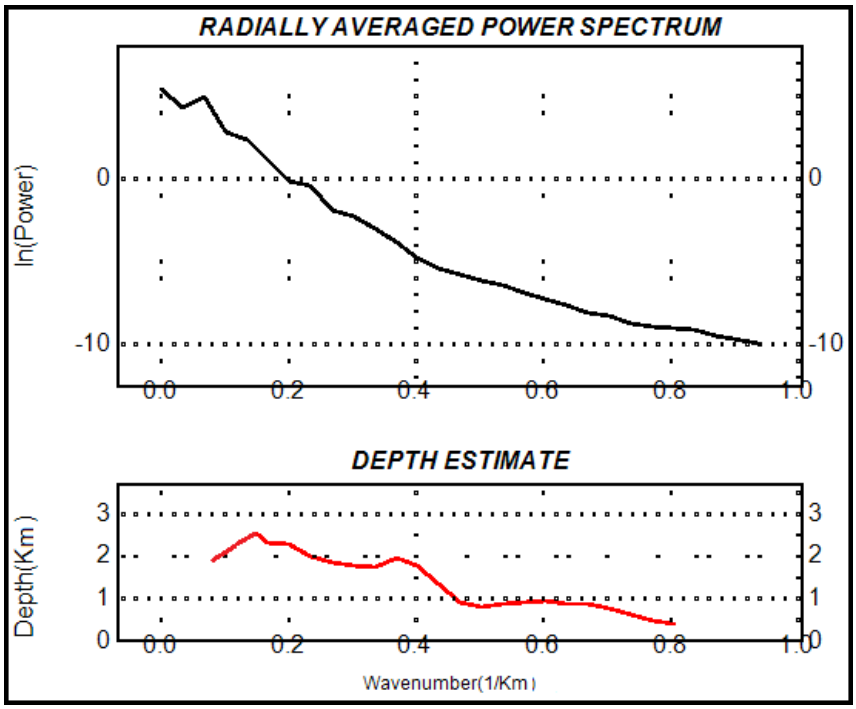

Figure 16. Estimated depth of sedimentary basin using power spectral density

The power spectral density is a common method for calculating the depth of gravity anomaly that can be estimated mean depth and thickness of subsurface anomaly using the power spectral density shape. Spector and Grant (1970) stated that the depth factor invariably dominates the shape of the radially averaged power spectrum of potential field data. Here, 'radially averaged' means that the powers for equal lengths of the wave vector are averaged. This statement has paved the way for a very convenient interpretation of the power spectrum of potential field data. The radially averaged power spectrum of the field in a 2-D observation plane decreases with increasing depth to source *t* by a factor exp (*-2tr)*, *r* being the wave number. Hence, if the depth factor dominates the shape of the power spectrum, the logarithm of the power spectrum should be proportional to *-2tr*, and the depth to source can be derived directly from the slope of the log radially averaged power spectrum.

Figure 16 demonstrates the power spectral density curve of the field under analysis and the calculated maximum depth using the curve. The maximum depth of the sedimentary basin basement is approximately estimated 2.5 km using the power spectral density method.

CONCLUSION

In this paper, to avoid premature convergence to local optimality and increase convergence speed, we have proposed the IPSO algorithm. For this aim, the inertia weight coefficient (w) and learning factors (c_1,c_2) are improved. Also, we have utilized the IPSO to estimate the depth of sediments using the gravity data, where the density contrast is supposed to be changing parabolically with depth.

The IPSO and the conventional Marquardt optimization method have been used to analyze the gravity data of the sedimentary basin and their results have been compared. By adding 10% and 15% random noise to gravity data, the efficiency of these methods was investigated. One of the notable advantages of the IPSO algorithm is the determination of the range for the model parameters that causes the calculated model parameters (depth and gravity of the synthetic model) do not differ too much from the assumed values due to set limits for model parameters and are always within the range which are derived through using geological data and interpreter experience. The Marquardt method is sensitive to noise. The gravity derivative is used in it, therefore the error rate increases by adding noise. From the comparison between the observed model parameters range with the calculated value of the model parameters and also by analyzing the misfit between the observed and calculated gravity, we concluded that the estimated depth of sedimentary basin basement using the Marquardt method was better than the IPSO algorithm for gravity data without noise, but for gravity data with noise, the IPSO algorithm was a reliable method for estimating sedimentary basin depth and simulating it rather than Marquardt method. Then, we used the IPSO algorithm for analyzing real gravity data.

The IPSO algorithm has been used to invert the gravity field of a sedimentary basin in Golestan province. The maximum depth value of the basement is estimated at 2.47 km. This depth corresponds to the obtained depth from the conventional power spectral density which has estimated the maximum depth of the studied area about 2.5 km.

ACKNOWLEDGMENTS

The authors thanks to the personnel of the Geographical Survey and Mineral Exploration of Iran who helped them with gathering data.

Compliance with Ethical Standards

The authors declare that they have no conflict of interest and adhere to copyright norms.

REFERENCES

Barbosa, V.C.F., Silva, J.B.C. and Medeiros, W.E., 1997. Gravity inversion of basement relief using approximate equality constraints on depths. Geophysics, 62(6), 1745–1757.

Bott, M.H.P., 1960. The use of rapid digital computing methods for direct gravity interpretation of sedimentary basins. Geophys. J. R. Astron. Soc, 3, 63–67.

Chakravarthi, V., 1995. Gravity interpretation of nonoutcropping sedimentary basins in which the density contrast decreases parabolically with depth. Pure Appl. Geophys., 145(2), 327–335.

Chakravarthi, V., Singh, S.B. and Ashok Babu, G., 2001. INVER2DBASE-A program to compute basement depths of density interfaces above which the density contrast varies with depth. Computers & Geosciences, 27(10), 1129–1133.

Chakravarthi, V. and Sundararajan, N., 2005. Gravity modeling of 21/2-D sedimentary basins—a case of variable density contrast. Computers & Geosciences, 31, 820–827.

Chakravarthi, V. and Sundararajan, N., 2006. Gravity anomalies of multiple prismatic structures with depth-dependent density – A Marquardt inversion. Pure Appl. Geophys., 163, 229–242.

Chakravarthi, V. and Sundararajan, N., 2007. Marquardt optimization of gravity anomalies of anticlinal and synclinal structures with prescribed depth-dependent density. Geophys. Prospecting, 55, 571–587.

Cordell, L., 1973. Gravity analysis using an exponential density–depth function—San Jacinto Graben, California. Geophysics, 38, 684–690.

Essa, K.S. and Elhussein, M., 2018. Gravity data interpretation using different new algorithms: A comparative study. Gravity-Geoscience Applications, Industrial Technology, and Quantum Aspect, Licensee InTech.

Gallardo-Delgado, L., Pérez-Flores, M. and Gómez-Treviño, E., 2003. A versatile algorithm for joint 3D inversion of gravity and magnetic data. Geophysics, 68, 949-959.

García-Abdeslem, J., 2005. The gravitational attraction of a right rectangular prism with density varying with depth following a cubic polynomial. Geophysics, 70(6), J39-J42.

Karcol, R., 2018. The gravitational potential and its derivatives of the right rectangular prism with depth-dependent density following an n-th degree polynomial. Studia Geophysica et Geodaetica, 62, 427–449.

Kennedy, J. and Eberhart, R., 1995. Particle Swarm Optimization. IEEE International Conference on Neural Networks, 4, 1942–1948.

Lin, C.J. and Liu, Y.C., 2009. Image backlight compensation using neurofuzzy networks with immune Particle Swarm Optimization.Expert Systems with Applications, 36, 5212-5220.

Margottini, C., Canuti, P. and Sassa, K., 2013. Landslide Science and Practice. Volume 1: Landslide Inventory and Susceptibility and Hazard Zoning. Springer-Verlag Berlin Heidelberg.

Marquardt, D.W., 1963. An algorithm for least-squares estimation of nonlinear parameters. J. Soc. Ind. Appl. Math, 11(2), 431–441.

Martín Atienza, B., 2001. Modelado e inversión en 2D y 3D de anomalías gravimétricas producidas por cuerpos cuya geometría y densidad de masa se describen utilizando funciones polinómicas. aplicaciones a datos gravimétricos

de Canadá y México. (Ph.D. thesis, Universidad Complutense de Madrid. Facultad de Ciencias Físicas. Departamento de Física de la Tierra, Astronomía y Astrofísica I).

Monteiro Santos, F.A., 2010.Inversion of self-potential of idealized bodies' anomalies using Particle Swarm Optimization. Computers & Geosciences, 36, 1185–1190.

Nickabadi, A., Ebadzadeh, M.M. and Safabakhsh, R., 2011. A novel particle swarm optimization algorithm with adaptive inertia weight. Applied Soft Computing, 3658–3670.

Pallero, J.L.G., Fernández-Martínez, J.L., Bonvalot, S. and Fudym, O., 2015. Gravity inversion and uncertainty assessment of basement relief via Particle Swarm Optimization. J. Appl. Geophys., 116, 180–191.

Pallero, J.L.G., Fernández-Martínez, J.L., Bonvalot, S. and Fudym, O, 2017. 3D gravity inversion and uncertainty assessment of basement relief via Particle Swarm Optimization. J. Appl. Geophys., 139, 338–350.

Pallero, J.L.G., Fernández-Muñiz, M.Z., Cernea, A., Álvarez-Machancoses, O., Pedruelo-González, L.M., Bonvalot, S. and Fernández-Martínez, J.L., 2018. Particle Swarm Optimization and uncertaintyassessment in inverse problems. Entropy, 20, 96.

Parsopoulos, K.E. and Vrahatis, M.N., 2002. Recent approaches to global optimization problems through Particle Swarm Optimization. Natural Computing, 1, 235–306.

Rao, B.S.R. and Murthy, I.V.R., 1978. Gravity and magnetic methods of prospecting. Arnold-Heinemann Publishers, New Delhi, India.

Rao, C.V., Raju, M.L. and Chakravarthi, V., 1995. Gravity modeling of an interface above which the density contrast decreses hyperbolically with depth. J. Appl. Geophys., 34(1), 63-67.

Rao, D.B., 1990. Analysis of gravity anomalies of sedimentary basins by an asymmetrical trapezoidal model with quadratic density function. Geophysics, 55(2), 226–231.

Roshan, R. and Singh, U.K., 2017. Inversion of residual gravity anomalies using tuned PSO. Geosci. Instrum. Method. Data Syst., 6, 71–79.

Samanta, B. and Nataraj, C., 2009. Use of particle swarm optimization for machinery fault detection. Engineering Applications of Artificial Intelligence, 22, 308-316.

Shi, Y. and Eberhart, R.C., 1998. Parameter selection in particle swarm optimization. In Evolutionary Programming, VII. Proceedings of EP 98, 591–600.

Silva, J.B.C., Costa, D.C.L. and Barbosa, V.C.F., 2006. Gravity inversion of basement relief and estimation of density contrast variation with depth. Geophysics, 71(5), J51–J58.

Singh, K.K. and Singh, U.K., 2017. Application of Particle Swarm Optimization for gravity inversion of 2.5-D sedimentary basins using variable density contrast.Geosci. Instrum. Method. Data Syst., 6, 193–198.

Spector, A. and Grant, F.S., 1970. Statistical models for interpreting aeromagnetic data. Geophysics, 35, 293-302.

Sweilam, N.H., El-Metwally, K. and Abdelazeem, M., 2007. Self potential signal inversion to simple polarized bodies using the Particle Swarm Optimization method: A visibility study. J. Appl. Geophys., 6, 195–208.

Talwani, M., Worzel, J.L. and Landisman, M., 1959. Rapid gravity computations for two-dimensional bodies with application to the Mendocino submarine fracture zone. J. Geophys. Res., 64, 49-59.

Toushmalani, R., 2013a. Comparison result of inversion of gravity data of a fault by Particle Swarm Optimization and Levenberg–Marquardt methods. Springer Plus, 2, 462.

Toushmalani, R., 2013b. Gravity inversion of a fault by Particle Swarm Optimization (PSO). SpringerPlus, 2, 315.

Xin, J., Chen, G. and Hai, Y., 2009. A Particle Swarm Optimizer with multistage linearly-decreasing inertia weight. International Joint Conference on Computational Sciences and Optimization, 1, 505–508.

Yi, L., 2016. Study on an Improved PSO algorithm and its application for solving function problem. Int. J. Smart Home, 3, 51-62.

Zahara, E., Fan, S.K.S. and Tsai, D.M., 2005. Optimal multi-thresholding using a hybrid optimization approach. Pattern Recognition Lett., 26, 1082-1095.

Zhang, Y., Yan, J., Wei, G. and Wu, L., 2010a. Find multi-objective paths in stochastic networks via chaotic immune PSO. Expert Systems with Applications, 37, 1911-1919.

Zhang, Y., Wang, S. and Wu, L., 2010b. PSONN used for remote-sensing image classification. J. Computational Information Systems, 6, 4417- 4425.

Received on: 12.06.2021; Revised on: 28.12.2021; Accepted on: 30.12.2021

J. Ind. Geophys. Union, 26(1) (2022), 23-40

Regional gravity and magnetic surveys in parts of Belgaum, Bijapur, Dharwar and Raichur districts, Karnataka (India)

D.C. Naskar*, S.V.N. Chandrasekhar, Anshika Sharma, and M. Purushottam

Geological Survey of India, Southern Region, Hyderabad-500068
*Corresponding author: dcnaskar@yahoo.com

ABSTRACT

Regional geophysical survey, employing gravity and magnetic methods, have been carried out in 2160 sq km area of Western Dharwar Craton (WDC). The objective of the survey was to delineate subsurface structural features. The Bouguer anomaly (BA) map has brought out negative gravity anomaly with amplitude of 29 mGal in the range from -78 mGal in the eastern part to -107 mGal. The area surveyed is characterized by high gravity anomaly towards northern and east central part and low to medium gravity anomaly in the west central and southern part, except a small gravity high closure near Yankachi. The elongated residual high gravity nosing trending in nearly NW-SE direction in the central portion and flanked by residual gravity lows on either side, is inferred as basement high below Kaladgi Supergroup of sediments. Similarly, magnetic anomaly (TF) map shows bipolar magnetic anomalies in the northern and east central parts; magnitude of anomalies ranging between -81 nT to 488 nT. Presence of wide spread Kaladgi Supergroup of sediments in the central and southern part of the studied region, may have contributed for low to medium intensity magnetic anomaly except a major high south of Bagalkot in the southern part. High intensity magnetic anomaly closure around Yankachi, reflected as a zone of high analytic signal, may be attributed to Hungund schist belt towards east central part. The radially averaged power spectrum of gravity data has brought out two interfaces at depths of around 8.33 km and 3.12 km, and for magnetic data one interface at the depth of 2 km respectively. The interfaces brought out by both the gravity as well as magnetic data, may represent the range of basement depth (2-8.33 km) in the western part of Dharwar Craton. The linear clustering, trending in N-S direction of Euler depth solutions towards west central part, NE-SW trending linear cluster around Bilji-Kolhar towards central part and NW-SE trending towards northern part in Kolhar-Kakhandaki-Babaleshwar section, whereas curvilinear clustering around north of Girisagar in the central part and south of Katgeri in the southern part have been brought out. These linear and curvilinear clustering may be inferred as geologic/faulted contacts warrants for detailing the area.

Keywords: Gravity and magnetic studies, Dharwar Craton, Euler 3D solutions, Geologic structures, Indian shield

INTRODUCTION

The South Indian Shield forms a coherent unit in which geological activity can be traced continuously over the entire Precambrian. It records more than a billion years of the early history of the Earth, involving several episodes of crustal development. The Dharwar Craton is located in the central part of the South Indian Shield, flanked by the high-grade granulitic terrain to the south and the younger cover of the Deccan flood basalts to the north. This craton can be divided into two distinct tectonic blocks: the Western Dharwar Craton (WDC) and Eastern Dharwar Craton (EDC) (Naqvi and Rogers, 1987; Swaminath and Ramakrishnan, 1981). Swaminath et al. (1976) marked an arbitrary boundary between both the blocks parallel to the western margin of Closepet granite, which was subsequently modified that coincide with the Chitradurga boundary fault and confirmed by Deep Seismic Sounding (DSS) (Kaila et al., 1979) and Landsat imagery (Drury and Holt, 1980). Manikyamba and Kerrich (2012) carried out geological study over eastern Dharwar Craton and reinterpreted it as composite tectonostratigraphic terranes of accreted plume-derived and convergent margin-derived magmatic sequences based on new high-precision elemental data. The Kushtagi greenstone belt (KGB) occurs in the central part of the EDC and is the northern continuation of the 400 km long Ramagiri-Hungund composite greenstone belt. A shear zone passes through the centre of the belt along which numerous gold occurrences are found (Manikyamba et al., 2004b). Matin (2006) studied the tectonic of Hungund-Kushtagi schist belt and opined that this relatively unknown schist belt is characterized by two major episodes of deformation. Qureshy et al. (1967) have noted that the gravity highs in this region are located over the schist belts and the moderate gravity lows are associated with the exposures of the granites and gneisses. Subrahmanyam and Verma (1982) proposed that the crust on the western part of the Dharwar Craton might be thicker than to the east of the Chitradurga Boundary Fault. The teleseismic studies (Gupta et al. 2003) report much thicker crust (42-51 km) beneath the West Dharwar Craton. Srinagesh and Rai (1996) observe that the seismic velocities at a depth of 40–180 km, corresponding to the upper mantle, are higher in the western block than those in the eastern block by about 2-3 per cent. The geoelectric model is suggestive of a suture along the Chitradurga-Gadag schist belt, formed by the thrusting of the West Dharwar Craton beneath its eastern counterpart (Gokarn et al., 2004). From the borehole studies, Roy and Rao (2000) and Gupta et al. (1991) have observed that the surface heat flows are higher in the Eastern Dharwar Block than the West Dharwar Block. The thickness of the lithosphere estimated from these studies is more than 200 km. Magnetic susceptibility map of the Dharwar region is obtained using the aeromagnetic anomalies to characterize the rock formations (Harikumar et al., 2000).

The present work (Longitudes 75°30' - 75°45' E and Latitudes 16°00' - 16°45' N; 47 P/10, 11 and 12) is an effort towards delineating the variations in lithology and structure would give rise to density and susceptibility contrasts invoking gravity and magnetic (GM) studies to bring out subsurface geological architecture (Figure 1). Structurally weak zones in the belt are common exploration targets, which act as locales for possible mineral-charged hydrothermal deposits.

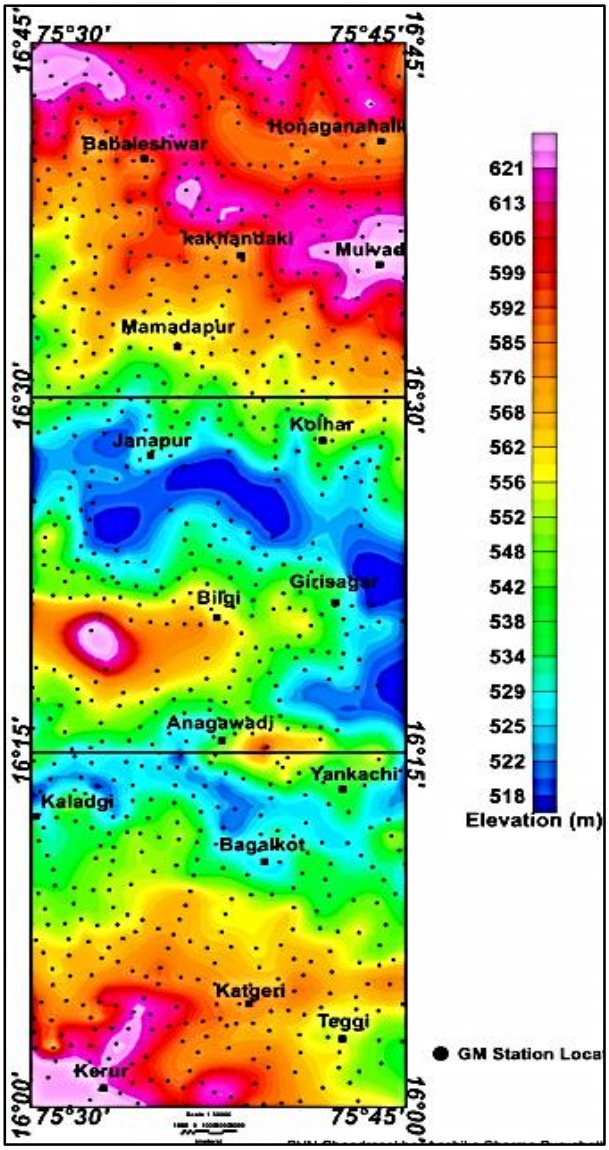

Figure 1. Location of GM stations along with elevation in parts of Belgaum, Bijapur, Dharwar and Raichur districts, Karnataka.

GEOLOGY OF THE STUDY AREA

The crustal evolution of the South Indian Shield may have been influenced by the Early Paleozoic pan-African orogenic activity (Boger et al. 2002) in which the Indian Plate, then a part of the East Gondwana Block, was involved and also the hotspot activity of the Marion and Reunion hotspots during the Late Cretaceous. The outburst of the Marion hotspot caused the break-up of Madagascar from the Indian continent (Kumar et al., 2001). The outburst of the Reunion hotspot at 65.5 Ma (Raval and Veeraswamy 2000) caused widespread fissure eruption of the Deccan flood basalts.

Geologically, the study area comprises rocks of varied nature belonging to Dharwar Supergroup, granite gneisses, Kaladgi Supergroup and Deccan trap ranging in age from Archaean to Cenozoic (Figure 2). The entire Dharwar Craton can be viewed as a matrix of Peninsular gneisses interspersed with high-and low-grade schist belts and the intrusive granites. Hungund-Kushtagi represents the Dharwar Supergroup and comprises of metabasalt, quartz-chlorite-sericite schist, rhyolite/quartz porphyry, banded iron formation. No age information is available for the rocks of this belt; however, U-Pb zircon and titanite ages are available for the felsic volcanics and surrounding granitoids of Ramagiri belt (Balakrishnan et al., 1999), which is the southern end of Ramagiri-Hungund composite greenstone belt. Geochemical and Nd isotopic studies on the granitoids surrounding this belt suggest distinct crustal histories on either side of the belt and subsequent juxtaposition due to lateral accretion (Dey et al., 2012). Geochemical signatures of the metabasalt of this belt suggest high-Mg tholeiitic

nature, whereas the felsic volcanic rocks are comparable to adakites (Naqvi et al., 2006). The E-W trending Kaladgi-Badami Basin is a Proterozoic intracratonic basin of the Western Dharwar Craton located along its northern edge. Jayaprakash et al. (1987) studied lithostratigraphy of the Kaladgi-Badami basin. Panduranga (1981) carried out systematic geological mapping in parts of Bijapur taluk, Bijapur district Karnataka. In TS 47P/12, specialized thematic mapping of the simikere subgroup of Kaladgi Group of sediments in parts of Bagalkot district, Karnataka was carried out by Raju (2010) The Hungund-Kushtagi Group of rocks has been intruded by granite and basic gabbro dykes. Rocks of Kaladgi Supergroup rests unconformably over the Peninsular Gneissic Complex (PGC) of Archaean age and the Deccan traps of Cretaceous to tertiary age unconformably overlie it. The sedimentary fill of the Kaladgi Basin comprises the Kaladgi Supergroup, which consists of Meso-Neoproterozoic shallow marine to fluvial deltaic and terrestrial basin margin sediments. While the Kaladgi Supergroup sediments unconformably overlie the Archaean basement Peninsular Gneiss and Dharwar Supergroup units in the south, towards north the sediment package is concealed under the Deccan Traps. The sedimentary sequence in the Kaladgi Supergroup has been divided along an angular unconformity surface into two groups; the lower Bagalkot Group and the overlying Badami Group. The generalized stratigraphic sequence of the study area is given in Table 1 (Raju, 2010).

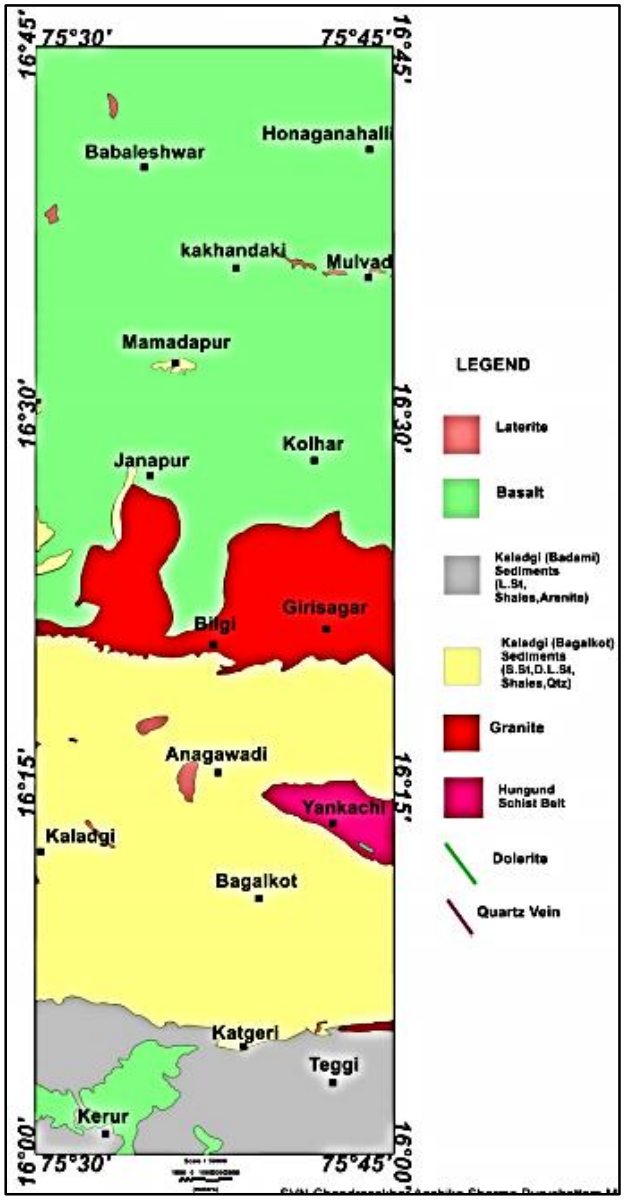

Figure 2. Geological map in parts of Belgaum, Bijapur, Dharwar and Raichur districts, Karnataka.

Table 1. Generalized geological succession.

Lithounit	Formation	Group	Supergroup	Age
Laterite				Cenozoic
Basalt flow	Purandargarh		Deccan trap	Upper Cretaceous to Paleocene
Limestone, shale, arenite	Katageri	Badami	Kaladgi	Neoproterozoic
Arenite, conglomerate	Kerur	Bagalkot		
Argillite, limestone, dolomite	Yendegiri			
Dolomite, argillite	Yargatti			
Chert breccia, argillite	Malprava			Mesoproterozoic
Argillite, quartzite	Ramdurg			
Dolerite, gabbro, quartz vein	Younger intrusive			Paleoproterozoic
Hornblende-biotite granite, pink porphyritic granite, pink granite, grey granite, grey biotite granite		Closepet granite		Archaean to Paleoproterozoic
Anorthositic gabbro, metagabbro	Kalmangi			Archaean
Rhyolite, metabasalt	Ilkal	Hungund-Kushtagi	Dharwar	
Banded iron formation, argillite, rhyolite, quartzchlorite-sericite schist, quartzchlorite schist	Mudenur			
Biotite gneiss, migmatite gneiss		PGC-I	PGC	

Economic geology

Occurrences of few economic minerals/rocks are reported in the present study area (GSI, 2018). The area is endowed with rich deposits of limestone and dolomite in the Bagalkot Group, manganese and iron ore in the schist belt. Kankar is quarried locally for producing white washing material and quicklime. BMQ bands occurring extensively in the Hungund-Kushtagi belt, provide a potential resource of iron ore. The exploration of iron ore is being carried out. Quartzite, laterites, limestone/dolomite and hard and massive part of the basaltic rocks are quarried for use as road and building/construction material. Red bole material is used as pigments. A few abandoned gold mines are present near Nagavai and Beladadi. This area is known for gold occurrences and mining activities from Mysore Mine, Hosur Champion, Doni, Venkatapura, Nagavi, Nagavi north and Attikatti. Four mineralized lodes were delineated namely Middle, New East, Temple East and East West gold over a strike length of 3.85 km near Gadag. The Middle lode occurs in meta-andesite while rest are within greywacke-argillite suite of rocks. Temple East lode is more promising. It has a strike length of 2100 m and width varying from 1.71 m to 3.5 m (Raju, 2010).

GEOPHYSICAL SURVEYS

Data acquisition, processing and instruments

In the present geophysical surveys, gravity and magnetic (TF) data were recorded at 760 locations along available roads and tracks with average station interval of 1-1.5 km. CG-5 Autograv Gravimeter with resolution of 0.001 mGal equipped with real time clock and GPS receiver (Scintrex make, Canada) have been used for gravity survey. Total Field (TF) magnetometer with resolution (0.1 nT) (GSM-19T, GEM make, Canada) devised with proton-precession technique, have been used to acquire magnetic data. Measurement of elevation of gravity stations was done by Differential Global Positioning System (DGPS) (Model: Viva, Leica make, Switzerland) which is aided with GPS antenna (AS10), receiver (GS10) and control unit (CS10). Data were processed with Leica Geo Office 10.3 software for determination of station coordinates and elevation through post-processing technique, with positional and elevation accuracies of the order of 0.0005 m and 0.001m, respectively. The drift corrected gravity data are reduced to the mean sea level using International Gravity Formula-1980 (International Association of Geodesy, 1980) with reference to IGSN-71 base. IGSN base was established by GSI (GSI, 2017) in the IB Guest House, Kushtagi, Koppal district, Karnataka and it was connected to Bagalkot district, Karnataka. Average crustal density of 2.67 gm/cc is assumed for making Bouguer corrections. The IGRF corrections are applied to the magnetic data, using IGRF-10 coefficients for the '2015-20' epoch to evaluate magnetic anomaly at each station. The Oasis Montaj (vol. 8.5) package of Geosoft (2015) is used for preparation of various gravity and magnetic anomaly maps, considering World Geodetic System (WGS)-84 datum and Universal

Transverse Mercator (UTM) projection system. Bouguer gravity and magnetic anomaly maps are gridded at 1000 m interval and, contours are drawn on 1 mGal and 50 nT intervals, respectively.

Rock samples were also collected throughout the survey area for measurement of density and magnetic susceptibility values. Physical properties viz. density and magnetic susceptibility are measured (Table 2) with Electronic Balance (Afcoset, India; Model: FX-400) and MS-2 Magnetic Susceptibility Meter (Make Bartington, UK) respectively. The results have been given in the following sections.

RESULTS AND DISCUSSION

Potential field involving gravity and magnetic methods have wide applications in geophysical mapping and mineral exploration as they pick up responses from concealed geological structures, which sometimes promote formation of mineral deposits (Grant and West, 1965; Paterson and Reeves, 1985; Sharma, 1986; Blakeley, 1995; Nabighian et al., 2005).

Bouguer gravity anomaly

The present gravity survey over the western Dharwar Craton, has brought out negative gravity anomaly with amplitude of 29 mGal in the range from -78 mGal to -107 mGal (Figure 3).

The area surveyed is characterized by high gravity anomalies around Mulvad-Babaleshwar-Honaganahalli (H1) and Bagalkot-Kaladgi-Anagawadi-Yankachi (H2) areas, medium to low gravity anomaly in the central and southern part. High gravity enclave formed by closed contours with values increasing towards centre in and around Yankachi (H2) area represents an anti formal structure in the crust over schist belt. It consists of high-density materials in the core and rock sample collected shows the range of density 2.84 and 2.91 gm/cc. High gradient zone manifested by crowding of contours in Kolhar-Kakhandaki-Babaleshwar (G1) in the north and Teggi-Katgeri and further northwest (G2) section in the extreme southern part reflects existence of shear/contact zone. Existence of minor fault/shear zones or dykes is suspected from contour disposition like stretching and kinking in some places. Predominantly low gravity anomaly zone (blue shade) exists on the southern part around Katgeri-Kerur section, with gravity values ranging from -107 mGal to -102 mGal. Such low gravity anomaly values are attributable to rocks with low to moderate density rocks like Kaladgi Supergroup comprises of limestone, shale and arenite. Rock samples collected from the area reveal that density of such rocks vary between 2.52 and 2.61 gm/cc. Low gravity signature is indicative of high crustal thickness, which masks the effect of high density mantle materials occurring at greater depth. Low gravity zone with E-W trending elliptical contour pattern represents a basin-like crustal structure consisting of low-density materials. The regional Bouguer anomaly map (Figure 4) has brought out this general characteristic very well.

Table 2. Measured physical properties of rock samples in study area.

Rock type	Density (gm/cc)	(Susceptibility $\times 10^{-6}$) cgs unit
Laterite	2.83	17.8
Volcanic tuff	2.48	6
Ferruginous shale	2.95	5
Limestone	2.74	6.42
Dolomite	2.71	0.3
Metabasalt	2.98	1071
Quartzite	2.63	5.5
Argillite	2.38	124
Quartzite	2.62	4.32
Sandstone	2.62	3.7
Shale	2.68	8
Granite	2.62	150
Schist	2.91	108
BIF	3.40	3158
Phyllite	2.97	630
Basalt	2.88	1120

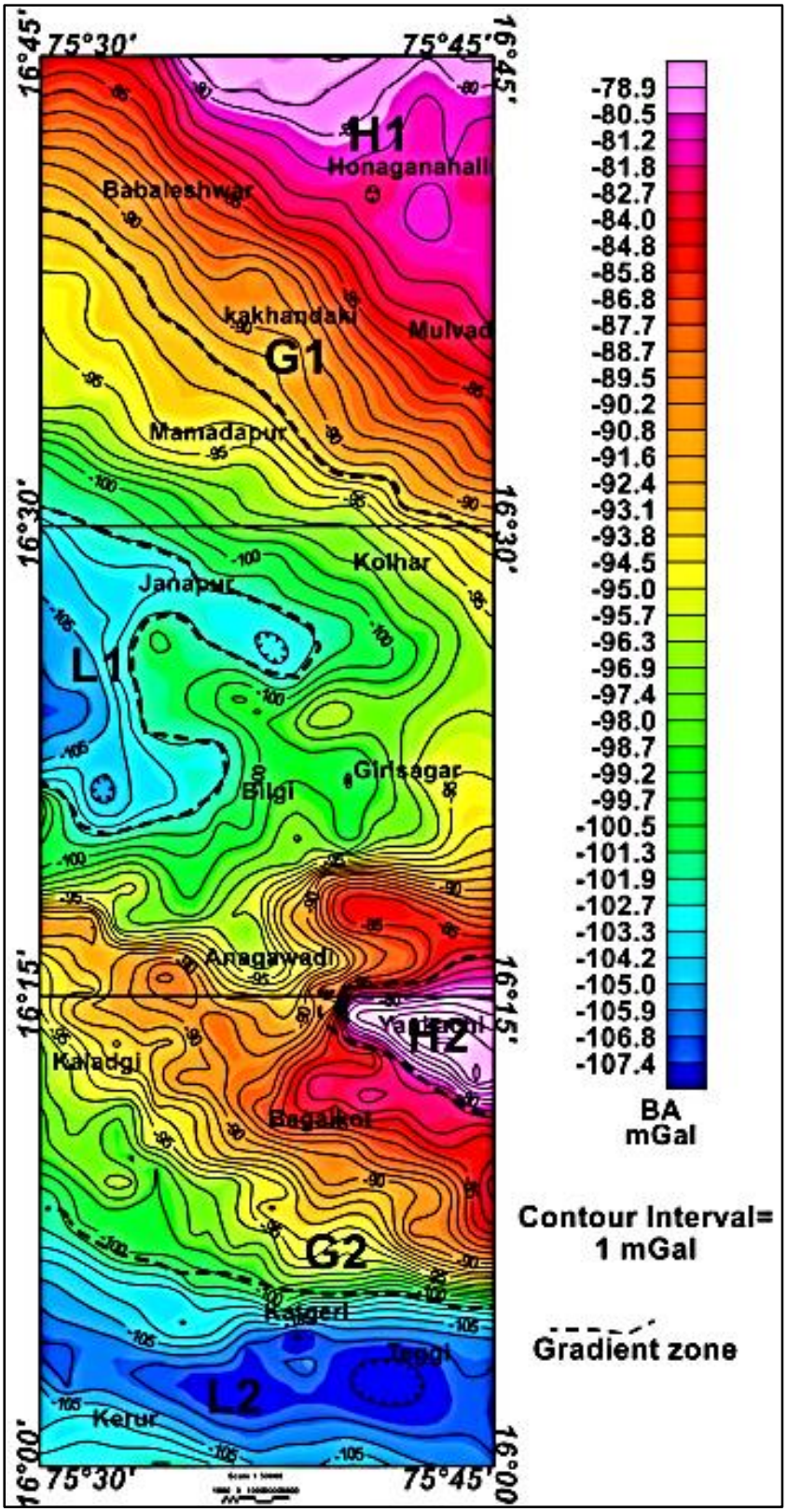

Figure 3. Bouguer gravity anomaly map in parts of Belgaum, Bijapur, Dharwar and Raichur districts, Karnataka.

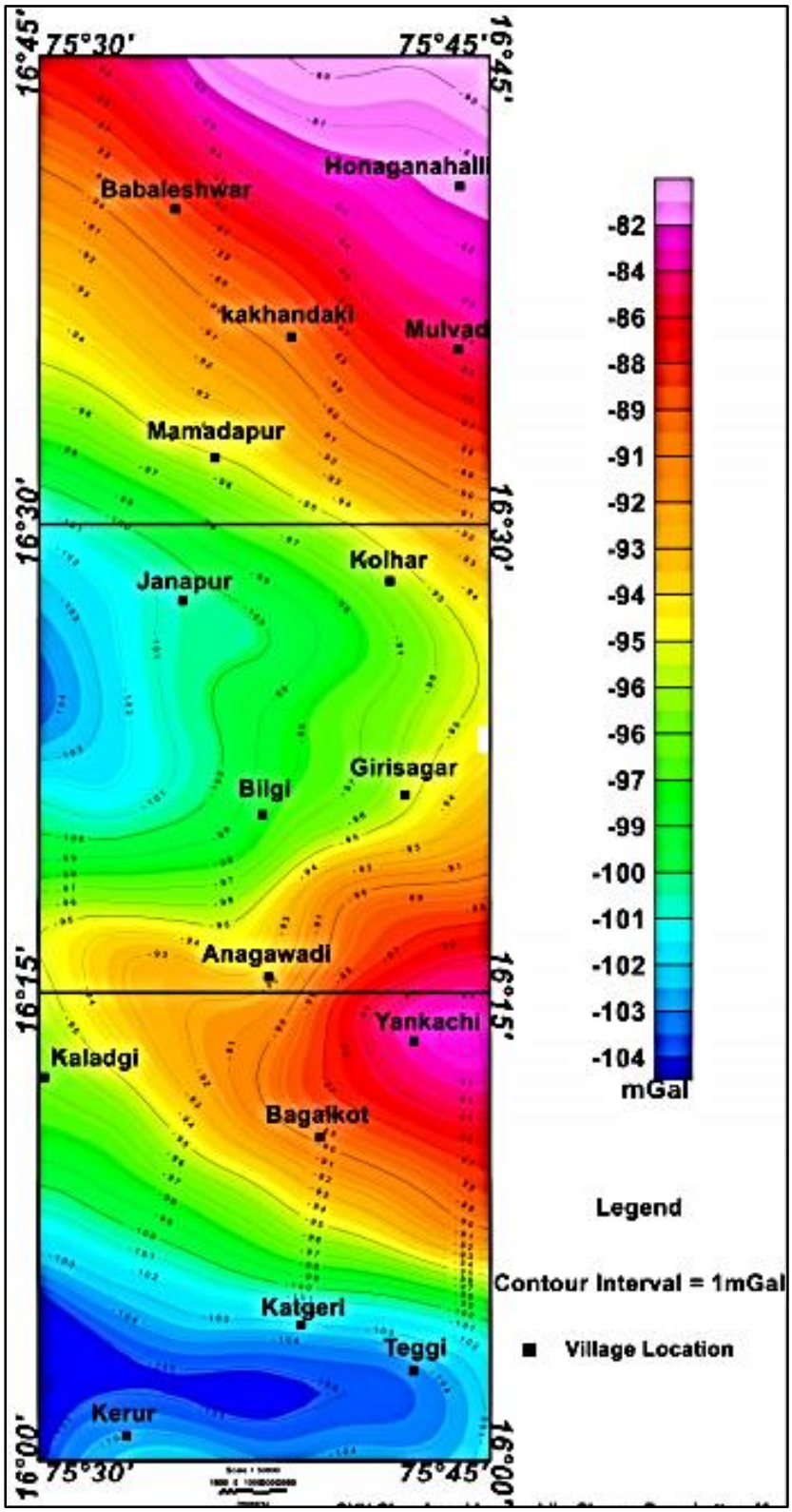

Figure 4. Regional Bouguer gravity anomaly map in parts of Belgaum, Bijapur, Dharwar and Raichur districts, Karnataka.

High gravity anomaly nosing north of Yankachi is well reflected as a high residual gravity anomaly on residual gravity map (Figure 5) as well as first order vertical derivative map (Figure 6).

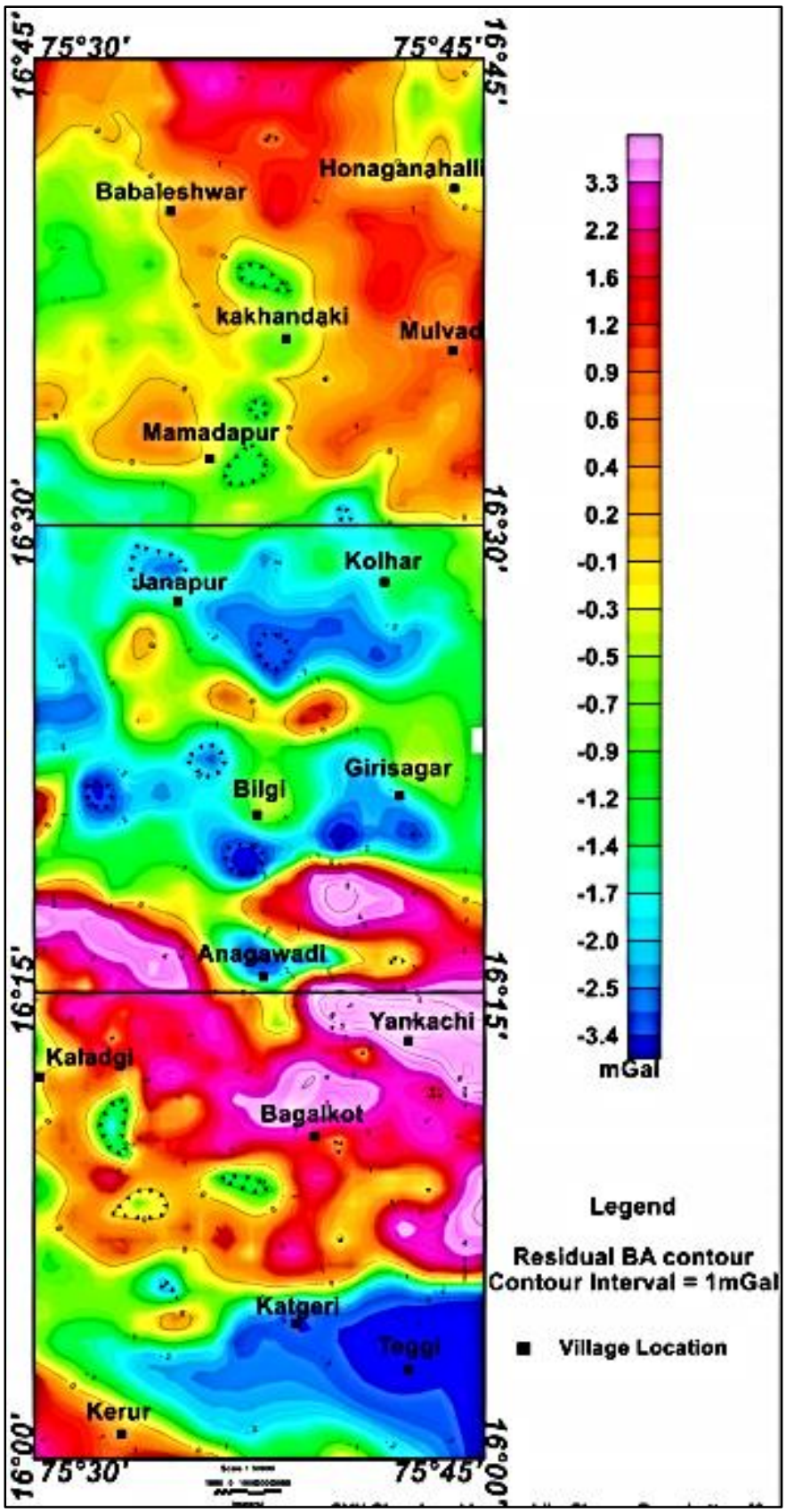

Figure 5. Residual Bouguer gravity anomaly map in parts of Belgaum, Bijapur, Dharwar and Raichur districts, Karnataka.

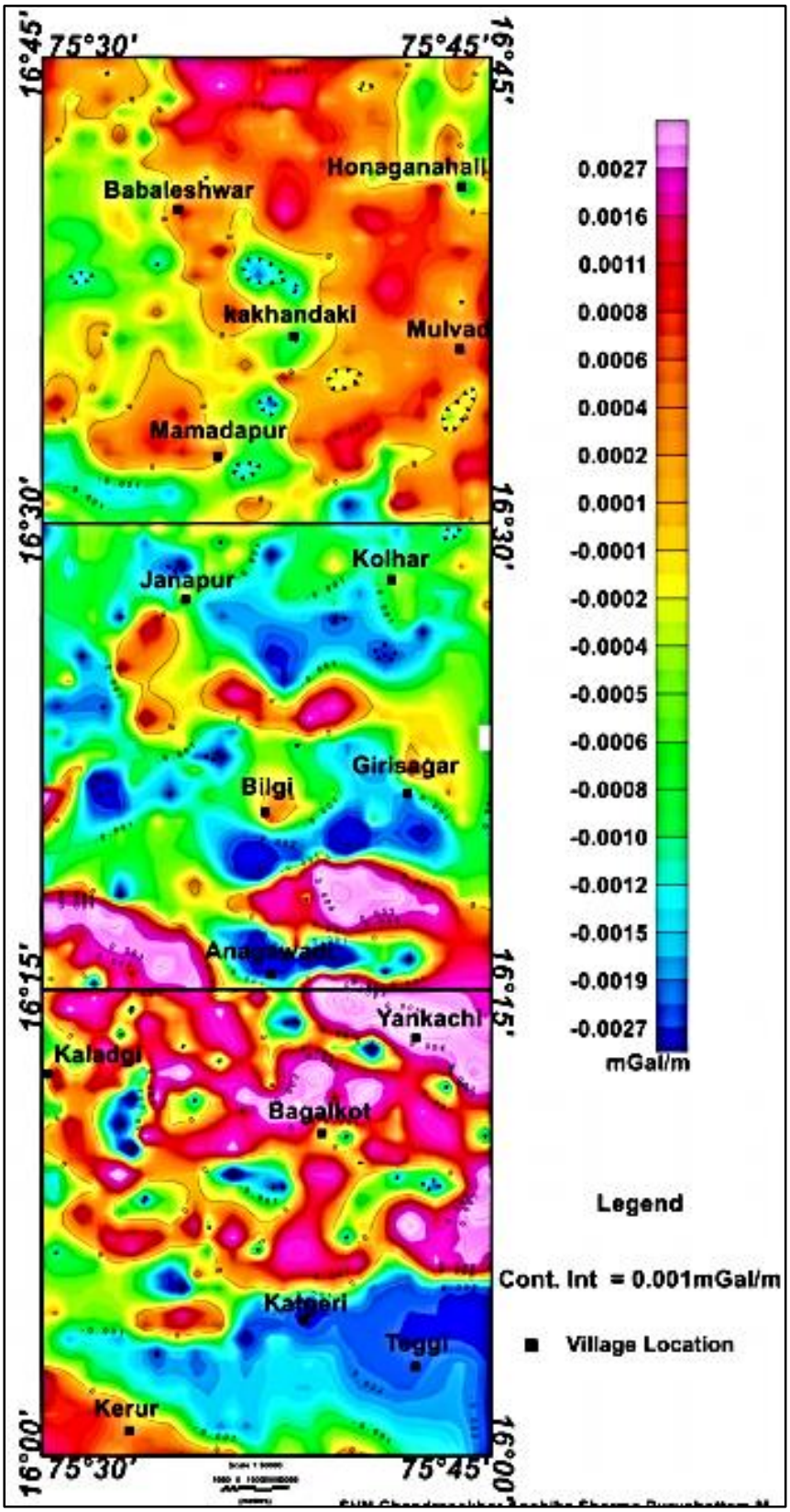

Figure 6. First order vertical derivative of Bouguer anomaly map in parts of Belgaum, Bijapur, Dharwar and Raichur districts, Karnataka.

A moderate gravity anomaly nosing prominent around northwest of Girisagar in the central portion, is well reflected as a high residual gravity anomaly on residual gravity map (Figure 5) as well as first order vertical derivative map (Figure 6). This elongated residual gravity high trending in nearly NW-SE direction and flanked by residual gravity lows on either side, is inferred as basement high below overlying basalt (density 2.88 gm/cc), granite (2.62 gm/cc) and Kaladgi sediments (2.63 gm/cc) and may assume importance for mineralization. Steep gradient contours in northern (G1) and southern (G2) parts have produced elongated residual highs (Figure 5) and prominently seen as linear gravity high on first order vertical derivative map (Figure 6). High gravity anomaly closure near Yankachi towards east on Bouguer anomaly map are prominently reflected as residual high on both residual gravity map and first order vertical derivative map (Figures 5 and 6). This residual high is interpreted as due to Hungund schist belt within the sediment cover region. NW-SE trending high gravity anomaly nosing passing through Bagalkot and extended towards southeast and northwest of it in the Bouguer anomaly map is well reflected as high residual anomaly in both residual map and derivative map (Figures 5 and 6). This feature is characterized by major shear/contact promising for deep-seated mineralization within sediment cover region. This residual high is interpreted as may be due to the extension of Hungund schist belt in the study area.

Magnetic (TF) anomaly

Magnetic anomaly (TF) map shows bipolar magnetic anomalies ranging between -81 nT to 488 nTwith (Figure 7). Northern part is dominated by medium to small amplitude bipolar anomalies (alternative bands of highs and lows). These bipolar anomalies suggest either emplacement of basic bodies along some fault planes or the faults/fractures along which concentration of magnetite is a natural phenomenon. The analytic signal map of magnetic data (Figure 8) has also brought out predominantly high magnetic anomaly peaks in this part. Upward continued magnetic anomaly map (Figure 9) also show high intensity magnetic anomaly towards northern part of the area. Rock samples (basalt) collected in this part show high order of magnetic susceptibility values of (204-1120) $\times 10^{-6}$ in cgs unit. These high magnetic anomaly peaks also seems to be caused by the basement granite gneisses composed of biotite gneiss & migmatite gneiss and Dharwar Group of rocks, which are not exposed in this part of the study area. Formational/lithological contact in between basalt (Deccan trap) and Closepet granite is clearly depicted in the magnetic anomaly map associated with bipolar anomalies and is well corroborated with high analytic signal of magnetic anomaly and regional magnetic anomaly map around Kolhar-Janapur section in the central part. High intensity magnetic anomalies (H1, H2 and H3) over basalt (Deccan trap) in the northern, sediment cover (Kaladgi Supergroup) in the eastern and southern parts and low intensity magnetic anomalies (L1 and L2) over sediments are observed. High intensity may be due to the anomalous occurrence of iron ores in the form of BIFs in these geological environments. The upward continued map also shows these general characteristic very well after removing the effect of high level of noise for shallow/surficial geological features. However, strong dipolar magnetic anomaly exists in the central and southern parts, indicating existence of magnetic body of the crust. High intensity magnetic anomaly closures around Yankachi in the eastern part over Hungund schist belt and south of Bagalkot (H3) over sediment are reflected as zone of high analytic signal of magnetic anomaly (Figure 8) and high anomaly peak in residual Bouguer anomaly map (Figure 5) respectively. These features may assume importance for mineralization. A NW-SE trending low magnetic anomaly tract (L1) northeast and southwest of Anagawadi, may be indicative of magnetic shear zone and is well reflected as high analytic signal of magnetic anomaly (Figure 8) where enrichment of magnetic minerals are postulated. Structures associated with mineralization such as folds, faults, veins and shear zones highlight the importance of a changing history of brittle and ductile deformation for economic mineralization.

Quantitative analysis of gravity and magnetic data

Radially averaged power spectrum of gravity and magnetic data

Spectral analysis of gravity and magnetic data is a conventional technique, which has wide applications in determination of depths of geological features, such as basement (Maus and Dimri, 1996) as depth of anomalous body controls the shape of power spectrum. Spectral analysis of gravity and magnetic data of study area was carried out using radially averaged power spectrum (Spector and Grant, 1970; Naidu and Mathew, 1988). The radially averaged power spectrum of gravity data (Figure 10) brought out mainly two interfaces at depths around 8.33 km and 3.12 km, whereas the spectral results of magnetic data, (Figure 11) brought out mainly one interface at depth around 2 km. The interfaces brought out both from gravity and magnetic data, may represent the range of basement depth. The estimated depth of basement within a range of 2-8.33 km.

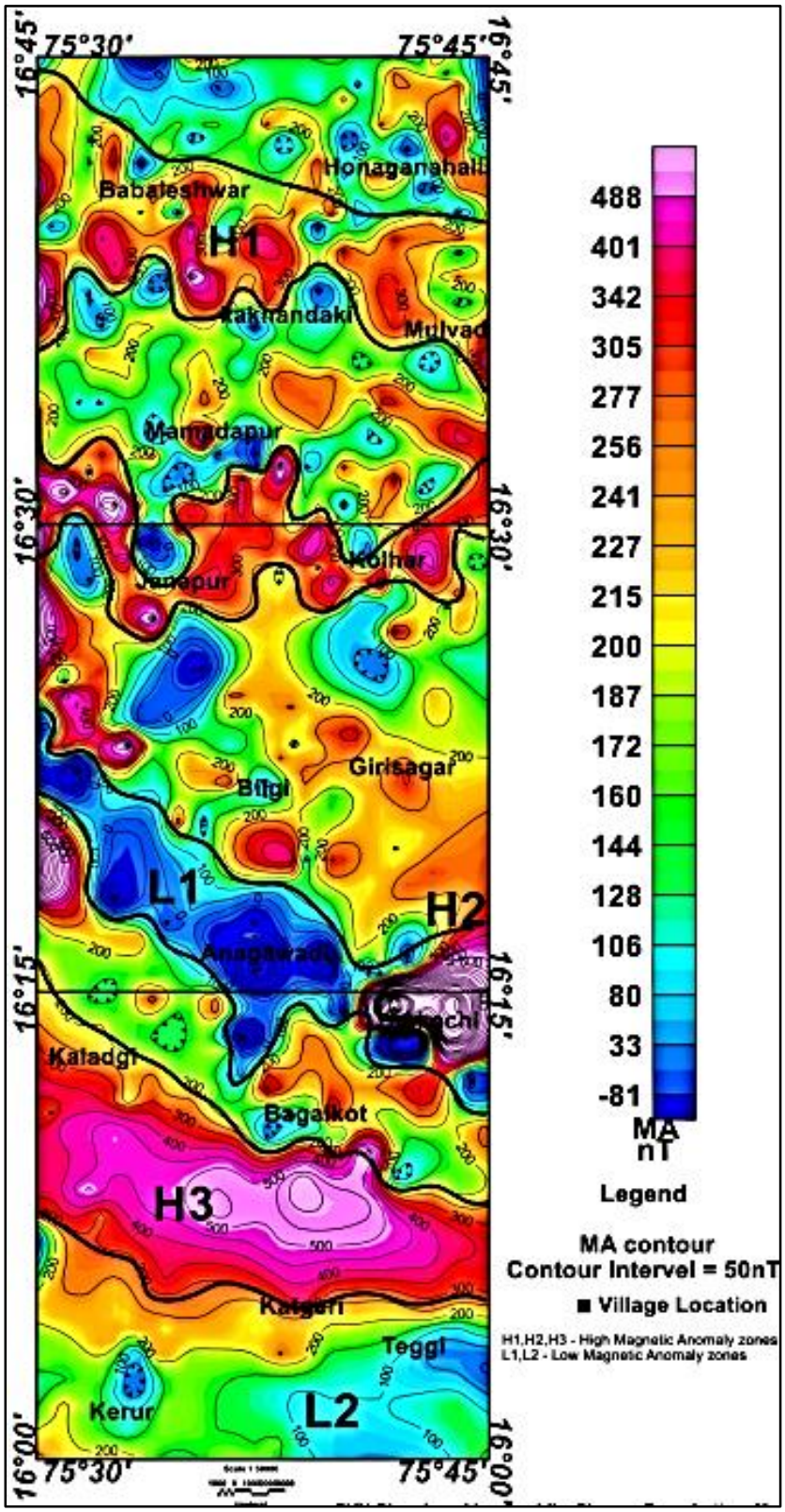

Figure 7. Magnetic (TF) anomaly map in parts of Belgaum, Bijapur, Dharwar and Raichur districts, Karnataka.

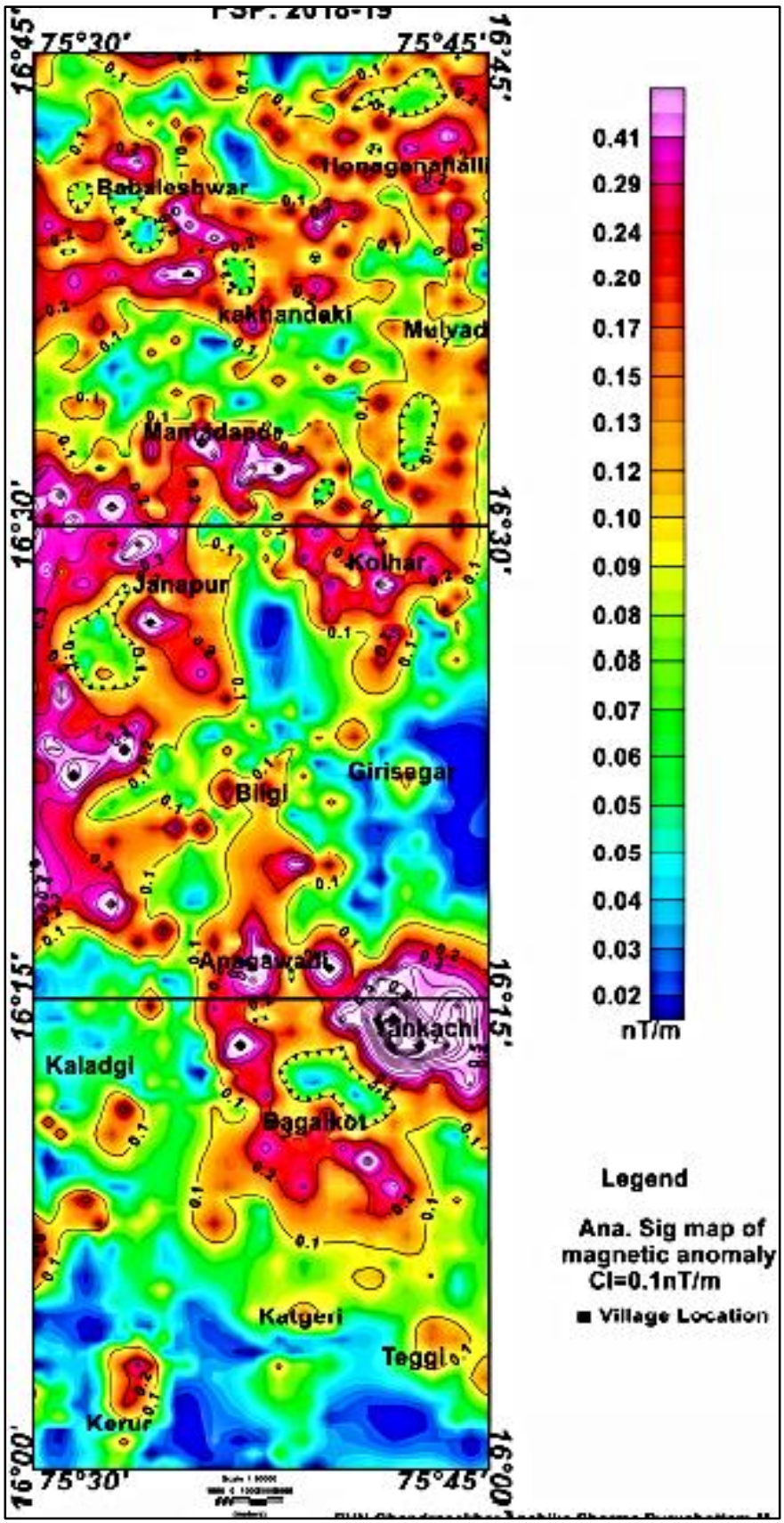

Figure 8. Analytic signal of magnetic anomaly map in parts of Belgaum, Bijapur, Dharwar and Raichur districts, Karnataka.

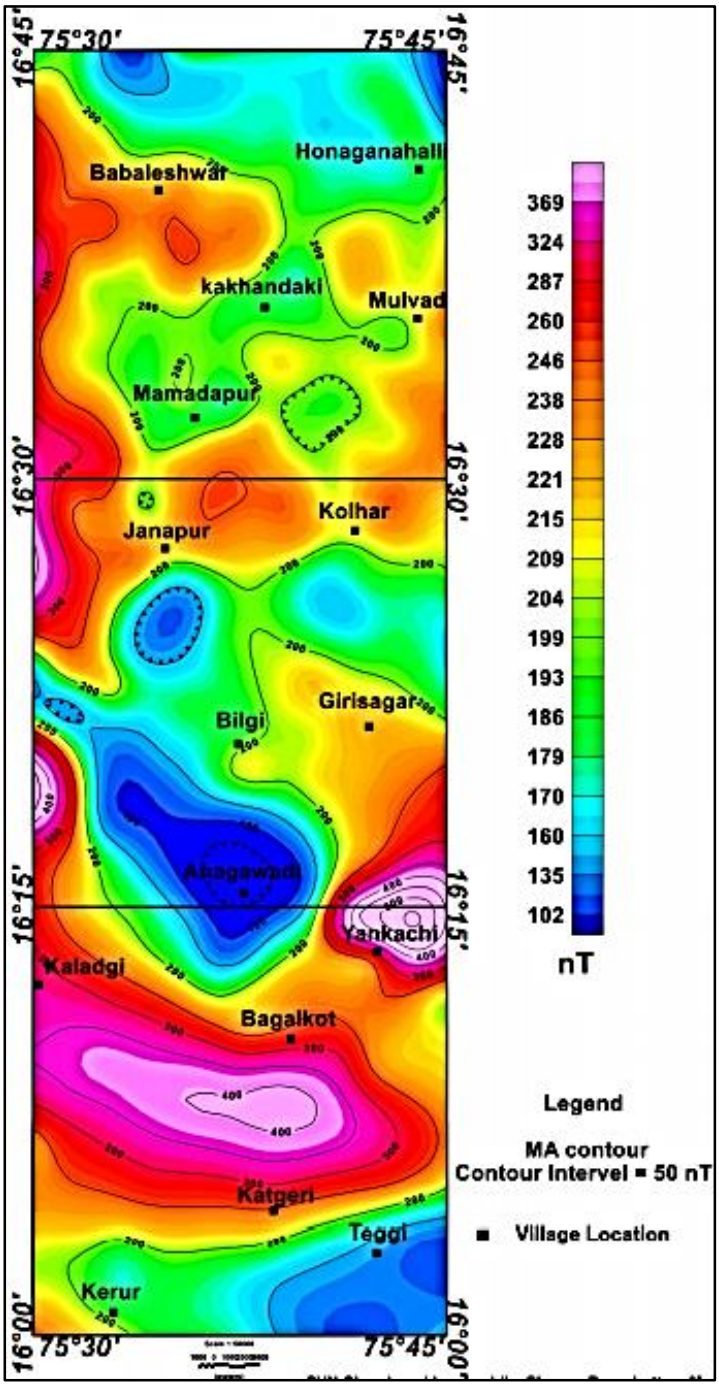

Figure 9. Regional magnetic anomaly map in parts of Belgaum, Bijapur, Dharwar and Raichur districts, Karnataka.

3D Euler deconvolution for depth estimation

The 3D Euler deconvolution of Reid et al. (1990) is a technique applied to the gridded potential field data to determine the position, depth and nature of sources on the basis of gradient of potential field. In present study, the technique has been applied to gravity and magnetic data for depth persistence of causative bodies. Data have been processed with Geosoft Software to find depth solutions by Euler deconvolution technique. Each calculation has been run for different grid cell sizes (500 m, 750 m and 1000 m), Structural Indices (source body geometry for 0, 0.5. and 1) and window lengths (5 km and 10 km) to derive depth solutions for causative bodies.

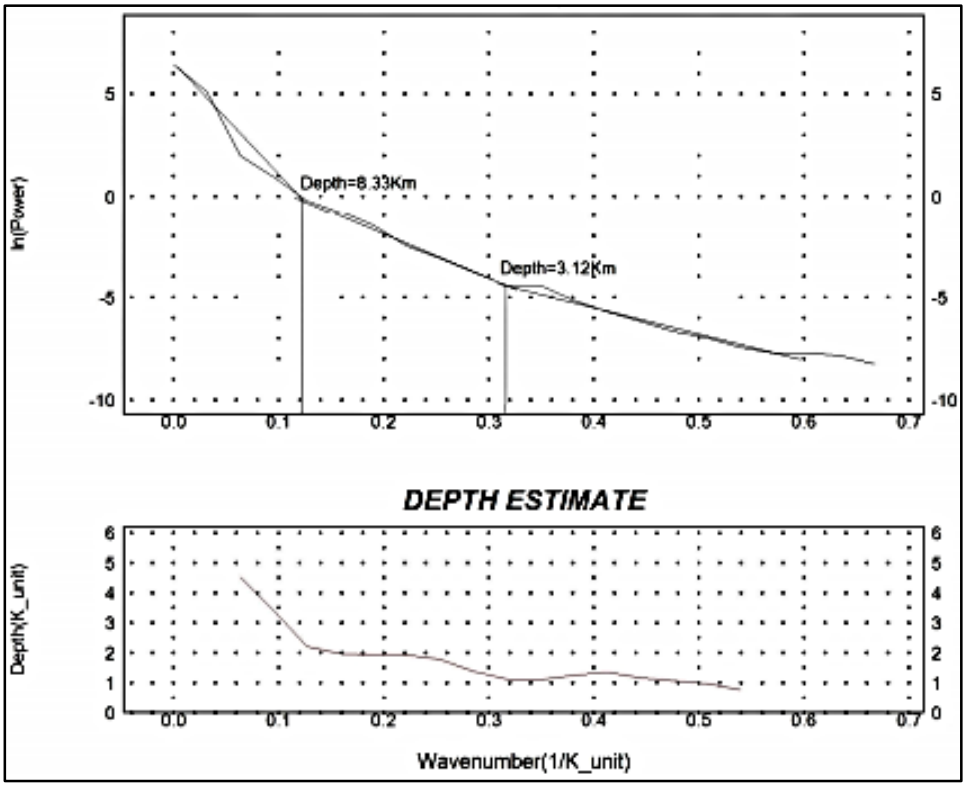

Figure 10. Radially averaged power spectrum of gravity data in parts of Belgaum, Bijapur, Dharwar and Raichur districts, Karnataka.

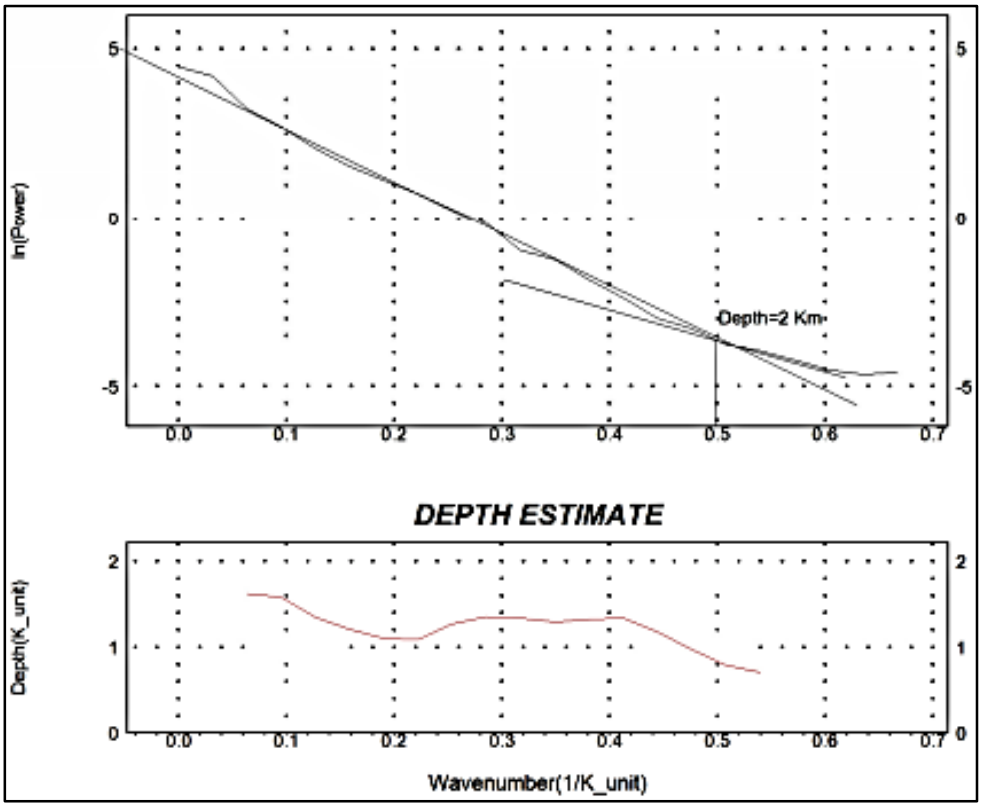

Figure 11. Radially averaged power spectrum of magnetic data in parts of Belgaum, Bijapur, Dharwar and Raichur districts, Karnataka.

Best solutions for Bouguer gravity anomaly have been obtained for grid cell size of 750 m, Structural Index of 1, window size of 10 km x 10 km and depth tolerance of 25%. The solutions have been superimposed on the gravity contour map of the area (Figure 12).

The deeper depth range >3000 m labelled with red solid circle, trending NW-SE direction dominates the northern part over Deccan trap, and southern part over Kaladgi Supergroup of sediments indicating their deeper extension. The remaining central part is dominated by a shallow depth range of 1000-2000 m levelled with blue solid circle and yellow solid circle with depth range of 2000-3000 m. The linear clustering trending in N-S direction are seen towards northern and west central parts, trending NE-SW direction towards central part whereas, curvilinear in the central and southern parts respectively. These linear and curvilinear clustering of depth solutions may be inferred as due to geologic/faulted contacts.

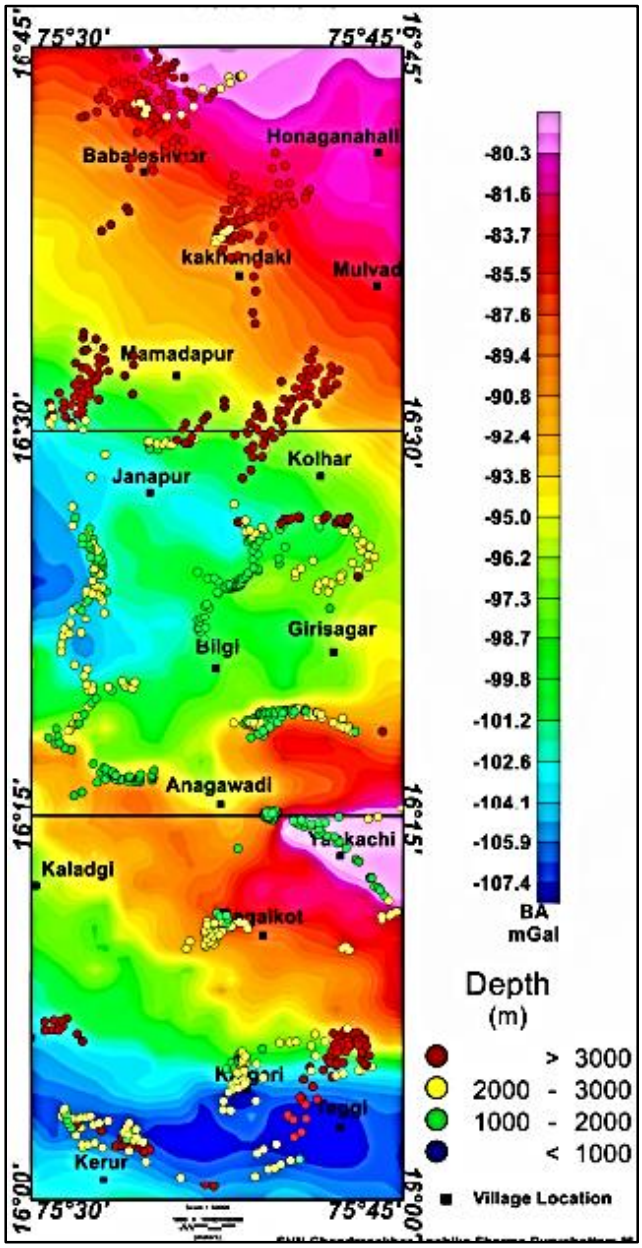

Figure 12. Euler depth solution of gravity data in parts of Belgaum, Bijapur, Dharwar and Raichur districts, Karnataka.

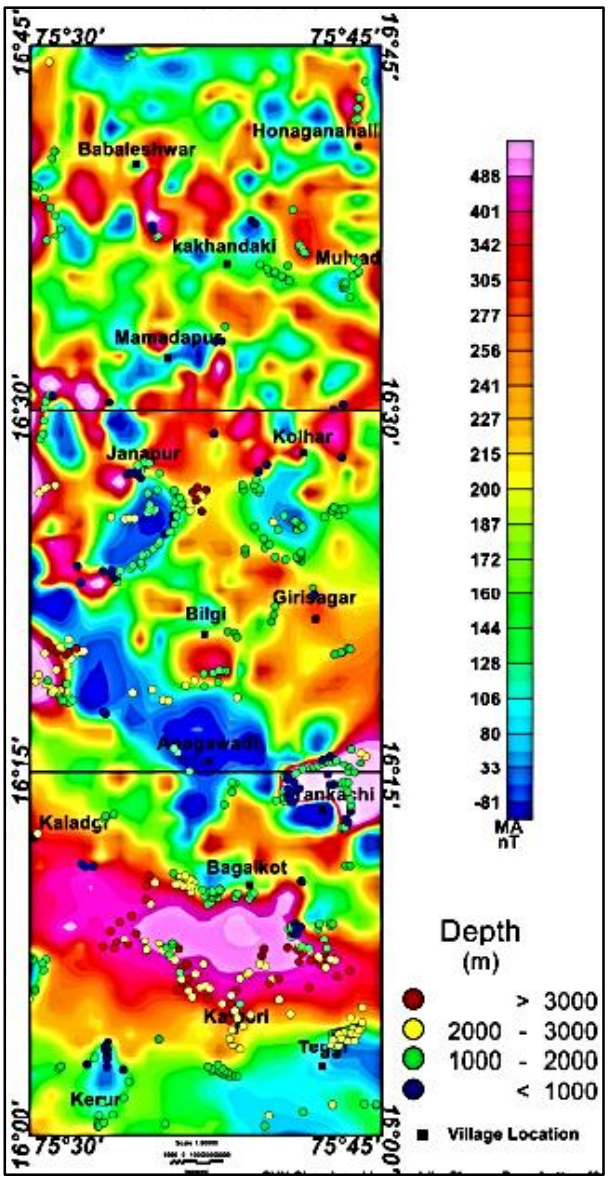

Figure 13. Euler depth solution of magnetic data in parts of Belgaum, Bijapur, Dharwar and Raichur districts, Karnataka.

Depth solutions derived from magnetic anomaly for grid cell size 750 m, Structural Index 1, Window size 5 km x 5 km and depth tolerance 20% have been plotted in magnetic analytic signal map (Figure 13). The depth range 1000-2000 m levelled with blue solid circle, mostly dominates the central part over Kaladgi Supergroup of sediments and Closepet granite. The remaining southern part is dominated by the depth range of 1000-2000 m, 2000-3000 m and >3000 m over sediments of Kaladgi Supergroup indicating its extension from shallow subsurface to deeper one. The linear clustering in the northern part whereas curvilinear clustering in the central and southern parts are observed. Prominent contacts are observed over Hungund schist belt around Yankachi in the eastern part and south of Bagalkot in the southern part over sediments respectively.

CONCLUSIONS

(i) The NW-SE trending northern and east central gravity highs are well reflected as high residual anomaly in residual and first order vertical derivative of Bouguer anomaly map.

(ii) High gravity anomaly closure near Yankachi is prominently reflected as residual gravity high. This residual high correspond to the Hungund schist belt in the eastern part.

(iii) The high magnetic anomaly peaks in the northern part trending NW-SE direction in Mulvad-Kakhandaki-Babaleshwar section may be due to the contribution of BIF within Deccan trap covered area and southern high anomaly peaks trending NW-SE direction in Teggi-Katgeri-Kaladgi

section may be the contribution by the basement granite gneisses composed of biotite gneiss and migmatite gneiss and Dharwar Supergroup of rocks.

(iv) Formational/lithological contact aligned in E-W direction has been delineated between trap and Closepet granite characterized by bipolar nature of anomalies in Janapur-Kolhar section in the central part.

(v) A NW-SE trending low magnetic anomaly tract (L1) northeast and southwest of Anagawadi, may be indicative of magnetic shear zone and is well reflected as high analytic signal of magnetic anomaly where enrichment of magnetic minerals are postulated.

(vi) Range of basement depth through radially averaged power spectrum of gravity and magnetic data has been brought out in western Dharwar Craton.

(vii) The linear clustering, trending in N-S direction (depth range 1000-3000 m) of Euler depth solutions, are seen towards west central, NW-SE direction (depth range >3000 m) in the northern part and NE-SW in the central part (depth range 1000-3000 m), whereas curvilinear cluster towards central and southern parts. These linear and curvilinear clustering of depth solutions may be inferred as geologic/faulted contacts.

ACKNOWLEDGEMENTS

The authors are thankful to the Director General of GSI for permission to publish the paper. The authors are thankful to the learned reviewers for valuable suggestions and comments, which greatly helped to improve the manuscript. Thanks are due to the Chief Editor for editing the manuscript thoroughly with patience apart from his busy schedule. The authors also thank Chief Editor for his kind support and encouragement.

Compliance with Ethical Standards

The authors declare that they have no conflict of interest and adhere to copyright norms.

REFERENCES

Balakrishnan, S., Rajamani, V. and Hanson, G.N., 1999. U-Pb ages for zircon and titanite from the Ramagiri area, southern India: evidence for accretionary origin of the eastern Dharwar craton during the late Archean. J. Geology, 107, 69-86.

Blakeley, R.J., 1995. Potential theory in Gravity and Magnetic Applications, Cambridge University Press, New York.

Boger, S.D., Carson, C.J., Fanning, C.M., Hergt, J.M., Wilson, C.J.L. and Woodhead, J.D., 2002. Pan-African intraplate deformation in the northern Prince Charles Mountains, east Antarctica. Earth planet. Sci. Lett., 195, 195-210

Dey, S., Pandey, U.K., Rai, A.K. and Chaki, A., 2012. Geochemical and Nd isotope constraints on petrogenesis of granitoids from NW part of the eastern Dharwar craton: possible implications for late Archaean crustal accretion. J. Asian Earth Sci., 45, 40-56.

Drury, S.A. and Holt, R.W., 1980. The tectonic framework of the south Indian craton: a reconnaissance involving LANDSAT imagery. Tectonophysics, 65, 71-75.

Geosoft, 2015. Oasis Montaj data processing and analytical system for earth science applications, 8.5. Geosoft Inc., Toronto, Canada.

Gokarn, S.G., Gupta, G. and Rao, C.K., 2004. Geoelectric structure of the Dharwar Craton from magnetotelluric studies: Archean suture identified along the Chitradurga–Gadag schist belt. Geophys. J. Int., 158, 712-728.

Grant, F.S. and West, G.F., 1965. Interpretation theory in Applied Geophysics. McGraw-Hill, New York, 306-381.

GSI, 2017. Report on Geophysical Mapping in Toposheet nos. 57 A/1,2,3,6&11 in parts of Karnataka & AP, FSP:2016-17. GSI Unpubl. Rep.

GSI, 2018. Report on regional gravity and magnetic (TF) surveys in toposheet no. 47P/10, 11 and 12 in parts of Belgaum, Bijapur, Dharwar and Raichur districts, Karnataka. GSI Unpub. Rep. FSP: 2018-2019, item code: M1AGS-GPM/NC/SR/2018/17236.

Gupta, M.L., Sundar, A. and Sharma, S.R., 1991. Heat flow and heat generation in the Archean Dharwar cratons and its implications for the Southern Indian Shield geotherm and lithospheric thickness. Tectonophysics, 194, 107-122.

Gupta, S., Rai, S.S., Prakasam, K.S., Srinagesh, D., Bansak, B.K., Chadha, R.K., Pristley, K. and Gaur, V.K., 2003. The nature of the crust in southern India: implications for Precambrian evolution. Geophys. Res. Lett., 30, 1.1–1.4.

Harikumar, P., Rajaram, M., and Balakrishnan, T.S., 2000. Aeromagnetic study of peninsular India. Proc. Indian Acad. Sci. (Earth Planet. Sci.), 109, 381- 391.

Jayaprakash, A.V., Sundaram, V., Hans, S.K. and Mishra, R.N., 1987. Geology of the Kaladgi-Badami basin, Karnataka. Mem. Geol. Soc. India, 6, 201-226.

International Association of Geodesy (IAG), 1980. The Geodesist's Hand Book (Ed. I.I. Mueller), Bull. Geod. 54(3). 226pp.

Kaila, K.L., Roy Chowdhury, K., Reddy, P.R., Krishna, V.K., Narain, H., Subbotin, S.I., Sologub, V.B., Checkunov, A.V., Kharechko, G.E., Lazarenko, M.A. and Ilchenko, T.V., 1979. Crustal structure along Kavali-Udipi profile in the Indian Peninsular shield from deep seismic sounding. J. Geol. Soc. India, 20, 307-333.

Kumar, A., Pande, K., Venkatesan, T.R. and Bhaskar Rao, Y.J., 2001. The Karnataka late Cretaceous dykes as products of the Marion hotspot at the Madagascar–India breakup event; evidence from 40Ar-39Ar geochronology and geochemistry. Geophys. Res. Lett., 28, 2715-2718

Manikyamba, C., Naqvi, S.M., Mohan, M.R. and Rao, T.G., 2004. Gold mineralisation and alteration of Penakacherla schist belt, India, constraints on Archaean subduction and fluid processes. Ore Geology Rev., 24, 199-227.

Manikyamba, C. and Robert Kerrich, 2012. Eastern Dharwar Craton, India: Continental lithosphere growth by accretion of diverse plume and arc terranes. Geoscience Frontiers, 3(3), 225-240.

Matin, A., 2006. Structural anatomy of the Kushtagi schist belt, Dharwar craton, south India—An example of Archaean transpression. Precamb. Res., 147(1), 28-40.

Maus, S. and Dimri, V., 1996. Depth estimation from scaling power spectrum of potential fields. Geophys. J. Int., 124, 113-120.

Nabighian, M.N., Grauch, V.J.S., Hansen, R.O., LaFehr, T.R., Li, Y., Peirce, J.W., Phillips J. D. and Ruder M.E., 2005. The historical development of the magnetic method in exploration, Geophysics, 70(6), 33–61.

Naidu, P.S. and Mathew, M.P., 1988. Computer program for radial and angular spectrum Estimation. Unpublished Report, GSI, AMSE, Bangalore, 1-11.

Naqvi, S.M. and Rogers, J.J.W., 1987. Precambrian Geology of India. Oxford monographs on Geology and Geophysics, 6, Oxford University Press, 223p.

Naqvi, S., Khan, R., Manikyamba, C., Mohan, M. and Khanna, T., 2006. Geochemistry of the Neo-Archaean high-Mg basalts, boninites and adakites from the Kushtagi-Hungund greenstone belt ofthe Eastern Dharwar Craton (EDC); implications for the tectonic setting. J. Asian Earth Sci., 27, 25-44.

Panduranga, R., 1981. Systematic geological mapping in parts of Bijapur and Basavana Bagevadi Taluks, Bijapur district, Karnataka. GSI Unpubl. Rep. Toposheet No. 47 P/10 and P/14, FSP 1980-81.

Paterson. N.R. and Reeves, C.V., 1985. Applications of gravity and magnetic surveys: the state- of-the- art in 1985, Geophysics, 50(12), 2558-2594.

Qureshy, M.M., Brahmam, N.K., Verma, R.K., Bhalla, M.S., Garde, S.C., Divakar Rao, V. and Naqvi, S.M., 1967. Geological, geochemical and geophysical studies along 14th parallel in Mysore, Proc. Symp. Upper Mantle Project, Hyderabad, India, 4–8 January 1967, 211-225.Geophysical Research Board & National Geophysical Research Institute, Hyderabad, India.

Raju, D.D., 2010. Specialized thematic mapping of the Simikere subgroup of Kaladgi Group sediments in parts of Bagalkot district, Karnataka. GSI Unpub. Rep. FSP 2005-2006, Code: STM/SR/KG/2004/021, Toposheet No. 47 P/12 and 47 P/8.

Raval, U. and Veeraswamy, K., 2000. Radial and linear modes of interaction between mantle plume and continental lithosphere: a case study from western India. J. Geol. Soc. India, 56, 525-536.

Reid, A.B., Allsop, J.M., Granser, H., Millet, A.J. and Somerton, I.W., 1990. Magnetic interpretation in three dimensions using Euler deconvolution. Geophysics, 55, 80-91.

Roy, S. and Rao, R.U.M., 2000. Heat flow in the Indian shield. J. Geophys. Res., 105(B11), 25587-25604.

Sharma, P.V., 1986. Geophysical Methods in Geology: Elsevier Science Publishing Co., Inc.

Spector, A. and Grant, F.S., 1970 Statistical model for interpretating aeromagnetic data. Geophysics, 35, 293-302.

Srinagesh, D. and Rai, S.S., 1996. Teleseismic tomographic evidence for contrasting crust and upper mantles in south Indian Archean terrains. Phys. Earth. Planet. Int.., 97, 27-41.

Subrahmanyam, C. and Verma, R.K., 1982. Gravity interpretation of Dharwar greenstone-gneiss-granite terrain in the south Indian shield, its geological implications. Tectonophysics, 84, 225-245.

Swaminath, J., Ramakrishnan, M. and Vishwanatha, M.N., 1976. Dharwar stratigraphic model and Karnataka Craton evolution. Records of the Geological Survey of India, 107, 149-175.

Swaminath, J. and Ramakrishnan,M., 1981. Early PrecambrianSupracrustals of Southern Karnataka. Geological Survey of India Memoir, 363p.

Received on: 29.09.2021; Revised on: 10.12.2021; Accepted on: 31.12.2021

J. Ind. Geophys. Union, 26(1) (2022), 41-46

Crustal deformation rates in the Indian region from continuous GNSS measurements from 2013 to 2018 and sensitivity of plate velocity with reference frames

Sravanthi Gunti[1*], J. Narendran[1], Priyom Roy[1], S. Muralikrishnan[1], K. Vinod Kumar[1], M. Subrahmanyam[2] and Y. Israel[2]

[1]National Remote Sensing Centre, Indian Space Research Organization (ISRO), Balanagar, Hyderabad-500037, India

[2]Department of Geophysics, Andhra University, Visakhapatnam-530017, India

*Corresponding Author: sravsgeophysics@gmail.com

ABSTRACT

The Indian plate velocity for six IGS (International GNSS Service) stations was re-estimated by processing the GNSS datasets for the period January, 2013 to December, 2018 in International Terrestrial Reference Frame 2008 (ITRF2008) using long baseline GNSS scientific software Bernese 5.2. Out of these six IGS stations, two stations IISC in Bengaluru and HYDE in Hyderabad are located on the Deccan plateau, two stations LCK3 and LCK4 in Lucknow are located in the Indo-Gangetic plain and the remaining two stations, PBRI and PBR2 are located in the Port Blair area of Andaman Islands. Totally, 13 IGS sites data have been used as reference stations; 6 sites being located in the Indian plate and the remaining 7 sites in the adjacent plates (Eurasian plate, Arabian plate, and Australian plate). The result indicates that Indian plate is moving with a velocity of 54±0.6 mm/year at Hyderabad, 55±0.8 mm/year at Bengaluru, 48.5±0.95 mm/year at Lucknow and 21.5±1.2 mm/year at Port Blair. The results confirm that Southern part of India is moving as a rigid plate at velocity of 48 to 55 mm/year and the Andaman area, at a velocity of 21 to 22 mm/year in North East direction. The sensitivity of the velocity estimates with reference to the different Terrestrial Reference Frames namely ITRF2005, ITRF2014 has also been analysed.

Keywords: Bernese software, ITRF (International Terrestrial Reference Frame), Indian plate velocity, earthquakes, IGS

INTRODUCTION

The change in the earth's surface caused by tectonic forces is called crustal deformation. The crustal deformation rates are very useful in understanding the earthquake phenomenon. The precise plate velocity is a key parameter in estimating the crustal deformation rates. Different techniques like Satellite Laser Ranging (SLR), Global Navigation Satellite System (GNSS), Very Long Baseline Interferometry (VLBI), Doppler Orbitography and Radio Positioning Integrated by Satellite (DORIS) etc. are there for estimating the plate velocity. Particularly, the geodetic methods like GNSS technology are very effective tool in studying the crustal deformation. Previously several research groups have studied the crustal deformation using GNSS technology. DeMets et al., (1990) observed that Indian plate moves with a velocity of approximately 5 cm/year. EC et al., (2000) used GPS data for studying the crustal deformation and observed that the motion of Indian Plate at Hyderabad (37 mm/year) is smaller than the NUVEL-1A model (45 mm/year). Southern peninsular India moves as a rigid plate with the velocity of Indian plate (Jade, 2004; Mahesh et al., 2012; Krishna et al., 2014; Rajewar et al., 2021). In the Indian Plate interior, there is no segmentation and observed residual velocity is 1 to 3 mm/yr (Jade et al., 2017; Sharma et al., 2021). The angular velocity for Indian plate was 0.5205±0.002°/myr. (Rajewar et al., 2021). The advancement in GPS geodesy makes it possible to understand the crustal deformation of Indian plate with better accuracy (EC et al., 2000; Jade, 2004). According to the Indian seismic zone map (BIS, 2002), seismically, there is no safe zone within India. Hence, it is required to monitor the crustal deformation of Indian region continuously to understand the earthquake process. In this paper, we have studied the crustal deformation of Indian region by using 6 IGS stations lying within the Indian region and 7 IGS stations lying in different tectonic plates around the Indian region as reference stations. In addition to that, we have analysed the effect of reference frames on plate velocity.

DATA

Continuous GNSS data from 13 IGS sites (International GNSS Services, Source: ftp://cddis.gsfc.nasa.gov) for the period of five years (Jan 2013 to Dec 2018) were used in this study. IGS is an international consortium involving more than 200 participating organizations in over 80 countries (Dow et al., 2009). The IGS sites were installed with geodetic receivers and calibrated antennae for high precision geodynamic studies. Among 13 IGS sites (Table 1), 6 sites are in the Indian region and the remaining 7 sites are located adjacent to the Indian region.

6 Indian region sites are Hyderabad (HYDE-Indian Plate), Bengaluru (IISC-Indian Plate), Lucknow (LCK3 and LCK4-Indian Plate), Port Blair (PBR2 and PBRI-Indian Plate) and the remaining 7 sites are Cocos (COCO-Australian Plate), Diego Garcia (DGAR-Australian Plate), Kitab (KIT3-Arabian Plate), Lhasa (LHAZ-Eurasian Plate), Quezon city (PIMO-Eurasian Plate), Bishkek (POL2-Eurasian Plate) and Yibal (YIBL-Arabian Plate), which are located adjacent to the Indian Plate. The daily based GNSS data in RINEX (Receiver INdependent EXchange) format for all the stations with sampling interval of 30 seconds were used in this study. The data used in this study have completeness above 90% and the multipath/cycle slips are within the acceptable range.

Table 1. Station information of different sites used for the present study and data availability of corresponding stations during the study period

Station name	Station ID	Plate	Type of site	Data period	
				From	To
Cocos	COCO	Australian	Reference	Jan-13	Dec-18
Diego Garcia	DGAR	Australian	Reference	Jan-13	Dec-18
Hyderabad	HYDE	Indian	Target	Jan-13	Dec-18
Bengaluru	IISC	Indian	Target	Jan-13	Dec-18
Kitab	KIT3	Arabian	Reference	Jan-13	Nov-17
Lucknow	LCK3	Indian	Target	Sep-14	Dec-18
Lucknow	LCK4	Indian	Target	Sep-14	Dec-18
Lhasa	LHAZ	Eurasian	Reference	Jan-13	Dec-18
Port Blair	PBRI	Indian	Target	Jan-13	Dec-18
Port Blair	PBR2	Indian	Target	Jan-13	Feb-16
Quezon city	PIMO	Eurasian	Reference	Jan-13	Dec-18
Bishkek	POL2	Eurasian	Reference	Jan-13	Aug-18
Yibal	YIBL	Arabian	Reference	Jan-13	Mar-18

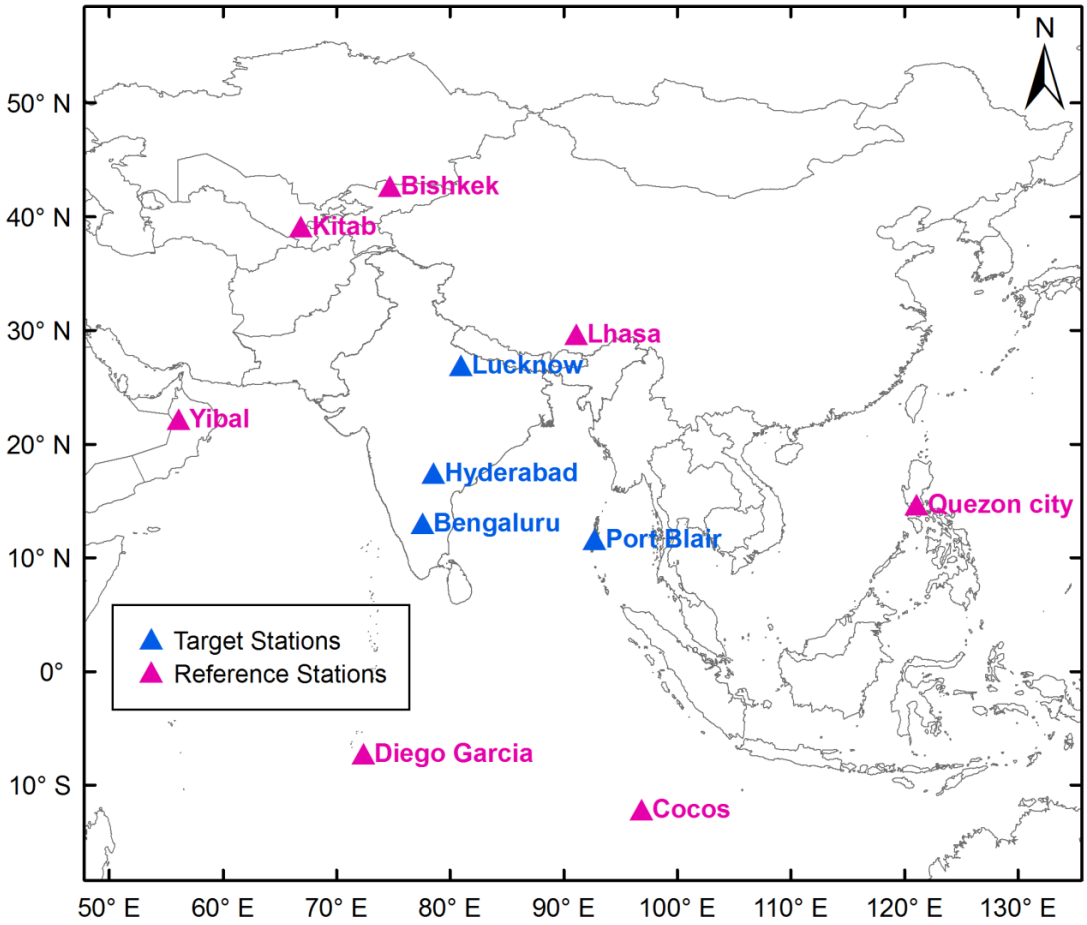

Figure 1. Network map used for processing the GNSS data. The blue triangles indicate the target sites on the Indian plate and pink triangles indicate the IGS reference sites.

METHODS

The GNSS data have been quality checked using Leica Spider QC and TEQC software (Esteyand Wier, 2013). A network containing six Indian region target sites and reference sites which are lying in adjacent plates of India has been defined to form baselines (Figure 1). The GNSS data were processed using Bernese 5.2 long baseline scientific post processing software for coordinate and velocity estimation. The Bernese software was developed at the Astronomical Institute of the University of Bern (AIUB), Switzerland (Dach and Walser, 2013).

The elementary inputs in the processing using Bernese software are observation files, precise ephemeris, Earth orientation parameters, clock files, ionospheric maps, Differential Code Biases (Source: ftp://ftp.aiub.unibe.ch), mapping functions, oceanic loading co-efficients (Source: http://holt.oso.chalmer.se) and atmospheric loading coefficients (Ray and Ponte, 2003) from different organization/ sources around the world to get the mm level accuracy. Also, the multiple general files like latest Satellite health information, leap seconds, receiver, antenna files, antenna phase centre offsets etc., are required for precise and accurate positioning. The daily based RINEX observation data were decimated to 30 seconds interval to maintain the consistency of sampling interval for each station. "RNX2SNX" program was adopted for carrier phase based double difference positioning. In this program, generation of tabular orbits, Single Point Positioning and Synchronization of receiver clocks, cycle slip detection and repair, baseline computation, carrier phase ambiguity resolution, atmospheric and oceanic loading correction, datum fixing and estimation of the coordinates are few important steps. It also verifies the consistency of the coordinates derived in terms of datum definition and comparison of coordinates. The flow chart shown in Figure 2 depicts the processing methodology adopted in Bernese 5.2 software.

The final solution has the coordinates (geocentric coordinates) in ITRF 2008 reference frame. Further, these coordinates are projected to UTM (Easting, Northing and Height). Easting and northing components were used for computation of horizontal velocity. The height component was excluded due to its seasonal variation (Bettinelli et al., 2008). From the UTM coordinates the horizontal velocity was computed for 06 IGS stations in Indian region. Further the study also addresses the effect of reference frames namely ITRF2005 and ITRF2014 on horizontal plate velocity.

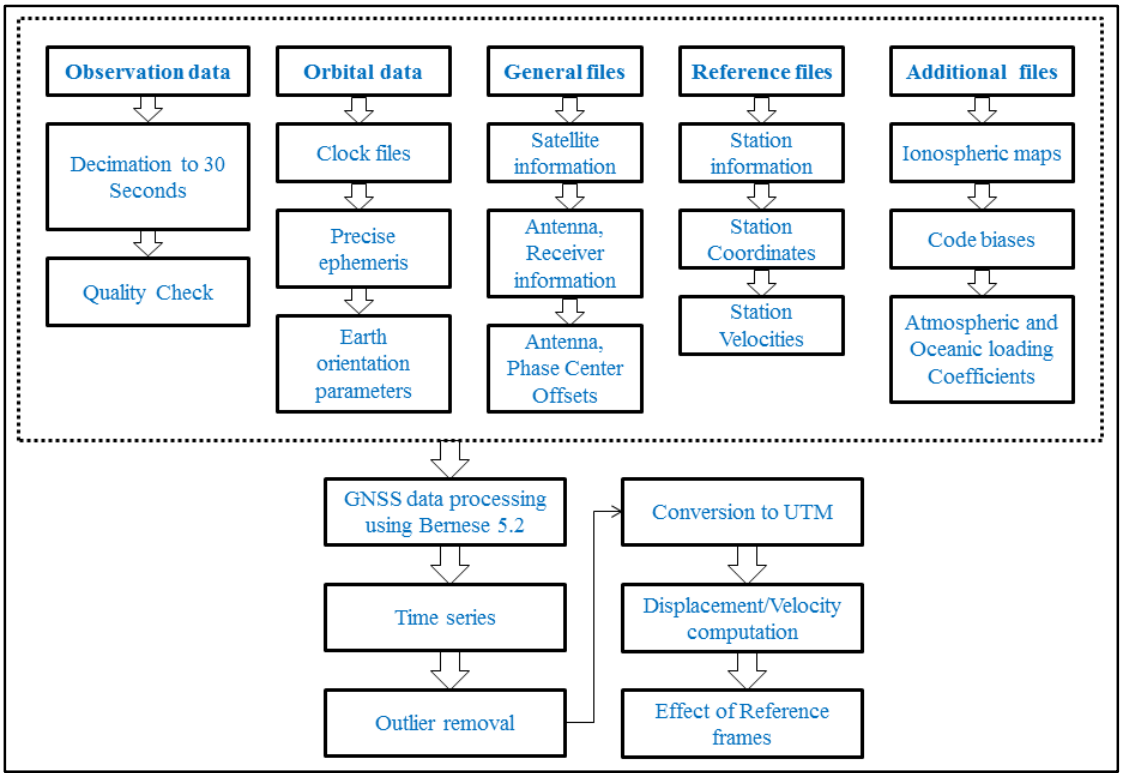

Figure 2. Process flow for processing GNSS data using Bernese 5.2

RESULTS

The Indian plate velocity at 6 IGS stations (HYDE, IISC, LCK3, LCK4, PBR2 and PBRI) has been computed using available GNSS stations (Table 1) for the period of 5 years from 01-Jan-2013 to 31-Dec-2018. The continuous GNSS data were processed using Bernese 5.2 long baseline software. Estimated the coordinates and velocities of 6 stations in ITRF 2008 reference frame by combining the daily based solutions. The daily based continuous time series in terms of change in easting (ΔE) and change in northing (ΔN) for 06 IGS stations have been shown in Figure 3. The horizontal plate velocity for each station has been computed using easting and northing components. The results (Table 2) indicate that all 06 stations are moving in north east direction.

The Indian plate is moving with a velocity of 54±0.6 mm/year at Hyderabad station, 55±0.8 mm/year at Bengaluru station, 48±0.9 mm/year at Lucknow (LCK3) and 49±1 mm/year at Lucknow (LCK4). The Indian plate is moving with a velocity of 21±1.1 mm/year and 22±1.3 mm/year at Port Blair (PBRI). Figure 4 shows the velocity vectors with error ellipses for the GNSS stations lying in Indian region. The magnitude of arrow marks is proportional to the magnitude of the velocity vectors.

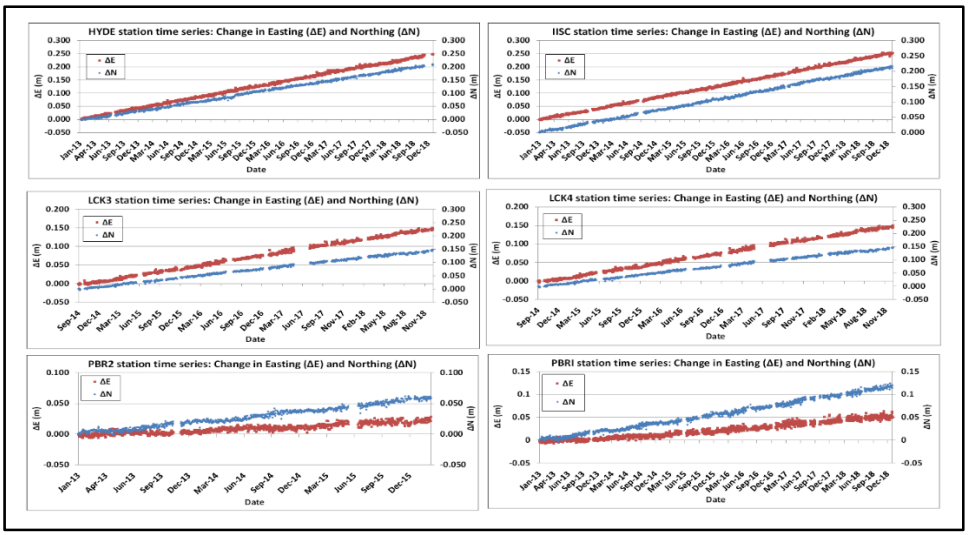

Figure 3. Time series in terms of easting and northing for the stations HYDE, IISC, LCK3, LCK4, PBR2 and PBRI respectively

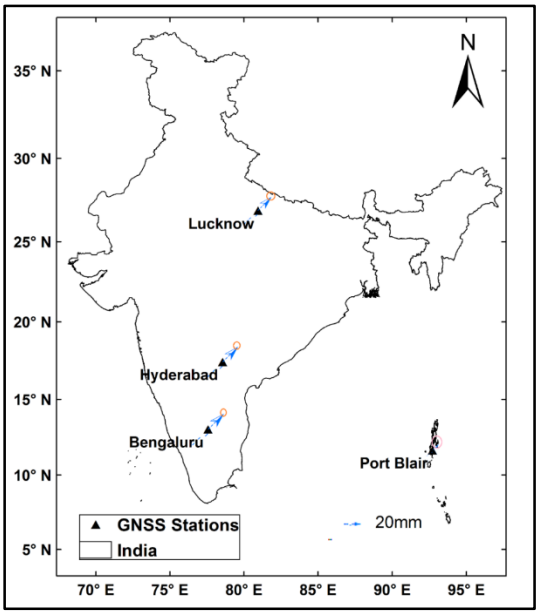

Figure 4. Indian Plate velocity with error ellipses (red) for the study area.

Table 2. Plate velocities at 6 IGS stations in ITRF 2008, ITRF 2005 and ITRF 2014 reference frame

Station Name	Velocity (mm/year)		
	ITRF 2008	ITRF 2005	ITRF 2014
HYDE	54	52	54
IISC	55	54	55
LCK3	48	46	50
LCK4	49	47	50
PBR2	21	25	22
PBRI	22	21	22

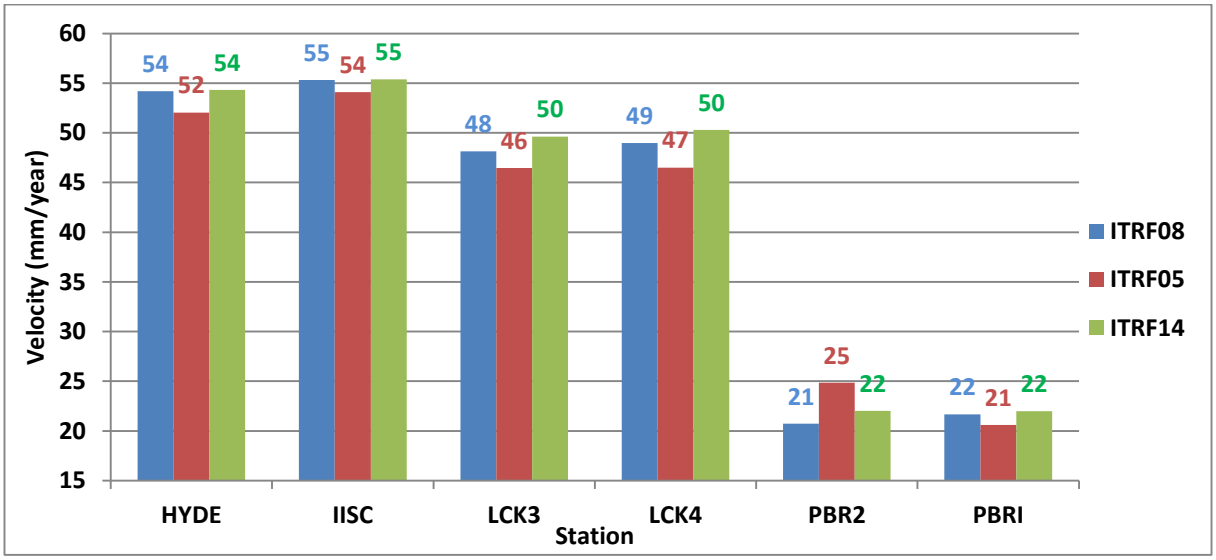

Figure 5. Plate velocity of 6 IGS stations in different ITRF reference frames (ITRF 2005, ITRF 2008 and ITRF 2014)

DISCUSSION

From the Figure 3, it was observed that there is a constant variation in easting and northing during the study period. For the stations, HYDE, IISC, LCK3 and LCK4, there is no significant change in plate velocity compared with previous results (Bettinelli et al., 2006; Krishna et al., 2014; Jade et al., 2017; Sharma et al., 2021). This shows that the plate velocity is consistent during the study period and the seismic activity in and around these four IGS stations (HYDE, IISC, LCK3 and LCK4) has not altered plate velocity. Whereas, the plate velocity at Port Blair (PBR2 and PBRI stations), was differed by 5.5 mm/year with the observations of Jade et al., (2017). This could be due to the difference in the observation period. Also, we have compared the plate velocity in ITRF 2005 and 2014 reference frame with the plate velocity in ITRF 2008 reference frame and corresponding results are tabulated in Table 2. The difference between plate velocity in ITRF 2008 and ITRF 2005 reference frame was ±4 mm/year, and in between ITRF 2008 and 2014 was ±2mm/year (Figure 5).

The improvement in the plate velocity from ITRF 2005 to ITRF 2014 could be due to the constant updation by the International Earth Rotation and Reference Systems Service (IERS).

CONCLUSIONS

From the re-estimated Indian plate velocities, it was observed that Indian plate is moving with a velocity of 54±0.6 mm/year at Hyderabad, 55±0.8 mm/year at Bengaluru and 48.5±0.95 mm/year at Lucknow. This confirms that south to central part of India is moving as a rigid plate at velocity of 48 to 55 mm/year in north east direction. The Indian plate is moving with a velocity of 21.5±1.2 mm/year at Port Blair (PBRI). This indicates that the Andaman Islands velocities may be slowed down after the M_w 9.3 Sumatra 2004 earthquake. The analysis of sensitivity of different ITRFs suggests that the variation of plate velocity is within ±5mm/year. Hence a continuous measurement of GNSS data or other geodetic techniques are required to study the geodynamics of the Indian plate. In this

study, we have established a methodology for computing plate velocity and it was observed that the CORS (Continuous Operating Reference Sites) data may be helpful in understanding the geodynamics for which already established GNSS receivers can be used. The plate velocity is critical in strain accumulation study for understanding the earthquakes better. The strain accumulation can be studied using these GNSS plate velocities as the input to understand the earthquakes in better way by using change in baseline lengths and Finite Element Method etc.

ACKNOWLEDGEMENT

The authors are thankful to National Remote Sensing Centre for the inspiration to carry out this work. We thank IGS for providing GNSS data which was obtained through the online archiever of the Crustal Dynamics Data Information System (CDDIS), NASA, Goddard Space Flight Center, Green belt, MD, USA.(ftp://cddis.gsfc.nasa.gov). The authors are very thankful to the Chief Editor, JIGU for valuable suggestions.

Compliance with Ethical Standards

The authors declare that they have no conflict of interest and adhere to copyright norms.

REFERENCES

Bettinelli, P., Avouac, J.P., Flouzat, M., Bollinger, L., Ramillien, G., Rajaure, S. and Sapkota, S., 2008. Seasonal variations of seismicity and geodetic strain in the Himalaya induced by surface hydrology.Earth Planet. Sci. Lett., 266, 332-344.

Bettinelli, P., Avouac, J.P., Flouzat, M., Jouanne, F., Bollinger, L., Willis, P. and Chitrakar, G.R., 2006. Plate motion of India and interseismic strain in the Nepal Himalaya from GPS and DORIS measurements, J. Geodesy, 80, 567-589.

BIS, 2002. IS 1893-2002: Indian Standard Recommendations for Earthquake Resistant Design of Structures, Bureau of Indian Standards, New Delhi.

Dach, R. and Walser, P., 2013. Bernese GNSS Software Version 5.2 Course Tutorial.

DeMets, C., Gordon, R.G., Argus, D.F. and Stein, S., 1990. Current plate motions. Geophys.J.Int., 101(2), 425-478.

Dow, J.M., Neilan, R.E. and Rizos, C., 2009. The international GNSS service in a changing landscape of global navigation satellite systems, J. geodesy, 83, 191-198.

EC, M., Campbell, J., Görres, B., Kotthoff, H. and Smaritschnik, S., 2000. Indian plate kinematic studies by GPS-geodesy. Earth, Planets and Space, 52, 741-745.

Estey, L. and Wier, S., 2013. Teqc tutorial: Basics of Teqc Use and Teqc Products. UNAVCO Inc., Colorado, 61 pp

Jade, S., 2004. Estimates of plate velocity and crustal deformation in the Indian subcontinent using GPS geodesy. Current Sci., 86(10) 1443-1448.

Jade, S., Shrungeshwara, T.S., Kumar, K., Choudhury, P., Dumka, R.K., and Bhu, H., 2017. India plate angular velocity and contemporary deformation rates from continuous GPS measurements from 1996 to 2015. Scientific reports, 7, 1-16.

Krishna, S., Mathew, J., Majumdar, R., Roy, P. and Kumar, K.V., 2014. Geodynamics of the Indian Lithospheric Plate relative to the neighbouring Plates as revealed by Space Geodetic Measurements, The International Archives of Photogrammetry, Remote Sensing and Spatial Information Sciences, 40, 53.

Mahesh, P., Catherine, J.K., Gahalaut, V.K., Kundu, B., Ambikapathy, A., Bansal, A. and Kalita, S., 2012. Rigid Indian plate: constraints from GPS measurements, Gondwana Res., 22, 1068-1072.

Rajewar, S.K., Mohana Lakshmi, C., Mohanty, A., Pandey, D.N., Pandey, A., Chaurasia, A., Pandey, A., Rajeswar Rao, V., Naidu, M.S., Kumar, A. and Mondal, S.K., 2021. Constraining Plate Motion and Crustal Deformation from GNSS Measurements: CSIR-NGRI Contribution, J. Geol. Soc. India, 97, 1207-1213.

Ray, R.D. and Ponte, R.M., 2003. Barometric tides from ECMWF operational analyses. Ann. Geophys. 21, 1897-1910.

Sharma, Y., Pasari, S. and Pasari, N., 2021. Indian Plate Motion Revealed by GPS Observations: Preliminary Results, In Mathematical Modeling and Computation of Real-Time Problems, CRC Press, 203-215.

Received on: 29.08.2021; Revised on: 14.12.2021; Accepted on: 04.01.2022

J. Ind. Geophys. Union, 26(1) (2022), 47-54

2D-Electrical resistivity tomography for groundwater exploration in Archean hard rock terrain in villages of Ottapidaram Taluk, Thoothukudi District, Tamil Nadu (India)

T. Jeyavel Raja Kumar*[1], P. Saravanan[1], C. Dushiyanthan[1], B.Thirunelakandan[2] and M. Senthilkumar[3]

[1]Department of Earth Sciences, Annamalai University, Annamalai Nagar – 608002, India
[2]Department of Geology, Jawahar Science College, Neyveli – 607802, India
[3]Department Geology, Presidency College, Chennai-600005, India
*Corresponding Author: tjeyavel@rediffmail.com; jeyavelgeo@gmail.com

ABSTRACT

Assessment of groundwater potential was done using Electrical Resistivity Tomography (ERT) in a part of hard rock terrain in Ottapidaram Taluk, Thoothukudi District of Tamil Nadu. The study area is located between 8º50´ to 9º00´ N and 78º05´to78º15´E. Geologically, the region comprises Archean gneiss, charnockite and quartzite intrusions. The ERT was carried out at four locations, Sinthalakatttai, Sillanatham, Mupplipatti and Saverimangalam. SYSCOL JUNIOR Switch-48 model resistivity meter is used and Wenner-Schlumberger configuration was adopted. Length of the profile is144 m and 48 electrodes were planted in straight line at an interspacing of 3 m. The measured resistivity data was interpreted using RES2DINV software and maximum depth interpreted was 26 m bgl. The interpreted resistivity model represented 4 layered subsurface geoelectrical structures. The overall resistivity varied from < 5 Ohm m to > 350 Ohm m. Low resistivity range was noted in Saverimangalam and high resistivity range in Sillanatham. The low resistivity observed is due to highly weathered or jointed rocks with water saturation, while the high resistivity may be related to poorly weathered rock with lack of water saturation. From the resistivity models, it is inferred that the study locations have fractured layer zones at shallow depth level up to 15m bgl at Sinthalakattai, Sillanatham and Mupplipatti locations, indicating favourable zones for groundwater occurrences. The existing bore well lithology matches with the interpreted resistivity model, indicating reliability of the ERT study for groundwater exploration.

Keywords: Groundwater, 2D Electrical Resistivity, Electrical Resistivity Tomography, Geoelectrical model, Groundwater Exploration

INTRODUCTION

Groundwater is the main resource of water supply for industrial, agricultural and domestic use in many semi-arid regions. In recent decades, requirement and dependency on groundwater is increased due to population, natural calamities, monsoon failure and development of low cost drilling techniques. The increasing dependency on groundwater has led to decline groundwater level and thus developing stress on aquifer due to over exploitation which has directly caused declining groundwater levels and consequently limited groundwater flow into deeper weathered/fractured zones (Rai et al., 2011; Kumar et al., 2011; Maiti et al., 2012). For a country like India, water scarcity will be hitting hard for sustainable development as it is still largely dependent upon rain fed agriculture and availability of fresh water is one of the foremost concern for the future (Mohanti, 2009). Thus, in the rural areas, most of the interventions have based on groundwater resources, accessed mainly through boreholes and hand dug wells. Success rates for drilling prolific wells have been variable, depending on the underlying geology. This situation is generally owed to the historical geology of the terrain and lack of adequate understanding of the hydrogeology. The hydrogeological characteristic of geology is influenced by the fractures and fault zones (Medeiros and Lima, 1990; Wyns et al., 1999; Taylor and Howard, 2000; Suski et al., 2008). Assessment of fractured rock aquifers in many parts of the world is complicated given their strong heterogeneity.

To study the subsurface geological formation and delineate groundwater potential, geophysical methods play a vital role. It is helpful to find out the hidden subsurface hydrogeological physiognomies adequately and accurately without drilling. Of all surface geophysical techniques, the electrical resistivity imaging (ERI) method has been applied most widely to obtain subsurface information due to the wide range of resistivity for different geological materials (Keller and Frischknecht, 1966; Bhattacharya and Patra, 1968; Koefoed 1979). Particularly, the imaging tomography method has been used effectively by a number of researchers for various applications including groundwater investigations (Owen et al., 2005; Sarma and Prasad, 2006; Pawar et al., 2009; Ratnakumari et al., 2012; Mondal et al., 2013; Rai et al., 2015; Gupta et al., 2015; Arsène et al., 2018; Thiagarajan et al., 2018; Mainoo et al., 2019; Archanakumari et al., 2021), saltwater intrusion problems (Satish et al., 2011; Hermans et al., 2012; Vann et al., 2020; Niculescu and Andrei, 2021) besides geothermal explorations (El-Qady et al., 2000; Kumar et al., 2011).

This technique is helpful in delineating top soil, weathered, fractured and bedrock zone for construction of suitable groundwater units, because in hard rock terrain, the weathered and fractured zone constitutes the potential location for groundwater flow. Thus, delineation of aquifers is the pre-requisite for the assessment of regional/local

groundwater potential. With this background, an attempt has been made to explore the capabilities of the resistivity imaging method for the detection of fractures and/or fractured zones to meet the rising demand of water in hard rock environments.

STUDY AREA

The study area in the eastern coast belong to Ottapidaram Taluk of Thoothukudi District. It lies between 8º50´ to 9º00´ N and 78º05´ to 78º15´E. Geologically, the region comprises Archean gneiss, charnockite and quartzite intrusions (Figure 1). The coastal plain, eolian and shallow pediments are the major geomorphologic units. The elevation of the study area is ±15 m above MSL. The water level varied from 4 m to 9 m below the ground level. The normal annual rainfall over the district is about 570 mm to 740 mm. The recorded minimum and maximum temperatures are 27.8^0 C to 35.5^0C. The relative humidity is high between 60 and 75% that prevails throughout the year

METHODOLOGY

2-D Electrical Resistivity Tomography (ERT) is a multi-electrode resistivity imaging system with multi-core cables and many electrode takeouts. They are connected together to form a multi-electrode set-up, where selection of any four (two for current injection and two for potential measurement) electrodes is possible. The number of electrodes differs from system to system. Some systems carry 12, 24, 48 electrodes and, some 72 and 96 electrodes and so on. The electrodes are laid out on the ground surface in a straight line with a constant spacing. A computer-controlled system is then used to automatically select the active electrodes for each measure (Griffith and Barker, 1993). The measured data are effectively interpreted using data processing software based on inversion techniques. The scheme of multi electrodes arrangement for 2D ERT is well known and explained in detail by many researchers (Barker, 1981; Dahlin, 1996; Loke and Barker, 1996; Sarma, 2014), as presented in the Figure 2.

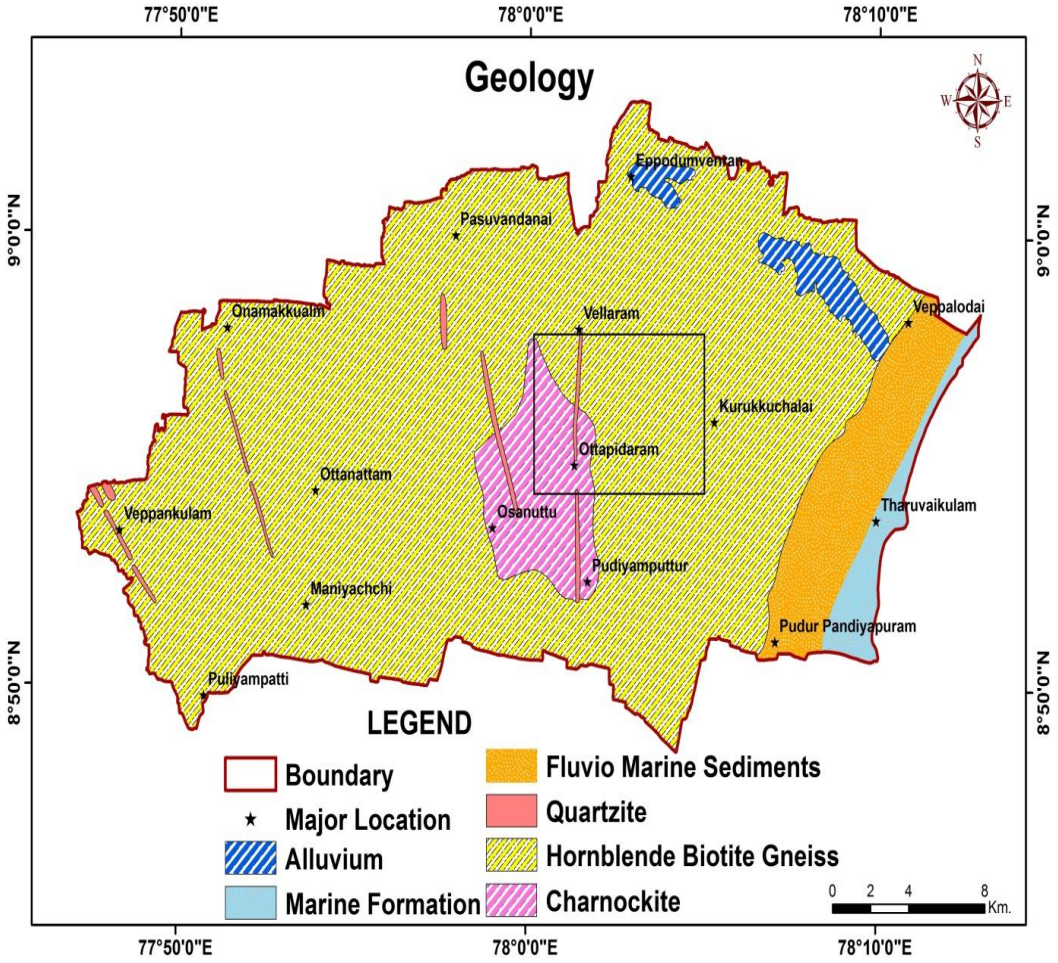

Figure 1. Geology map of the study area. Black rectangle denotes study area

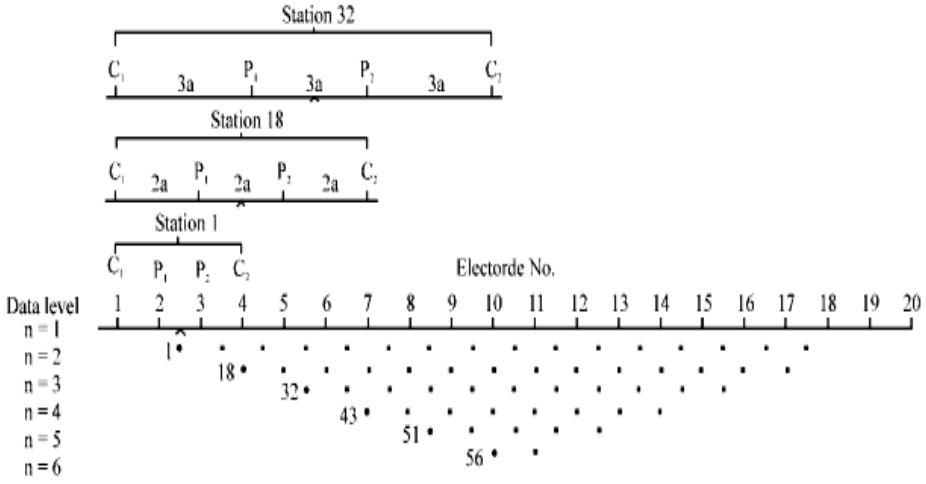

Figure 2. Scheme of electrode arrangement (Loke, 2000)

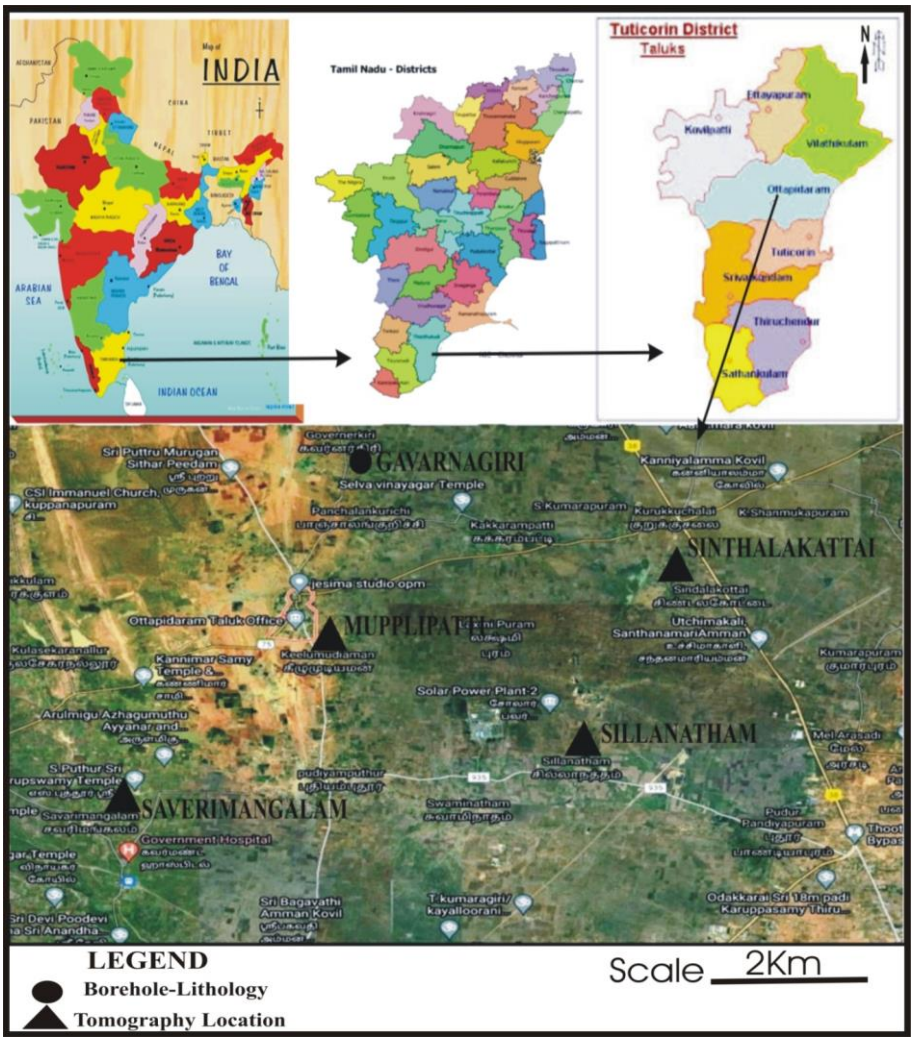

Figure 3. Location map of the study area with electrical resistivity tomography (ERT) locations

In order to delineate weathered and fracture zones for groundwater potential, 2-D electrical resistivity tomography (ERT) was carried out. Four traverses were taken in the Sinthalakatttai (WE), Sillanatham (NS), Mupplipatti (NS) and Saverimangalam (WE) villages that are shown in Figure 3. In this study, SYSCOL JUNIOR Switch-48 model resistivity meter is used and Wenner-Schlumberger configuration was adopted. In a straight line, 48 electrodes have been planted at an interspacing of 3 m. The raw data were processed and interpreted using RES2DINV software. The maximum depth interpreted was 26 m. The data were filtered to remove bad datum points and inverted to estimate the true resistivity of the subsurface.

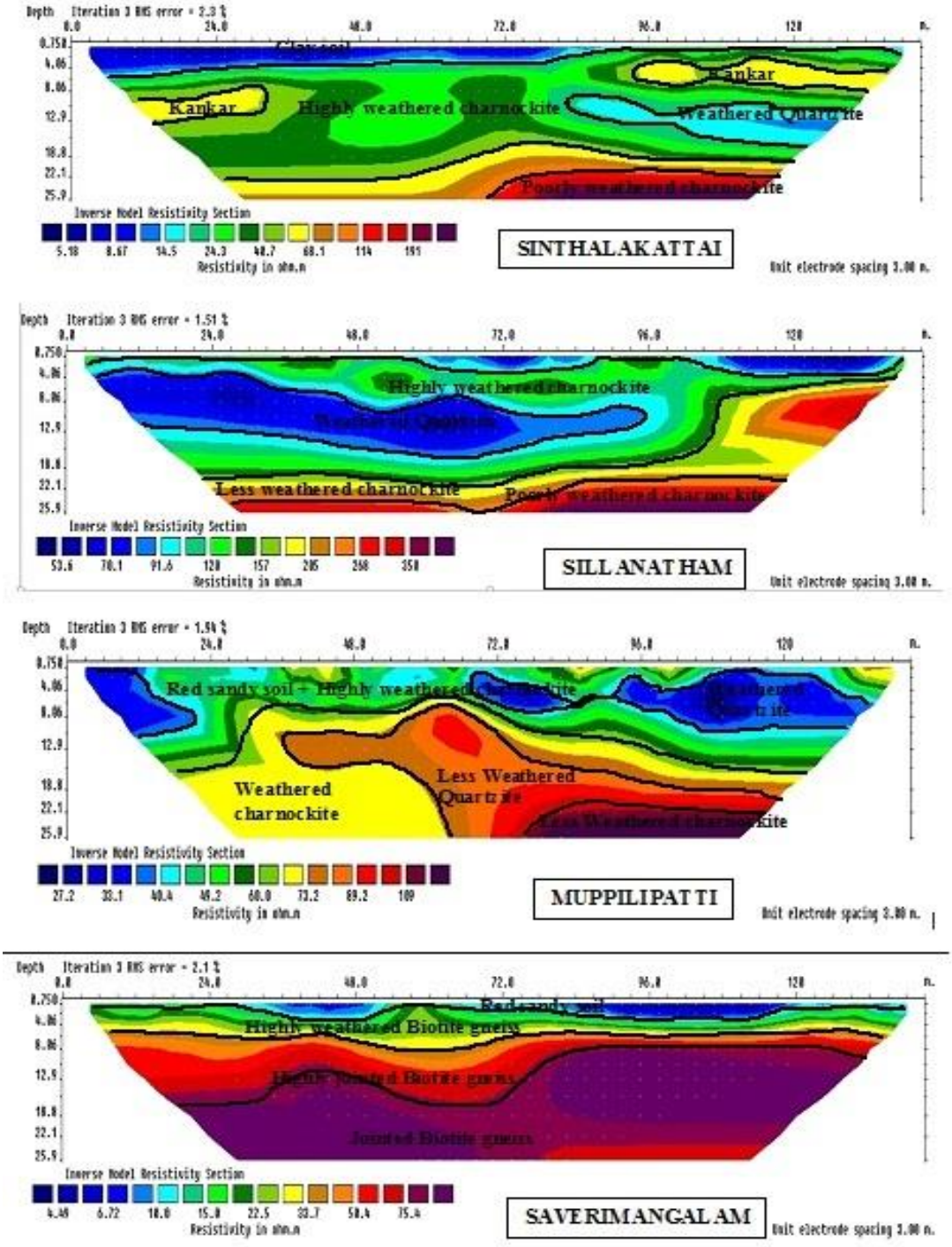

Figure 4. Interpreted electrical resistivity tomography (ERT) models at different studied locations

RESULTS AND DISCUSSION

The interpreted resistivity model represents stratified layers with small anomalies. Resistivity varied from < 5 Ohm m to > 350 Ohm m. Low resistivity was noted in Saverimangalam and high resistivity in Sillanatham village. Considering the resistivity range and its trend, geo-electric layers were recognised. The interpreted resistivity model of the locations is presented in Figure 4. Lithological characteristics are discussed below.

Sinthalakattai

The 2D resistivity model for Sinthalakattai profile is represented by four layered sections. Along this 144 m long WE profile, measured resistivity varies from < 5 to 191 Ohm m. The first layer resistivity varies from < 5 to 15 Ohm m. The thickness of the layer is about 6 m bgl in the western side, which gradually decreases and terminates at middle part of the profile. Low resistivity represented in western side of the first layer could be attributed by clay soil and relatively increased resistivity is due to less clay content and dryness. In the second layer, resistivity varied from 24 to 41 Ohm m and the thickness from 1 m to 20 m. Thickness is 8 m bgl in the western side and 2 to 8 m bgl in the eastern side of the profile. Second layer resistivity could be attributed by highly weathered charnockite wherein two anomalies were identified. Resistivity of the anomalies is 41 to 68 Ohm m and 15 to 24 Ohm m. It could be ascribed to the presence of kankar and quartzite veins saturated with water. In the third layer, resistivity varied from 41 to 114 Ohm m. The layer is little thicker in the western side. It gradually thins down towards the eastern side. The fourth layer has a resistivity of 114 Ohm m to about 200 Ohm m. The third layer could be represented by presence of less weathered charncokite and the fourth layer could be poorly weathered charcnockite.

Sillanatham

The 2D resistivity model for Sillanatham profile is represented by four layered section. This NS profile is 144 m long and measured resistivity varies from 53 to 350 Ohm m. The first layer resistivity varied from 53 to 70 Ohm m and the layer thickness is <1 m on the northern side of the profile while 2 to 4 m on the southern side. The resistivity of first layer is attributed by red sandy soil and relatively decreasing resistivity in the southern side is due to little wet condition. In the second layer, resistivity varied from 120 to 157 Ohm m. The thickness of the layer is about 18 m on the northern side which decreases about 4 to 5 m on the southern side of the profile. The resistivity of second layer could be attributed by weathered quartzite and weathered charnockite. Within the second layer, an anomaly was identified with resistivity of <53 to 92 Ohm m which could be ascribed to weathered quartzite saturated with water. In the third layer, resistivity varied from 157 to 205 Ohm m. Thickness is about 3 m on the northern side while increases towards southern side of the profile. Third layer resistivity is due to less weathered quartzite and charnockite. The fourth layer has a resistivity of about 205 to 350 Ohm m and thickness of the layer varied from 4 to 6 m and could be ascribed by poorly weathered or massive charnockite.

Muppilipatti

Here too, the 2D resistivity model is represented by four layered section. Along this 144 m long NS profile, measured resistivity varies from 27 to 109 Ohm m. The first layer resistivity varied from 27 to 60 Ohm m and a small discontinuous patch of anomaly with resistivity <27 to 41 Ohm m was noticed. The layer is thicker on either side of the profile and thinner in the central part. First layer resistivity could be attributed by red sandy soil and highly weathered charnockite. The anomaly is due to weathered quartzite saturated with water. In the second layer, resistivity varied from 60 to 73 Ohm m while layer thickness is high and thins down towards southern side of the profile. The second layer resistivity could be ascribed to weathered charnockite saturated with water. Third layer resistivity varied from 73 to 89 Ohm m. Similar to first layer, third layer thickness too thins on either side of the profile and thick at the centre. The third layer resistivity could be attributed by weathered quartzite with under saturation condition. Fourth layer resistivity varied from 89 to 109 Ohm m and the layer noticed at mid of the profile about side 18 m bgl. The fourth layer resistivity could be ascribed to the presence of poorly weathered charnockite.

Saverimangalam

In the 2D resistivity model for Saverimangalam profile, measured resistivity varies from 4 to 75 Ohm m. First layer resistivity varied from 4 to 10 Ohm m. The layer appeared as discontinued patches from west to east of the profile and this layer is very thin. First layer resistivity could be attributed by red sandy soil and the resistivity variation is due to presence of clay content or manure added to the soil. Second layer resistivity varied from 10 to 34 Ohm m and the layer is very thin on western side of the profile and gets gradually thicker towards eastern side. Third layer resistivity varied from 34 to 51 Ohm m. The layer is little thicker in the western side and gradually thins towards the eastern side. The second layer resistivity could be attributed by highly weathered biotite gneiss, while the third layer could be presence of highly jointed biotite gneiss. In the fourth layer, resistivity varied from 51 to 75 Ohm m. Similar to third layer, layer thickness thick to thin from western side to eastern side. The fourth layer resistivity could be attributed by highly jointed gneiss saturated with water.

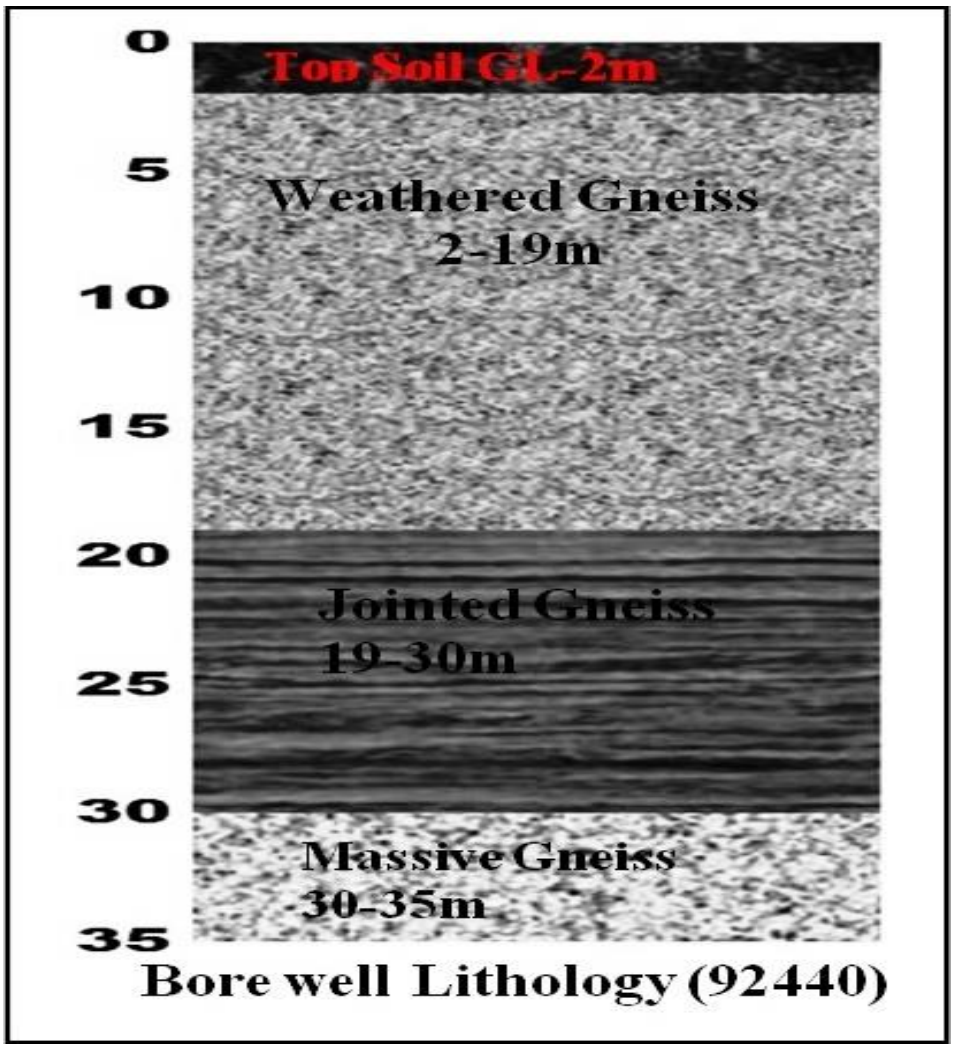

Figure 5. Lithology in the drilled bore well, located in the studied region

RESISTIVITY MODEL AND LITHOLOGY

The delineated resistivity layers from this study matched with the bore well lithology. The lithology is taken from a profile from Thoothukudi District prepared by Public Works Department (PWD, 2005). It is presented in Figure 5. Location of the bore well Gavarnagiri (Well No.92440) is near to the study locations. The village comes under the revenue block of Ottapidaram. Drilled depth of the bore well is 35 m and rock type is gneiss. The lithology represents top soil thickness of about 2m from ground level. Weathered gneisses are present from 2 to 19 m bgl and jointed gneisses from 19 to 30 m bgl. Similarly, massive gneiss is seen present from 30 m to the drilled depth of 35m. Resistivity model of the study locations are represented by 4 layers similar to the bore well lithology. It indicates that interpreted resistivity model matches closely with the sub surface lithology in the existing borehole.

CONCLUSION

The resistivity model in the studied locations reveals existence of four layered subsurface section. The resistivity varied from < 5 Ohm m to > 350 Ohm m. Low resistivity was noted in Saverimangalam and high resistivity in Sillanatham localities. High resistivity in Sillanatham is due to compaction and lack of fractures in the charnockite. Sinthalakattai and Mupplipatti resistivity models confirms with the presence of fractured layers. These two locations are suitable for shallow depth groundwater development up to 15 m bgl. In Saverimangalam, low resistivity is attributed to highly weathered or jointed rocks with the possibility of saline water. The anomaly represented in Sillanatham could be related to quartzite intrusion. Similarly, the anomaly with irregular pattern noticed in Mupplipatti, could be structural disturbance or quartzite intrusion with water saturation. The existing bore well lithology show appreciable match with

the derived resistivity models. It indicates the reliability of the tomography technique for sub surface resistivity studies, particularly in groundwater exploration.

ACKNOWLEDGEMENT

This work is a part of sponsored research project funded by Science and Engineering Research Board, DST, Government of India, New Delhi and the sanction No. is DST-SERB-SB/EMEQ-490/2014; Dt.25.07.2014. Author thanks the reviewer for his critical review and valuable suggestions.

Compliance with Ethical Standards

The authors declare that they have no conflict of interest and adhere to copyright norms.

REFERENCES

Archana Kumari., Kumar, D. and Warwade, P., 2021. Application of multi-criteria decision making (MCDM) and electrical resistivity tomography (ERT) techniques for identification of groundwater recharge zone(s) in granitic hard rock aquifer, J. Earth Syst. Sci., 130, 81.

Arsène, M., Elvis, B.W.W., Daniel, G., Théophile, N., Kelian, K. and Daniel, N.J., 2018. Hydrogeophysical Investigation for Groundwater Resources from Electrical Resistivity Tomography and Self-Potential Data in the Méiganga Area, Adamawa, Cameroon, Int. J. Geophys., Article ID 2697585, https://doi.org/10.1155/2018/2697585.

Barker, R.D., 1981. The offset system of electrical resistivity sounding and its use with a multicore cable. Geophys. Prospect., 29, 128-143. DOI: 10.1111/j.1365-2478.1981.tb01015.x.

Bhattacharya, P.K. and Patra, H.P., 1968. Direct current geoelectric sounding, principles and interpretation, methods in geochemistry and geophysics, vol 9. Elsevier Publishing Company, Amsterdam 135p.

Dahlin, T., 1996. 2D resistivity surveying for environmental and engineering application. First Break, 14, 275–283.

El-Qady, G., Ushijima, K. and El-Sayed, A., 2000. Delineation of a geothermal reservoir by 2D inversion of resistivity data at Hammam Faraun area, Sinai, Egypt. In: Proceeding of the World Geothermal Congress pp 1103–1108.

Gupta, G., Patil, J.D., Saumen Maiti., Vinit C. Erram., Pawar, N.J., Mahajan, S.H and Suryawanshi, R.A., 2015. Electrical resistivity imaging for aquifer mapping over Chikotra basin, Kolhapur district, Maharashtra, Environ Earth Sci., DOI 10.1007/s12665-014-3971-5.

Griffiths, D.H. and Barker, R.D., 1993. Two dimensional resistivity imaging and modeling in areas of complex geology. J. Appl. Geophys., 29, 211–226.

Hermans, T., Vandenbohede, A., Lebbe, L., Martin, R., Kemna, A., Beaujean, J., Nguyen, F., 2012. Imaging artificial salt water infiltration using electrical resistivity tomography constrained by geostatistical data. J. Hydrol., 438–439,168–180.

Keller, G.V. and Frischknecht, F.C., 1966. Electrical methods in geophysical prospecting. Pergamon Press Inc, Oxford.

Koefoed, O., 1979. Geosounding principles 1: Resistivity sounding measurements. Elsevier Science Publishing Company, Amsterdam.

Kumar, D., Thiagarajan, S. and Rai, S.N., 2011. Deciphering Geothermal Resources in Deccan Trap Region using Electrical Resistivity Tomography Technique. J. Geol. Soc. India, 78, 541–548.

Loke, M.H. and Barker, R.D., 1996. Rapid least-squares inversion of apparent resistivity pseudosections using a quasi-Newton method. Geophys. Prosp., 44, 131-152.

Loke, M.H., 2000. Electrical Imaging s Surveys for Environmental and Engineering Studies, a practical guide to 2-D and 3-D surveys, Penang, Malaysia.

Mainoo, P.A., Manu, E., Yidan, S.M., Agyekum, W.A., Tibore, S., Duah, A.A. and Kwasi, P., 2019. Application of 2D-Electrical resistivity tomography in delineatinggroundwater potential zones: Case study from the voltaian super group of Ghana. J. African Earth Sci.,, 160, 103618.DOI: 10.1016/j.jafrearsci.2019.103618.

Maiti, S., Erram, V.C., Gupta, G. and Tiwari, R.K., 2012. ANN based inversion of DC resistivity data for groundwater exploration in hard rock terrain of western Maharashtra (India). J. Hydrol. 464–465, 281–293. doi:10.1016/ j.jhydrol.2012.07.020.

Medeiros, W. and Ede Lima, O.A.L., 1990. A geoelectrical investigation for groundwater in crystalline terrains of Central Bahia, Brazil. Ground Water, 28, 518-523. DOI:10.1111/j.1745-6584.1990.tb01707.x.

Mohanti, M., 2009. Climate change on water resources: Indian perspective, Proc.vol.IGC's 16th convention, Feb 2-4, 165-167.

Mondal, N.C., Singh, V.P. and Ahmed, S., 2013. Delineating shallow saline groundwater zones from Southern India using geophysical indicators. Environ. Monit. Assess., 185, 4869–4886.

Niculescu, B.M. and Andrei, G., 2021. Application of electrical resistivity tomography for imaging seawater intrusion in a coastal aquifer. Acta Geophys., https://doi.org/10.1007/s11600-020-00529-7.

Owen, R.J., Gwavava, O. and Gwaze, P., 2005. Multi-electrode resistivity survey for groundwater exploration in the Harare greenstone belt, Zimbabwe. Hydrogeol. J., 14, 244–252.

Pawar, N.J., Pawar, J.B., Supekar, A., Karmalkar, N.R., Kumar, S. and Erram, V.C., 2009. Deccan dykes as discrete and prospective aquifers in parts of Narmada-Tapi zone, Dhule District, Maharashtra. In Indian Dykes (eds Srivastava, R.K., Sivaji, Ch. and Chalapathi Rao, N.V.), Narosa Publishing House Pvt Ltd, New Delhi, 189-198.

PWD, 2005. A Profile of Thoothukudi District, State Ground and Surface water Resources, Public Works Department, Government of Tamil Nadu, p.114.

Rai, S.N., Thiagarajan, S. and Ratnakumari, Y., 2011. Exploration of groundwater in the basaltic Deccan traps terrain in Katol taluk, Nagpur district, India. Curr. Sci., 101(9), 1198–1205.

Rai, S.N., Thiagarajan, S., Shankar, G.B.K., Sateesh Kumar, M., Venkatesam, V., Mahesh, G. and Rangarajan, R., 2015. Groundwater prospecting in Deccan traps covered Tawarja basin using Electrical Resistivity Tomography, J. Ind. Geophys. Union, 19(3), 256-269.

Ratnakumari, Y., Rai, S.N., Thiagarajan, S. and Kumar, D., 2012. 2D Electrical Resistivity Imaging for Delineation of Deeper Aquifers in a Part of the Chandrabhaga River Basin, Nagpur District, Maharashtra, India. Curr. Sci., (Bangalore), 102, 61-69.

Sarma, V.S., 2014. Electrical Resistivity(ER), Self Potential (SP), Induced Polarisation (IP), Spectral Induced

Polarisation (SIP) and Electrical Resistivity Tomography (ERT) prospection in NGRI for the past 50 years-A Brief Review, J. Ind. Geophys. Union, 18(2), 245-272.

Sarma,V.S. and Rajendra Prasad, P., 2006. HERT studies for sub-surface scanning, Proceedings of the International Conference on Ground Water - Organised by JNU, New Delhi during 1-4.

Sathish, S., Elango, L., Rajesh, R. and Sarma, V.S., 2011. Assessment of Seawater mixing in coastal acquiferby high resolution electrical resistivity tomography Int.J.Environ Sci.Tech., 8(3), 483-492.

Suski, B., Lander, F., Baron, L., Vuataz, F.D., Philippossian, F. and Holliger, K., 2008. Detection and characterization of hydraulically active fractures in a carbonate aquifer: results from self-potential, temperature and fluid electrical conductivity logging in the Combioula hydrothermal system in the southwestern Swiss Alps. Hydrogeol. J., 16, 1319-1328.

Taylor, R. and Howard, K., 2000. A tectono-geomorphic model of the hydrogeology of deeply weathered crystalline rock: evidence from Uganda. Hydrogeol. J., 8(3), 279–294.

Thiagarajan, S., Rai, S.N., Dewashish Kumar, and Ajai Manglik., 2018. Delineation of groundwater resources using electrical resistivity tomography, Arab. J. Geosci., 11(9), DOI: 10.1007/s12517-018-3562-y.

Vann, S., Puttiwongrak, A., Suteerasak, T. and Koedsin, W., 2020. Delineation of Seawater Intrusion Using Geo-Electrical Survey in a Coastal Aquifer of Kamala Beach, Phuket, Thailand, Water, 12, 506; doi:10.3390/w12020506.

Wyns, R., Gourry, J.C., Baltassat, J.M. and Lebert, F., 1999. Caractérisation multiparamètres des horizons de subsurface (0–100 m) en contexte de socle altéré. In: BRGM, IRD, UPMC, I. (Ed.), 2ème Colloque GEOFCAN, 105–110. Orléans, France.

Received on: 08.03.2021; Revised on: 22.09.2021; Accepted on: 20.11.2021

J. Ind. Geophys. Union, 26(1) (2022), 55-61

Interplay between climate, tectonics and sea level changes in shaping the geomorphic landscape of the Mainland Gujarat, western India: A review

Nikul P. Desai* and Shital H. Shukla
Department of Earth Science, Gujarat University, Ahmedabad, Gujarat
*Corresponding author: nikul.02.17@gmail.com

ABSTRACT

The landscape of Mainland Gujarat has experienced processes which are governed by external forcings viz., climate, tectonic and sea level changes. However, the studies carried out so far have been focused on each of these factors in different pockets of this vast region. The Kachchh region has mostly attracted research on tectonic aspect of Quaternary period and the Mainland Gujarat on tectonics as well as palaeoclimatic changes. In this review, we attempt to analyse all the available information pertaining to external forcings and their mechanisms, to evaluate the lacuna in the landscape evolution model and identify pathways for future research, especially in the Mainland Gujarat region. The climatic and tectonic studies have often not been integrated to deconvolute the imprints of each forcing in quantitative aspects. The review highlights the need for more chronologically supported analysis, which would be more quantified in nature rather than qualitative. The term neotectonic activity has been used widely in context of Gujarat, which needs to be supported with chronology for the realistic assessment of tectonic attributes.

Keywords: Gujarat mainland, Climate, Sabarmati River, Geomorphology, Tectonics

INTRODUCTION

The roles of climatic changes and tectonic instability in shaping the landscape have been debated since a long time (Schumm, 1977; Holbrook and Schumm, 1999). Indeed, these factors have together implicated changes in hydrological balance, sediment erosion and topography formation during the Quaternary times. To access this, the fluvial systems are most sensitive to tectonic or climatic perturbations as they archive these signatures in the form of erosion and/or deposition of sediments (Starkel, 2003). River systems respond in varying manner as per varying climatic conditions i.e., during dry conditions, they tend to produce enormous amount of sediments but due to poor discharge they are unable to erode and hence eventually, they lead to aggradation of valley. Contrastingly during wet climatic conditions, rivers will flush out the sediment produced and also lead to incision in the bedrock (Srivastava et al., 2008). However, it is widely believed that the response of 'Dryland Rivers' is quite complex (Tooth, 2000).

Gujarat Mainland, western India shows spectacular signatures of tectonic-climatic-sea level interplay. However, the research over this terrain has remained monotonous with focus only on tectonic or climatic forcings. In comparison, the Gujarat Alluvial Plains (GAP), have been studied well for palaeoclimatic and hydrological changes (Tandon et al., 1997; Jain and Tandon, 2003; Jain et al., 2004; Bhandari et al., 2005; Prasad et al., 2007; Sridhar et al., 2013; Prasad et al., 2014; Raj et al., 2015). The studies on fluvial systems of Mainland Gujarat alluvial plains have shown strong control of tectonic instability and palaeo-environmental changes during the Quaternary period (Srivastava et al., 2001; Chamyal et al., 2002, 2003; Bhandari et al., 2005; Raj 2007; Das and Solanki, 2020). Additionally, some archeological findings have hinted at eustatic-tectonic instability, which had affected the human settlements and led to their migration / collapse (Gaur and Vora, 1999; Khadkikar et al., 2004). However, the picture of climatic and tectonic interplay that led to evolution of this magnificent landscape of Mainland Gujarat, is still not clear. The aim of the present article is (i) to synthesize the available data on climatic and tectonic instabilities which governed the formation of present-day landscape of Mainland Gujarat covered by the fluvial sequences of Sabarmati, Mahi rivers, and (ii) to highlight the gaps in present understanding for future prospects.

STUDY AREA

Climate

The landscape of Mainland Gujarat is bordered by the great Thar desert of western India (Figure 1a, b). The present-day climate is predominantly controlled by the Indian Summer Monsoon (ISM) with periods of precipitation restricted between June–September with annual precipitation varying from 750 - 300 mm (Figure 1) (Chamyal et al., 2003). The landscape hosts semi-arid landforms and geomorphic features.

GEOLOGICAL AND TECTONIC FRAMEWORK

The Cambay basin is NNW-SSE oriented narrow graben that originated during the Mesozoic period during the break up of Gondwana land and the subsidence occurred during the Tertiary (Biswas, 1987). The basin extends from Tharad south-southeast through the alluvial plains of Gujarat, the

Gulf of Cambay and into the Arabian Sea in the western margin of India. Geologically, the Cambay basin comprises of igneous and metamorphic rocks of the Pre-Cambrian age at the basement level, overlain by the Mesozoic Formations. Mesozoic Formation are made up of Dhrangdhra, Wadhwan, Wagad, Himmatnagar Formations, overlain by the Deccan traps that contain multiple lava flows separated by thin intratrappean beds. Major part of basin is covered with thick Quaternary and Tertiary sediments (Merh, 1995). Quaternary sediments are mostly made up of thick unconsolidated sand, clay and gravels deposited by fluvial and aeolian activity (Merh, 1995).

Geomorphologically, the Cambay basin has been divided into the (i) northeastern rocky uplands consisting of Aravalli and trappean zone, (ii) piedmont zone, which is mainly covered by the fluvial sediments, (iii) alluvial zone, and (iv) coastal area in the south of the Cambay basin. The study area mainly comprises of alluvial plain of the Quaternary sediments, which are in the form of the channel fill and flood plain deposits.

The sequential fragmentation of western margin of Indian plate, as it collided with Eurasian plate during the Late Mesozoic, led to formation of three major rift systems namely Kachchh, Cambay and Narmada (Biswas, 1987). These basins have thus acted as major depocenters, accounting for a thick pile of sedimentation.

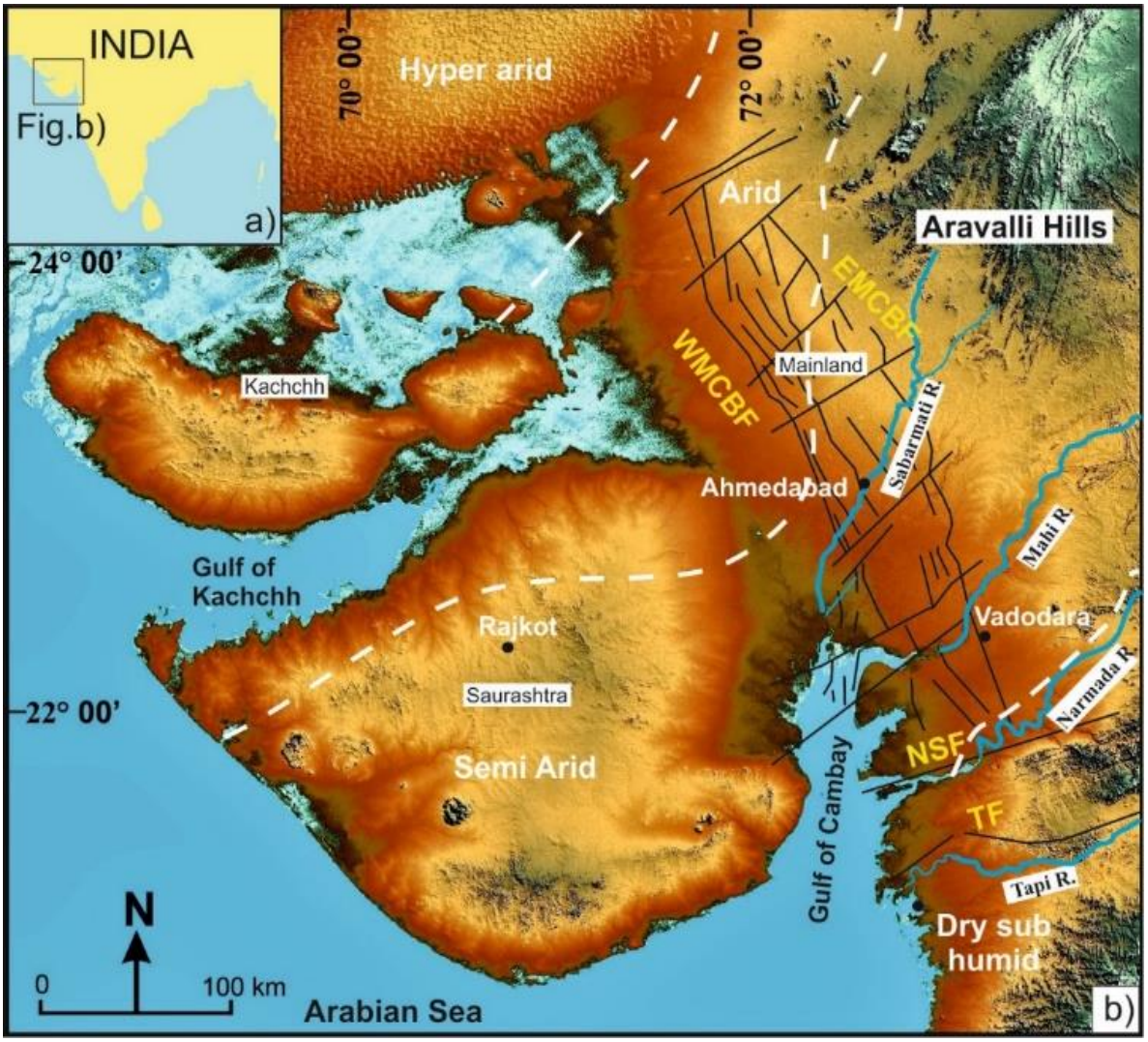

Figure 1. (a) Inset of the study area. (b) Terrain map of Gujarat with various climatic zones and major rivers of Mainland Gujarat (Modified after Chamyal et al., 2003, Juyal et al., 2006). TF – Tapti Fault, NSF – Narmada Son Fault, WMCBF – Western Margin Cambay Basin Fault, EMCBF – Eastern Margin Cambay Basin Fault.

The Late Cretaceous period witnessed the eruption of vast Deccan Trap formation, which covered in the most parts of Saurashtra and Kachchh. It was followed by Early Eocene transgression and subsequently the Tertiary sediments were deposited which are mainly of marine origin (Merh, 1995). The Quaternary sediments are predominantly of fluvial origin in entire Gujarat, especially the Mainland Gujarat which is vastly covered by the alluvial plains.

Tectonically, the basin is restricted by the Western Margin Cambay Basin Fault (WMCBF) in the west and Eastern Margin Cambay Basin Fault (EMCBF) in the east in Mainland Gujarat (Figure 1b). The basin is dissected by several E-W and ENE-WSW transverse faults from north to south, which led to five tectonic blocks, viz, Narmada block, Jambusar-Broach block, Cambay- Tarapur block, Ahmedabad - Mehsana block and Patan -Tharad- Sanchor block.

Geomorphic evidences of active tectonics and climatic reconstructions in Mainland Gujarat

Mainland Gujarat is mostly occupied by vast flat alluvial plains which are bordered by Aravalli and trappean outcrops to the east. Sabarmati, Mahi, Narmada and Tapti are the major rivers flowing through the Mainland Gujarat and have deposited huge thickness of Quaternary sediments. The Late Quaternary fluvial histories of these fluvial sequences have been studied in detail (Tandon et al., 1997; Jain et al., 1999; Kar et al., 2001; Chamyal et al., 2003; Jain et al., 2004; Bhandari et al., 2005; Raj, 2007). The oldest sequence dated in mainland Gujarat is of basal unit of Luni River with age of 400 ka BP (Jain et al., 1999) whereas the oldest sequence in Sarbamati is < 300 ka BP (Tandon et al., 1997) and 100 ka in Mahi (Juyal et al., 2000). Several workers have reported presence of bluish clay of marine origin as the basal unit of the exposed sections of Sabarmati, Mahi and Narmada rivers (Merh and Chamyal, 1997; Raj et al., 1998; Juyal et al., 2000; Chamyal et al., 2002, 2003) and its deposition is linked with the last interglacial (i.e., 125 ka) period when the sea level along the west coast of India was speculatively higher than present. This unit is overlain by gravel facie (Gm, Gc, Gh, Gms) which were deposited with an alluvial fan environment (Tandon et al., 1997; Chamyal et al., 1997, 2002). On the basis of OSL dating, Juyal et al. (2000) reported that aggradation phases in Mahi River basin are corresponding to marine isotopic stage 5 and 3. In an extensive review on monsoonal strength southern margin of Thar dessert, Juyal et al. (2006) suggests that the region experienced wetter phase during 130 – 120 ka, followed by subsequent reduction in precipitation during 120 – 100 ka. Whereas, the following period between 100 - 70 ka experienced enhanced monsoon with seasonality, followed by a phase of weak monsoon during 70 – 60 ka. The monsoon again enhanced during 60 – 30 ka leading to flood plain aggradation and pedogenesis. Again during 30 ka and 20 – 11 ka, dry phase in monsoonal conditions are observed, latter corresponding to the last glacial maximum. The fluvial records of the Early Holocene deposits from mainland Gujarat are absent. Prasad et al. (2007) studied the sedimentary sequence in lower Mahi River and reported cool and dry climate in the mainland Gujarat during 3660 to 2850 years BP. Whereas, on the basis of radiocarbon dating the valley-fill sequences in lower Mahi River, which shows the presence of foraminifers, yielded an age of 3660 ± 90 yr BP to 1760 ± 80 yr BP (Kusumgar et al., 1998), indicating their deposition during a sea level higher than present.

The Nal Sarovar, situated in a narrow depression between Little Rann of Kachchh and the Gulf of Cambay (present altitude of approx. 10 m from msl) was believed to be under shallow sea which linked the Little Rann of Kachchh with the Gulf of Cambay during the Late Quaternary Period (Figure 2a, c). The Nal region was studied using on a 54 m long core for its provenance, palaeoclimatic and palaeoenvironmental aspects (Prasad et al., 1997, 1998; Padrinath et al., 1999; Prasad and Gupta, 1999). They suggested that there was a sea linking the Gulf of Cambay and the Gulf of Kachchh during the last interglacial period (127 – 73 ka). However, they ruled out the possibility of high sea level reaching the Nal region during the Holocene period (7 ka to present). Despite this several authors have speculated that both these gulfs were connected during the Middle Holocene period (6 – 2 ka) (Chamyal et al., 2003), owing to few higher sea level signatures in form of marine terraces from the lower Mahi basin (Kusumgar et al., 1998) and oyster bed from the southern Saurashtra coast (Juyal et al., 1995). Recently Das et al. (2017) and Raj et al. (2021) reported the geological evidences of Mid-Holocene high from Kachchh coast and the Little Rann of Kachchh.

Several studies have attempted to document the role of tectonism in shaping the present-day landscape of mainland Gujarat (Srivastava et al., 2001; Chamyal et al., 2002; Raj et al., 2003,2004; Raj, 2007), however the understanding is still in its infancy owing to (i) lack of studies particularly aimed at documenting tectonic forcings on landscape modification, (ii) lack of chronological support and (iii) complexity in decoupling sea level change.

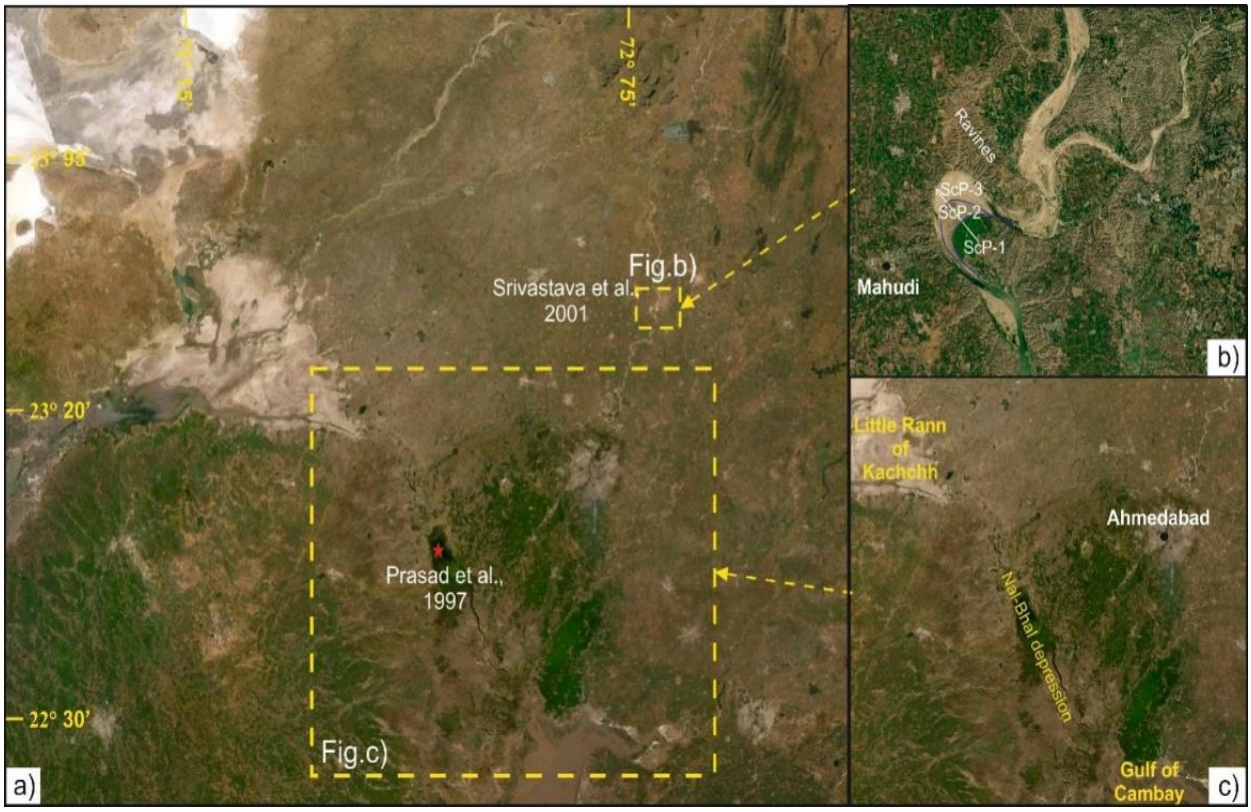

Figure 2. (a) Satellite image of the Mainland Gujarat with major geomorphic domains, (b) three scroll plains produced due to tectonic movement along the Sabarmati River (Modified after Srivastava et al., 2001), and (c) Nal-Bhal depression, which connects the Little Rann of Kachchh with the Gulf of Khambhat.

Presence of several drainage anomalies in form of tributaries on only one side of bank, offset channels, deep ravines, >40 m incised cliffs and gorge like valleys have been reported from the fluvial systems of mainland Gujarat (Srivastawa et al., 2001; Chamyal et al., 2002, 2003, Raj 2007). A major phase for realignment of drainages that suggested that large-scale river capture took place by structurally controlled major rivers was suggested on basis of several palaeochannels on western side of Sabarmati, Mahi and Orsang rivers (Tandon et al., 1997; Merh and Chamyal, 1997; Raj et al., 2000). Maurya et al. (1997, 2000) reported presence of seismites, age bracketed between 3.3 – 2.8 ka from the lower Mahi River basin. Srivastava et al. (2001) based on OSL dating of scroll plain sequence in lower Sabarmati River suggested that the basin had experienced two tectonic uplift events at 3 and 0.3 ka (Figure 2b). Similarly, Chamyal et al. (2002) studied the Narmada Son Fault (NSF) and suggested two major phases in tectonic activity, (i) slow synsedimentary subsidence of the basin during the Late Pleistocene, and (ii) inversion of the basin marked by differential uplift during the Holocene. Raj et al. (2004) and Raj (2007) studied the landform response of Dhadhar and Narmada rivers to tectonic activity along NSF during the Late Quaternary period.

Indeed, the fluvial sequences of mainland Gujarat have been studied in detail for their palaeohydrological aspects and palaeoclimatic signatures (Tandan et al., 1997; Juyal et al., 2000; Prasad et al., 2007; Sridhar et al., 2013), however there is still a need to strengthen the chronological background of these fluvial sequences namely Narmada, Tapti, Dhadhar. It is an accepted fact that the tectonism has played vital role in shaping landscape of mainland Gujarat and controlling the style of sedimentation, however only few studies have reported signatures of past tectonic activity (Maurya et al., 1997, Srivastava et al., 2001; Chamyal et al., 2002).

ARCHEOLOGICAL EVIDENCES

Various archeological studies have reported several pre-Harappan, Harappan and historical sites of human occupation from different parts of Gujarat**.** Offshore of the port Hazira, near Surat in the southern Gujarat mainland, a palaeochannel was discovered which was 20 – 40 m below present-day sea level and which had preserved several potsherds, lump of broken hearth and wattle and daub

(Kathiroli et al., 2004). TL dating of potsherds suggested that there was human activity during Early Holocene (i.e., 8 to 6 ka period) (Kathiroli et al., 2004). It is believed that this human activity ended during the Middle Holocene due to the rise in sea level (Kathiroli et al., 2004). Similarly, one of the most magnificent sites of Harappan civilization is Lothal ~ a port town, presently situated at 7 m above mean sea level and 23 km from the coastline shows most fascinating evidences of sea withdrawal since last 4000 years. Archeological findings from Lothal in form of Persian Gulf seal, terracotta models of African mummy and guerilla clearly suggested that Lothal had maritime connections and relations with Mesopotamia and Egypt (Rao, 1979; Gaur and Vora, 1999). Lothal thus shows evidences of southward shifting of sea by 23 km during the last 4000 years. Other sites like Kuntasi in northwest of Mainland Gujarat have been identified as small landing ports for the ancient settlers, however they are not well documented geologically for understanding human-landscape inter-relationship. Similarly, Rangpur located in hinterland of Lothal is believed to have been alternate settlement similar to Lothal, however owing to tremendous focus on Lothal had led to dismal efforts which would have been attempted on sites like Rangpur.

The archeological findings from different parts of Mainland Gujarat have shed light on sea level changes during the Holocene period and also hinted at ongoing tectonic activity. However there remains a need to corroborate these archeological evidences with other geological signatures to better understand the cultural and landscape evolution of this terrain.

DISCUSSION AND CONCLUSION

The landscape of Gujarat has evolved due to manifestation of climatic-tectonic-sea level interplay (Tandon et al., 1997; Srivastava et al., 2001; Chamyal et al., 2002; Jain and Tandon, 2003; Jain et al., 2004; Bhandari et al., 2005; Juyal et al., 2006; Sridhar, 2007; Raj, 2007; Sridhar and Chamyal, 2010; Sridhar et al., 2013; Das and Solanki, 2020; Raj et al., 2021; Solanki et al., 2021). However, the understanding of these forcing mechanisms is still in its infancy, primarily due to lack of chronological support and some ambiguous interpretations. In following points, we highlight the gaps in understanding which warrants urgent attention for better understanding of this magnificent landscape.

Incision in fluvial sequences can be on account of (i) enhanced monsoonal conditions, (ii) tectonic uplift and (iii) lowering of base level (Holbrook and Schumm, 1999; Blum and Tornqvist, 2000). However, in absence of detailed understanding of palaeoclimatic conditions in Mainland Gujarat region during the Quaternary period, it would be erroneous to link incision in fluvial sequences solely to neotectonic uplift. Early Holocene period between 6 - 9 ka is believed to be characterized by stronger monsoonal precipitation in the western India (Prasad and Enzel, 2006), can also account for such incised valleys. Similarly, several studies have shown that the increased incision near coastlines can also be due to lower sea strand (Leigh and Feeney, 1995). As per the sea level curve for west coast of India (Hashmi et al., 1995), the relative sea level was about 100 m below the present-day level during the Last Glacial Maxima (i.e., 20 ka), following which it had risen rapidly up to the Early Holocene period and reached its peak of 2 – 4 m higher than present day level around 6 ka. The relative sea level along the Gujarat coast was higher than present level around the Middle Holocene and relative sea level fell to present-day stand around 2ka (Hashmi et al., 1995; Chamyal et al., 2003; Das et al., 2017; Raj et al., 2021; Solanki et al., 2021).

We have identified some research gaps in our understanding of landscape evolution of Gujarat which can be taken up in future research. (i) The coastal sequences along with exposed fluvial sequences (>10 m) provide an ample opportunity for studying the land – sea interactions over this terrain. Similarly, the mainland Gujarat (i.e., Gujarat alluvial plains) has been studied extensively for the palaeo-hydrological and palaeo climatic aspects. However there exists only little systematic documentation of structural and tectonic elements (Raj et al., 2004; Raj, 2007, 2012), which limits our understanding of role of tectonism in shaping the present-day landscape. Major lacuna for this is the lack of chronological support. (ii)Another important aspect to study these exposed fluvial sequences would be palaeoclimatic proxies like geochemical analysis, mineral magnetic analysis, stable isotopic analysis and micropalaeontological analysis, coupled with constrained chronology, which would shed more light on tectonic-climatic interplay during the Late Quaternary period (Raj et al., 2015, 2021). Such attempts may be important in reconstructing an overall evolution of the Gujarat Mainland alluvial plains during the Quaternary Period. (iii) The climatic and tectonic studies have often not been integrated to deconvolute the imprints of each forcing in quantitative aspects. This can be envisioned with proper chronological support, which is major lacuna presently. (iv) The estuarine zones of various coastal as well as major rivers needs to be explored with geological and integrated archaeological studies, so as to better envision landscape change in response of human interaction during the Middle to Late Holocene period.

ACKNOWLEDGEMENT

The authors thank Department of Earth Science, Gujarat University for providing infrastructural support. The paper forms part of doctoral thesis of NPD. We thank two anonymous reviewers and the editor for their constructive suggestions which improved the paper.

Compliance with Ethical Standards

The authors declare that they have no conflict of interest and adhere to copyright norms.

REFERENCES

Bhandari, S., Maurya, D.M. and Chamyal, L.S., 2005. Late Pleistocene alluvial plain sedimentation in Lower Narmada Valley, Western India: Palaeo-environmental implications. J. Asian Earth Sci., 24, 433–444.

Biswas, S.K., 1987. Regional tectonic framework, structure and evolution of the Western marginal basins of India, Tectonophysics, 135, 307–327.

Blum, M.D. and Tornqvist, T.E., 2000. Fluvial responses to climate and sea-level change; a review and look forward. Sedimentology, 47, 2–48.

Chamyal, L.S., Khadkikar, A.S., Malik, J.N. and Maurya, D.M., 1997. Sedimentology of the Narmada Alluvial Fan, Western India. Sediment. Geol., 109, 263–279.

Chamyal, L.S., Maurya, D.M., Bhandari, S. and Raj, R., 2002. Late Quaternary geomorphic evolution of the lower Narmada valley, Western India: implications for neotectonic activity along the Narmada-Son Fault. Geomorphology, 46, 177- 202.

Chamyal, L.S., Maurya, D.M. and Rachna, R., 2003. Fluvial systems of the dry lands of western India: a synthesis of Late Quaternary environmental and tectonic changes, Quat. Int., 104, 69–86.

Das, A. and Solanki, T., 2020. Geological Signatures of Tectonic Instabiloity along the North Cambay Basin during the Late Holocene Period, North Gujarat, India. Geol. Soc. India, 96, 584-590.

Das, A., Prizomwala, S.P., Makwana, N. and Thakkar, M.G., 2017. Late Pleistocene-Holocene climate and sea level changes inferred based on the tidal terrace sequence, Kachchh, Western India. Palaeogeograp., Palaeoclimat., Palaeoecol., (PPP), 473, 82-93.

Gaur, A.S. and Vora, K.H., 1999. Ancient shorelines of Gujarat, India, during the Indus civilization (Late Mid-Holocene): A study based on archaeological evidences, Curr. Sci., 77, 180-185.

Hashimi, N.H., Nigam, R., Nair, R.R. and Rajagopalan, G., 1995. Holocene sea level fluctuations on western Indian continental margin: an update. J. Geol. Soc. India, 46, 157–162.

Holbrook, J. and Schumm, S.A., 1999. Geomorphic and sedimentary response of rivers to tectonic deformation: a brief review and critique of a tool for recognizing subtle epeirogenic deformation in modern and ancient settings. Tectonophysics, 305, 287–306.

Jain, M. and Tandon, S.K., 2003. Fluvial response to Late Quaternary climate changes, western India, Quat. Sci. Rev., 22, 2223–2235.

Jain, M., Tandon, S.K., Bhatt, S.C., Singhvi, A.K. and Mishra, S., 1999. Alluvial and aeolian sequences along the river Luni, Barmer District: physical stratigraphy and feasibility of luminescence chronology methods. Mem. Geol. Soc. India, 42, 273–295.

Jain, M., Tandon, S.K. and Bhatt, S.C., 2004. Late Quaternary stratigraphic development in the lower Luni, Mahi and Sabarmati River basins, western India. J. Earth System Sci., 113(2), 453-471.

Juyal, N., Pant, R.K., Bhushan, R. and Somayajulu, B.L.K., 1995. Radiometric dating of late Quaternary sea levels of the Saurashtra coast, Western India: an experiment with oyster and clam shells. Geol. Soc. India Mem., 32, 372–37.

Juyal, N., Rachna, R., Maurya, D.M., Chamyal, L.S. and Singhvi, A.K., 2000.Chronology of Late Pleistocene environmental changes in the lower Mahi basin, western India. J. Quat. Sci., 15, 501–508.

Juyal, N., Chamyal, L.S., Bhandari, S., Bhushan, R. and Singhvi, A.K., 2006. Continental record of the southwest monsoon during the last 130 ka: evidence from the southern margin of the Thar Desert, India, Quat. Sci. Rev., 25, 2632–2650.

Kar, A., Singhvi, A.K., Rajaguru, S.N., Juyal, N., Thomas, J.V., Banerjee, D. and Dhir, R.P., 2001. Reconstruction of late quaternary environment of the lower Luni plain, Thar Desert, India. J. Quat. Sci., 16, 61–68.

Kathiroli, S., Badrinarayanan, S., Rao, D.V., Sasisekaran, B. and Ramesh, S., 2004. Recent marine archaeological finds in Khambat, Gujarat. Journal of Indian Ocean Archaeology 1, 141-149.

Khadkikar, A.S., Rajshekhar, C. and Kumaran, K.P.N., 2004. Palaeogeography around the Harappan port of Lothal, Gujarat, western India. Antiquity, 78, 896-903.

Kusumgar, S., Raj, R., Chamyal, L.S. and Yadav, M.G., 1998. Holocene paleo-environmental changes in the lower Mahi basin, Western India. Radiocarbon, 40, 819.

Leigh, D.S. and Feeney, T.P., 1995. Paleochannels indicating wet climate and lack of response to lower sea level, Southeast Georgia. Geology, 23, 687-690.

Maurya, D.M., Malik, J.N., Rachna, R. and Chamyal, L.S., 1997. Soft-sediment deformation in the Quaternary sediments of the Lower Mahi Basin, Western India. Current Science 72, 519–522

Maurya, D.M., Rachna, R. and Chamyal, L.S., 2000. History of tectonic evolution of Gujarat alluvial plains, western India, during Quaternary: a review. J. Geol. Soc. India, 55, 343–366.

Merh, S.S., 1995. Geology of Gujarat, Geol. Soc. India, Bangalore, 222p.

Merh, S.S. and Chamyal, L.S., 1997. The Quaternary geology of Gujarat alluvial plains, Proc. Indian National Sci. Acad., 63, 1–98.

Padrinath, K., Prasad, S. and Gupta, S.K., 1999. A 75 ka Record of Palaeoclimatic Changes Inferred from

Crystallinity of Illite from Nal Sarovar, Western India. Geol. Soc. India, 54, 142-156.

Prasad, S. and Gupta, S.K., 1999. Role of eustasy, climate and tectonics in late Quaternary evolution of Nal-Cambay region, NW India. Z. Geomorphology, 43(4), 483-504.

Prasad, S. and Enzel, Y., 2006. Holocene paleoclimates of India. Quat. Res., 66, 442–453.

Prasad, S., Kusumgar, S. and Gupta, S.K., 1997. A mid to late Holocene record of palaeoclimatic changes from NalSarovar:apalaeodesert margin lake in western India. J. Quat. Sci., 12, 153–159.

Prasad, S., Pandarinath, K. and Gupta, S.K., 1998. Geomorphology, tectonism and sedimentation in the Nal region, western India. Geomorphology, 25, 207–223.

Prasad, V., Phartiyal, B. and Sharma, A., 2007. Evidence of enhanced winter precipitation and the prevalence of a cool and dry climate during the mid to late Holocene inmainland Gujarat, India, The Holocene, 17, 889–896.

Prasad, V., Farooqui, A., Sharma, A., Phartiyal, B., Chakraborty, S., Bhandari, S., Raj, Rachna, and Singh, A., 2014. Mid–late Holocene monsoonal variations from mainland Gujarat, India: a multiproxy study for evaluating climate culture relationship. Palaeogeogr. Palaeoclimatol. Palaeoecol. 397, 38–51.

Raj, R., 2007. Strike slip faulting inferred from offsetting of drainages: Lower Narmada Basin, western India. J. Earth System Sci., 116, 413-421.

Raj, R., 2012. Active tectonics of NE Gujarat (India) by morphometric and morphostructural studies of Vatrak River basin J. Asian Earth Sci., 50, 66–78.

Raj. R., Maurya, D.M., Chamyal, L.S., 1998. Late Quaternary sea level changes in western India: evidence from Lower Mahi valley. Current Sci., 74, 910–914.

Raj, R., Wadi, M.B., Maurya, D.M., Chamyal, L.S., 2000. Palaeochannels in the lower Mahi basin, Gujarat. Man and Environment, 25, 13–18.

Raj, R., Bhandari, S., Maurya, D.M. and Chamyal, L.S., 2003. Geomorphic indicators of active tectonics in Karjan River basin, Lower Narmada valley, Western India, J. Geol. Soc. India, 62, 739–752.

Raj, R., Mulchandani, N., Bhandari, S., Maurya, D.M. and Chamyal, L.S., 2004. Channel shifting of a highly sinuous meandering river in alluvial plain, Vishwamitri river, Mainland Gujarat. Current Sci., 86, 1647-1653.

Raj, R., Chamyal, L.S., Prasad, V., Sharma, A., Tripathi, J.K. and Verma, P., 2015. Holocene climatic fluctuations in the Gujarat Alluvial Plains based on a multiproxy study of the Pariyaj Lake archive, western India, Palaeogeograph.Palaeoclimat.Palaeoecol., 421, 60–74.

Raj, R., Tripathi, J.K., Kumar, P., Singh, S.K., Phartiyal, B., Sharma, A., Sridhar, A. and Chamyal, L.S., 2021. Palaeoclimatic and sea-level fluctuations from the last deglaciation to late Holocene from western India: Evidence from multiproxy studies. J. Asian Earth Sci., 214, 104777. doi.org/10.1016/j.jseaes.2021.104777

Rao, S.N., 1979. Lothal: A Port Town (1955-62): Archaeological Survey of India.

Scumm, S. A., 1977. The fluvial system: New York, John Wiley & Sons, 338 p.

Solanki, T., Prizomwala, S.P., Makwana, N. and Solanki, P.M., 2021. Assessing the climatically triggered aggradation-incision processes in a dryland environment during the Late Quaternary period from Shetrunji River basin (Saurashtra), India. Quat. Int., 585, 70-84.

Sridhar, A., 2007. Mid-late Holocene hydrological changes in the Mahi River, arid western India. Geomorphology, 88, 285-297.

Sridhar, A. and Chamyal, L.S., 2010. Sediment records as archives of the Late Pleistocene–Holocene hydrological change in the alluvial Narmada River basin, western India. Proc. Geologists' Assn, 121(2), 195-202.

Sridhar, A., Chamyal, L.S., Bhattacharjee, F. and Singhvi, A.K., 2013. Early Holocene fluvial activity from the sedimentology and palaeohydrology of gravel terrace in the semi arid Mahi River Basin, India .J. Asian Earth Sci., 66, 240-248.

Srivastava, P., Juyal, N., Singhvi, A.K. and Wasson, R.J., 2001. Luminescence chronology of river adjustment and incision of Quaternary sediments in the alluvial plains of Sabarmati River, north Gujarat, India. Geomorphology, 36, 217–229.

Srivastava, P., Tripathi, K.J., Islam and Jaiswal, K.M., 2008. Fashion and phased of late Pleistocene aggradations and incision in the Alaknanda River Valley, Western Himalayan, India. Quaternary Research 70, 68–80.

Starkel, L., 2003. Climatically controlled terraces in uplifting mountain areas. Quaternary Science Reviews 22, 2189–2198.

Tandon, S.K., Sareen, B.K., Someshwararao, M. and Singhvi, A.K., 1997. Aggradation history and luminescence chronology of Late Quaternary semi-arid sequences of the Sabarmati basin, Gujarat, western India. Palaeogeogeograph., Palaeoclimat., Palaeoecol., 128, 339–357.

Tooth, S., 2000. Process, form and change in dryland rivers: a review of recent research. Earth Sci. Rev., 51, 67–107.

Received on: 23.09.2021; Revised on: 16.10.2021; Accepted on: 03.11.2021

J. Ind. Geophys. Union, 26(1) (2022), 62-77

Investigations of organic matter in meteorites using Fourier transform infrared and micro-Raman spectroscopic methods: Implications for origin of extraterrestrial organic matter

Bhaskar J. Saikia[1*], G. Parthasarathy[2] and Rashmi R. Borah[3]

[1] Department of Physics, Anandaram Dhekial Phookan College, Nagaon -782002, India
[2]School of Natural Sciences and Engineering, National Institute of Advanced Studies, Indian Institute of Science Campus, Bengaluru-560012, India
[3]Department of Physics, Nowgong College (Autonomous), Nagaon 782001, India
*Corresponding author: vaskaradp@gmail.com

ABSTRACT

We present here the evidence for the presence of organic matters in Dergaon, Mahadevpur and Natun Balijan ordinary chondrites using Fourier transforminfrared and micro-Raman spectroscopic technique. The Fourier transforminfrared spectrum of these ordinary chondrites in the range 2700–3000 cm^{-1} indicates the presence of CH_3 asymmetric stretching, and CH_2symmetric and asymmetric stretching modes due to aliphatic hydrocarbons. The micro-Raman spectrum exhibits the diamond and graphite peaks correspondingly at 1331 cm^{-1}, 1349 cm^{-1} and 1588– 1618 cm^{-1}. The full wave at half maximum value correspondingly 120 cm^{-1}, 70 cm^{-1} and 17.5 $cm^{-1}$for Dergaon, Mahadevpur and Natun Balijan, indicate the nature of disordered phase involved shock metamorphism in the meteorites. The diamond and graphite peaks intensity ratios of ~1.121, ~1.075 and ~0.532, correspondingly for Dergaon, Mahadevpur and Natun Balijan, indicates the disordered nature of graphite. This study has strong implications in understanding of the origin of organic matters in extra-terrestrial materials and origin of extraterrestrial life.

Keywords: Organic compound; Dergaon, Mahadevpur and Natun Balijan chodrites; diamond and graphite; Infrared and micro-Raman spectroscopic methods, Extraterrestrial life

INTRODUCTION

The formation of our solar system started around 4.6 G yr ago, as this is the oldest age calculated so far for any material formed in it (Cronin et al., 1988; Cassen and Boss, 1988; Ahrens, 1990; Bouvier and Wadhwa, 2010). All solar system objects like asteroids, planetary satellites, dwarf planets, major planets and comets were formed from the nebular dust and gas within the first 10-100 million years after the formation of the first solar system solids (Montmerle et al. 2006). Most meteorites originated from different solar system bodies formed during the accretion processes that took place in the first few Myr, thus they vary in elemental and isotopic composition. Consequently, meteorites are an important source of extraterrestrial matter and their chemical and physical characteristics, texture and internal structure contribute to our understanding of the birth and early history of our solar system (McSween, 1999). The most common type of meteorites is chondrites and they originate from debris of the solar nebula (e.g., Brearley, 2003; Hutchison, 2004).

Carbon is one of the most abundant elements in the interstellar and circumstellar medium. In interstellar medium, carbon compounds occurs in different forms, including hydrocarbon dust, graphite, amorphous carbon, and diamonds. About ~4 × 10^7 kg of extraterrestrial material, ranging in size from meter-sized meteorites down tomicron-sized interplanetary dust particles (IDPs), rains down on the Earth every year (Love and Brownlee, 1993). On an average, IDPs contain about 12 wt% carbon (Thomas et al., 1993, 1994), approximately half of which is organic matter (Flynn et al., 2004). The flux of exogenous organic matter delivered to the early Earth by IDPs and carbon-rich meteorites ~4 billion years ago, may have been orders of magnitude higher than the present rate with estimates of up to 10^9 kg/year of organic carbon (Jenniskens et al., 2000). The carbon phases are commonly found in carbonaceous chondrites. When C60and C70 fullerenes were discovered along with the presence of poly aromatic hydrocarbons and carbon clusters in Allende Meteorite, Becker et al. (1999) found C60 and C70, as well asa unique distribution of remarkably stable clusters of C100 to C400. These large extra-terrestrial carbon clusters are either the first indication of higher fullerenes in Allende meteorite. Fullerenes are an allotropic modification of carbon, often termed as a molecular form of carbon, or carbon molecules. Fullerenes were discovered in 1985 by H.W. Kroto, R.F. Curl and R.E. Smalley (Frans, 2006; Misra et al., 2007) who were later awarded with the nobel prize for chemistry in 1996. The fullerene family includes a number of atomic C n clusters (n > 20), composed of carbon atoms on a spherical surface. Carbon atoms are usually located on the surface of the sphere at the vertices of pentagons and hexagons. In fullerenes, carbon atoms are usually present in the sp2-hybrid form and linked together by covalent bonds. Fullerene C60 is the most common and best-investigated fullerene. The spherical molecule is highly symmetric and consists of 60 carbon atoms, located at the vertices of twenty hexagons and twelve pentagons. The diameter of fullerene C60 is 0.7 nm. Becker et al. (1999) had suggested

that unlike other proposed carbon carriers, nanodiamond, SiC, graphite and phase Q, fullerenes are extractable in an organic solvent. It is this unique property, in fact, this may be why fullerene molecules or fullerene-related compounds were overlooked as a carrier phase of extra-terrestrial gases in meteorites. Fullerene, like other carbon carriers, were transported to the solar nebula, accreted into carbonaceous chondrites and delivered to the terrestrial planets.

Carbonaceous chondrites are among the most primitive meteorites but less abundant than ordinary chondrites. Based on spectrographic studies, C-type asteroids are the best asteroidal analogues for carbonaceous chondrites (Burbine et al., 2002; Consolmagno et al., 2008). Carbon matter is commonly found in the carbonaceous chondrites in various forms, including carbonates and minor amounts of presolar grain material such as diamond, graphite, and silicon carbide (Lewis et al., 1987; Ott, 1993; Huss and Lewis, 1995; Lodders and Amri, 2005). Analyses of carbonaceous chondrites also have revealed a major insoluble organic component consisting of >50% of the total organic carbon (Alexander et al., 2007), as well as a complex and highly diverse suite of soluble organics (Sephton, 2002; Pizzarello et al., 2006; Schmitt-Kopplin et al., 2010). The insoluble organic matter (IOM) found in primitive meteorites was formed in the early solar system and subsequently processed on the parent body or asteroids. Generally the CI, CR and CM groups of carbonaceous meteorites exhibit the highest content of a primitive organic matter (up to 4 wt%), mainly in the form of an insoluble macromolecular solid with large diversity of functional groups (Robert and Epstein, 1982; Alexander et al., 1998, 2007). Allamandola et al. (1992) first reported the infrared spectra of some dense interstellar clouds exhibiting a broad absorption feature around at ~2880 cm^{-1} (3.47 μm). Further investigations confirm that these infrared features to tertiary C-H groups (with a large diversity of functional groups of both sp3 and sp2 carbons present together with heteroatoms such as O, N and S) and proposed the carrier to be a diamond-like material (Alexander et al., 1998, 2007; Bauschlicher et al., 2007; Pirali et al., 2007; Mennella, 2008; Derenne and Robert, 2010). There are some evidences of carbon which is frequently associated with Fe-Ni metal (McKinley et al., 1981; Scott et al., 1988; Cronin et al., 1988, 1993a; Brearley et al., 1989), and carbon of unknown chemical form has been identified at the surface of metal and troilite grains in ordinary chondrites (Makjanic et al., 1993). In unequilibrated ordinary chondrites (UOCs), the carbon content usually ranges from 0.2 to 0.6%, but reaches 1% in a few cases (Smail et al., 2000). The analyses of Orgueil and other meteorites had identified the presence of saturated hydrocarbons in meteorites (Wang et al., 2004a; 2004b). A wide range of aromatic hydrocarbons and polycyclic aromatic molecules in different meteorites have been identified using gas chromatography, spectroscopic techniques (infrared, ultraviolet, and fluorescence) and mass spectrometry (Wang and Chen, 2006; Wang et al., 2006; Gillet et al., 2007; Quirico et al.,2009, 2014). In many meteorites, the insoluble organic material like aliphatic carbon, appears in the form of methyl, methylene, and methine groups (Quirico et al., 2005; Bonal et al., 2006, 2007). Carboxlyic acids and aliphatic dicarboxylic acids also have been remarkably observed in different meteorites like Murchison, Murray, Asuka, Yamato, Orgueil and Tagish Lake meteorite etc (Briggs and Mamikunian, 1964; Epstein et al., 1987; Cooper and Cronin, 1995;Hiroi et al., 2001; Pizzarello et al., 2001;Martins et al., 2006).A numbers of researchers suggested that the volatile organic compounds including aldehydes, amides, amines, mono and di-carboxylic acids, aliphatic and aromatic hydrocarbons, heterocyclic aromatics, hydroxy acids, ketones, phosphonic and sulfonic acids, fatty acids, purines, pyrimidines are present in meteorites (Cronin and Chang,1993; Cronin et al., 1993; Palme, 2000). However, the amino acids have been observed with large compositional variability in different meteorites including Tagish Lake meteorites (Pizzarello et al., 2001), and meteorites found in Antarctica (Shimoyama et al., 1979; Cronin et al., 1979), CI chondrites (Kvenvolden et al.,1970), CM chondrites (Kvenvolden et al., 1970; Cronin and Pizzarello, 1990; Komiya et al., 2003; Koga and Naraoka, 2017), and CR chondrites (Cronin and Moore, 1976; Shimoyama et al., 1985; Pizzarello and Cronin, 2000). More than seventy amino acids have been identified in different meteorites (e.g., Kvenvolden et al., 1970; Cronin et al., 1981; Engel and Nagy, 1982). Extraterrestrial delivery of organic compounds including amino acids to the early Earth prior to the generation of life may have been important for the origin of life. Other organic compounds like sulfonic acids, phosphonic acids, N-heterocycles, amines, amides, polyols and imino acids are also observed in different carbonaceous chondrites and interplanetary dust particles (IDPs) (Cooper et al., 1992; Pizzarello et al., 1994; Cooper and Cronin, 1995; Cooper et al., 2001; Huang et al., 2005; Lerner and Cooper, 2005). Furthermore, the primitive meteorites allow mineralogical evidence of post accretion processes; therefore, the identification of meteoritic organic features can provide an understanding how IOM chemical variability observed among chondrite groups relates to parent body processes (e.g. Bonal et al., 2007; Busemann et al., 2007, 2009; Quirico et al., 2011; Yabuta et al., 2010). These organic molecules are therefore believed to be a biogenic (Cronin et al., 1988), having been produced by chemical rather than biologic processing. Exogenous delivery of organics to the earth's surface could have been

an important source of these molecules on the pre-biotic earth (Parthasarathy et al., 1998, 2005, 2008)

Commonly organic carbons including polycyclic aromatic hydrocarbons (PAHs), are found in carbonaceous meteorite. However, the organic carbon in ordinary chondrite is very rare. Conversely, chondritic meteorites are the oldest and most primitive rocks in the solar system. Chondrites are stony meteorites that have not been modified due to melting or differentiation of the parent body. Chondrites are broadly ultramafic in composition, consisting largely of iron, magnesium, silicon and oxygen and account for 87% of all meteorites observed to fall. The largest group of chondritic meteorites is known as the ordinary chondrites, which account for 80% of all known meteorites (Philip et al., 2000). In this study we present our results on occurrence of organic carbon and nanodiamonds in three (Dergaon H5, Mahadevpur H4/5 and Natun Balijan L4) ordinary chondrites, using Fourier transform infrared and micro-Raman spectroscopic technique

EXPERIMENTAL TECHNIQUES

Raman spectroscopy is a non-destructive technique that can yield information on the structural order of polyaromatic organic matter when applied at low laser power. Therefore, it is used to investigate insoluble organic matter from a range of chondritic meteorites, and a suite of interplanetary dust particles (Fraundorf et al., 1982; Saikia et al., 2009a, b, 2017; Starkey et al., 2013; Starkey and Franchi, 2013). Raman analysis of insoluble organic matter has been already discussed by various authors in different meteorites (Bonal et al., 2006, 2007; Busemann et al., 2007; Dobrica et al., 2011), as well as of interplanetary dust particles (Allamandola et al., 1987; Quirico et al., 2005) and returned samples from the Stardust Mission (Wopenka et al., 2013). However, the infrared spectroscopy presents the advantage of being non-destructive technique; therefore, it is highly appreciated for analysing precious samples such as meteorites. This technique is the most powerful method to characterize the nature of carbonaceous matter present in meteorites. Moreover, the Raman and infrared spectra of a sample typically differ because Raman activity requires a change in polarizability during the transition, whereas infrared activity requires a change in dipole moment, consequently each technique can provide complementary information regarding the sample. With these two techniques, both the mineralogy of the matrix and the carbonaceous components can be investigated with a high spatial resolution (a few microns), allowing the detailed analysis of heterogeneous samples (Matrajt et al., 2004).

All the sample preparation was performed in ultra-clean conditions. To prevent from the environmental artefact contaminations, such as mud, the sample was carefully checked by optical microscopy. To avoid any surface contamination and the fusion crust, we fragmented the sample (~20 mg) and took only pieces coming from its interior. The Raman spectra were collected on bulk powdered meteorite samples using a Ar ion laser with a power of ~5 mW, which used an excitation source having a wavelength of 488 nm coupled with a Jobin-Yvon Horiba LabRam-HR Micro-Raman spectrometer (Horiba Scientific, USA) equipped with an Olympus microscope with 109, 509, and 1009 objectives. Powdered samples were selected for the present investigation instead of polished thin sections, as the latter will have textural and crystallite orientation effects in spectroscopic and powder XRD studies. Powder methods are more reliable for characterization of mineral phases. However, comparing to chemical analytical techniques such as gas and liquid chromatographies or stepped combustion where the sample is totally lost, or techniques such as SIMS and ICPMS where samples are strongly corroded, the crushing approach presents the advantage of not chemically or physically destroying the sample (Matrajt et al., 2004). A motorized x–y stage is included in this arrangement and used 1800 grooves mm^{-1} grating in the range from 100 to 3000 cm cm^{-1}. A silicon wafer (520.7 ± 0.5 cm^{-1}) was applied for calibration. The excellent accuracy (±0.5 cm^{-1}) and precision (±0.1 cm^{-1}) of peak positions for this instrument over the whole Raman spectral range make it relatively straightforward to use this technique to identify minerals based on their spectral signatures. An edge filter was used for measuring the exact Stokes lines. The data interpretation procedure used a Gaussian fit to find the exact position of the maximum of each peak. Minerals were identified by comparing the band positions in our spectra with the Raman data on the end member minerals at ambient pressure and temperature conditions (RRUFF-database http://rruff.info/). Raman data were collected at room temperature (30°C). Spectra were collected with counting times ranging between 10 and 60 s.

The powdered sample was homogenized in spectrophotometric grade KBr (1:20) in an agate mortar and was pressed 3mm pellets with a hand press. We tried to minimize the grinding time to avoid the deformation of the crystal structure, the ion exchange and the water absorption from atmosphere. The infrared spectra was acquired using Perkin-Elmer system 2000 FTIR spectrophotometer with helium-neon laser as the source reference, at a resolution of 4 cm^{-1}. The spectra were taken in transmission mode in the region 400− 4000 cm^{-1}. The room temperature was 30°C during the experiment. The 800-1100 cm^{-1} (10μm) and 800−400 cm^{-1} (20μm) region of the infrared spectra facilitate an understanding of the relative nature of the SiO_4 tetrahedra.

Particular interest is directed towards the presence of trace of organic compound in the spectral region around 2800-3000 cm^{-1}(3.4μm), due to the aliphatic functional CH_2 and CH_3 groups.

The composition of the meteorite samples was also determined by the X-ray diffraction technique (XRD) using PHILIPS PW 3710/31 diffractometer, scintillation counter, CuKα radiation and Ni filter at 40 kV and 35 mA (Philips, USA). This instrument is connected to a computer system using APD program and PDF-2 database for mineral identification. We used a 2θ range of 10–80° with a step size of 0.02° and a 0.5 s count time per step. The slits used consisted of 1° fixed divergence and anti scatter slits and a 0.2 mm receiving slit.

RESULTS AND DISCUSSION

Hydrocarbons in ordinary chondrites

Extraterrestrial organic compounds present in carbonaceous chondrites known to exhibit large structural diversity, which is a feature contrasting with terrestrial biogenic organic compounds. Potiszil et al. (2017) have carried out high pressure spectroscopic measurements on organic materials and suggested that the formation of the hydrogen bonds has implications for the origination of macromolecular organic matter (MOM) in the extra terrestrial materials. Such high-pressure-induced hydrogen-bond formation is likely a process by which aromatic MOM precursors could have cross-linked to generate the organic polymers found within extra terrestrial bodies (Potiszil et al. 2017). About 50% of the carbon content of the interstellar matter is bound in a solid phase, most likely an amorphous form of solid carbon, and additionally up to 10% of the carbon is in large polycyclic aromatic hydrocarbons(PAHs) (e.g. Mathis et al., 1977; Kwok, 2004; Matrajt et al., 2005). Polycyclic aromatic hydrocarbons (PAHs) have been observed in carbonaceous chondrites and primitive chondrites due to their volatile element enrichment (Basile et al., 1984; Allamandola et al., 1987; Botta and Bada, 2002). However, PAHs are the most abundant free organic molecules in the interstellar medium (d'Hendecourt and Ehrenfreund, 1997; Ehrenfreund and Charnley, 2000). The analyses of PAHs and the insoluble organic component within meteorites show that there are extensive amounts of polycyclic aromatic sheets present in the material (Cronin et al., 1987; Messenger, 2000). More than 70 % of the carbon in the Murchison and Orgueil meteorites has been identified to be aromatic (Gardinier et al., 2000), PAHs have been identified as the insoluble organic component (Alexander et al., 2007), and the vibrational spectra of these compounds have been extensively studied.

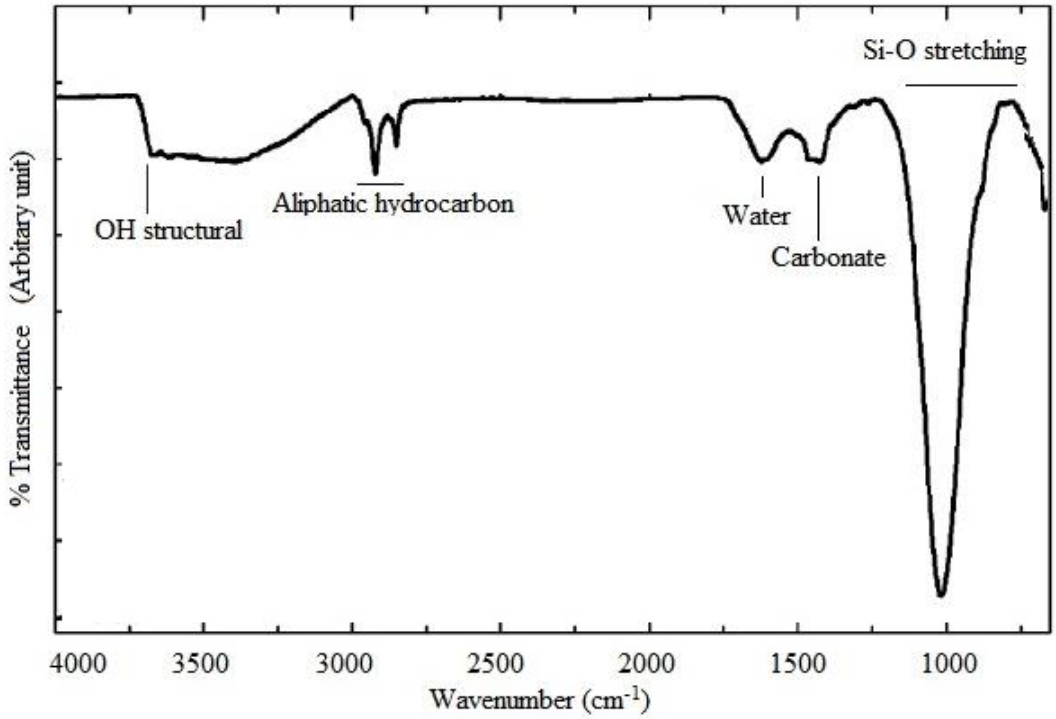

Figure 1. A schematic infrared spectrum in the 4000−1000 cm^{-1} region showing general appearances of Si-O stretching, water stretching, structural OH stretching, the carbonate component and the aliphatic stretching component

A general feature of mid infrared spectrum is shown in the Figure 1. The aromatic peaks can be observed in the 650−900 cm^{-1} and 1400−1650 cm^{-1} region. The Si–O stretching is commonly observed at ~1000 cm^{-1}. The 2700−3100 cm^{-1} region is characterized as C–H stretches of aliphatic hydrocarbons. The water stretching can be observed at ~ 1615-1620 cm^{-1} and the structural OH stretching is observed at ~ 3660−3670 cm^{-1}. The carbonate component is commonly represented by a broad band centered at ~1450 cm^{-1}. The aliphatic stretching component is represented by the group of peaks in the 2700−3000 cm^{-1} region. In the mid infrared region, Salisbury et al. (1992) and Socrates (2001) observed the infrared bands of organic compounds in meteorites; their infrared interpretations of organic bands are summarized in Table 1 (Salisbury et al.,1992; Socrates, 2001). An analysis of Dergaon and Natun Balijan using mid-infrared spectroscopy are presented here in order to facilitate an understanding the relative nature and characterized the aliphatic functional CH_2 and CH_3 groups in the spectral region around 2700-3000 cm^{-1} (3.4μm region) of ordinary chondrite.

The mid-infrared spectrum of Dergaon and Natun Balijan in the spectral region 4000-400 cm^{-1} is shown in Figure 2. The spectra reveals a number of absorption bands in the 10μm (800-1150cm^{-1}) and 20μm (400-700cm^{-1}) region which indicates the presence of silicate minerals. Prominent peaks in the in 10μm and 20μm region of infrared spectra correspond to the characteristics band of olivine group originated from the valance vibrations of SiO_4 tetrahedra.

Table 1. Some possible infrared interpretations of organic bands found in meteorites (after Salisbury et al., 1992 and Socrates, 2001).

Wavenumber (cm^{-1})	Possible Interpretations
679	carbonate
740	carbonate/branched alkane
842	carbonate/straight chain alkane
880	carbonate/aliphatic
650-900	out-of-plane CH bending deformation due to aromatics
1017	Si-O stretch due to phyllosilicate
1266	CH_3 of aliphatic hydrocarbon
1315	bending CH_3 due to aliphatic hydrocarbon
1353	bending CH_3 due to aliphatic hydrocarbon
1379	bending symmetric CH_3 due to aliphatic hydrocarbon
1424	C=C stretchingdue to aromatic/carbonate
1466	bending asymmetric CH_3 due to aliphatic/carbonate
1503	carbonate
1320-1530	broad band centred at ~1450 due to carbonate
1602; 1615	H-O-H stretching of water/phyllosilicate
1624	C=C stretching due to aromatic/alkene
1700	C=O stretching due to saturated aliphatic ketone/ carboxylic acid
2851	stretching symmetric CH_2 due to aliphatic hydrocarbon
2865	stretching symmetric CH_3due to aliphatic hydrocarbon
2922	stretching asymmetric CH_2 due to aliphatic hydrocarbon
2958	stretching asymmetric CH_3 due to aliphatic hydrocarbon
3623-3680	free OH/water
3668	structural hydroxyl feature/phyllosilicate

The trace around 3600-3700 cm^{-1} region arises due to O-H stretching of structural hydroxyl features of phyllosilicates. Generally, OH groups reside at the octahedral surface of the layers and forms weak hydrogen bonds with the oxygen of the Si-O-Si bonds on the lower surface of the octahedral plane (Madejova and Komadel, 2001). Moreover, the presence of very week band at ~1650 cm^{-1} is attributed to H-O-H bending vibration. Another moderate peak is correspondingly observed at 3430 cm^{-1} and 3441-3449 cm^{-1} in both spectra, indicating to the presence of dissolved volatile species.

The organic aliphatic C-H stretching features in meteorites have been reported in many literatures (e.g. Socrates, 2001; Martins, 2011). The C-H bending vibrations of aliphatic hydrocarbons are generally observed at ~1466 cm^{-1} and ~1379 cm^{-1}, these peaks are not observed in the infrared spectrum of Natun Balijan. However, the C-H bending vibrations are observed in Dergaon spectrum at 1376 cm^{-1} and 1451-1462cm^{-1}.

Generally, three stretching features of aliphatic hydrocarbon are found in the region 2700-3000 $cm^{-1}$of infrared specturm. The first pair of peaks at 2922 cm^{-1} and 2851 cm^{-1} corresponds to the asymmetrical and symmetrical stretching vibrations of CH_2 in an aliphatic hydrocarbon. The second peaks at 2958 cm^{-1} and 2865 cm^{-1} correspond to the asymmetrical and symmetrical stretching vibrations of CH_3 in an aliphatic hydrocarbon (Flynn et al., 2004; Matrajt et al., 2004).

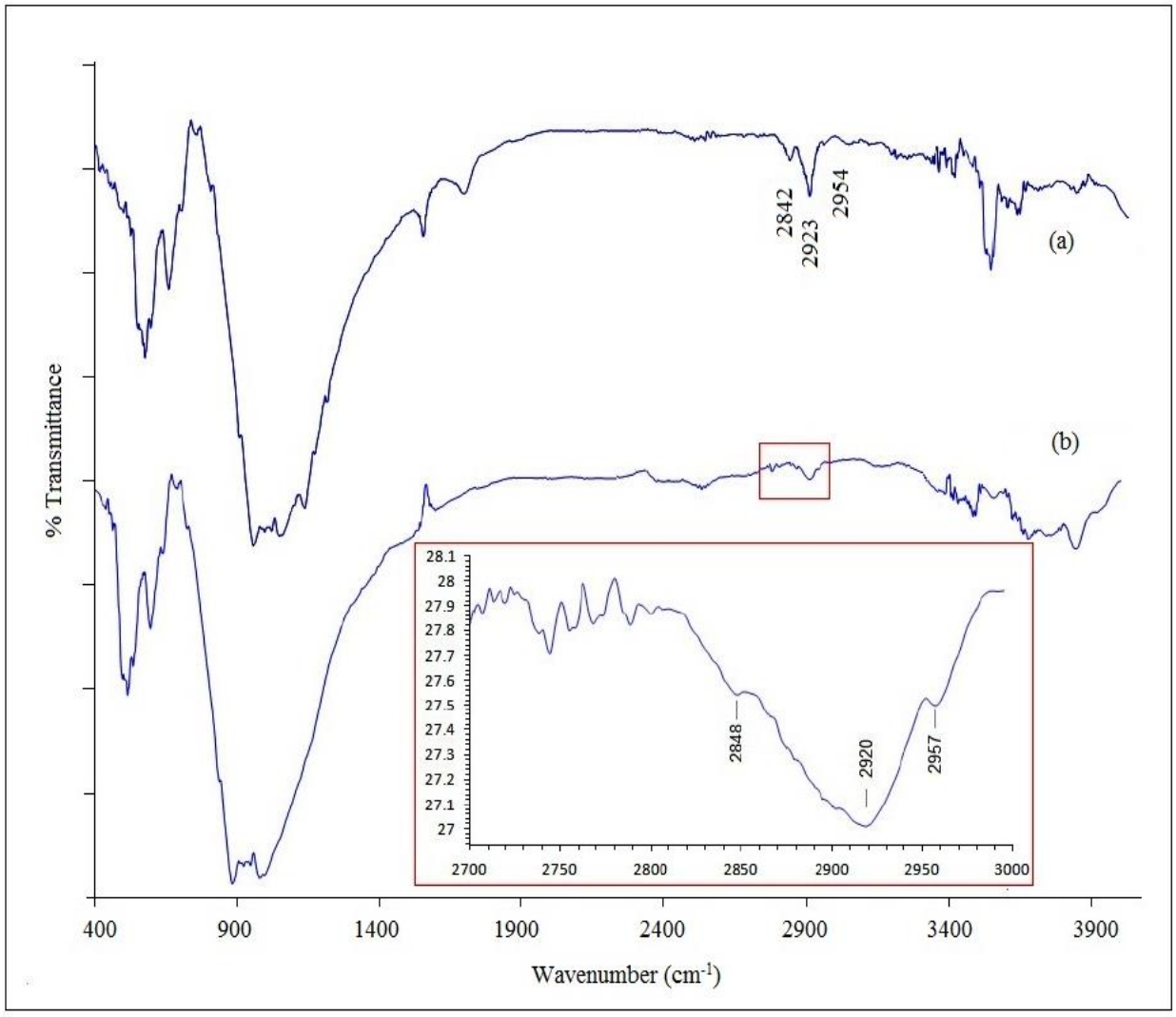

Figure 2. The infrared spectra of (a) Dergaon H5 chondrite and (b) Natun Balijan L4 chondrite in the spectral region 400-4000 cm^{-1}, C-H features is recorded in 2800-3000 cm^{-1} region of both meteorites. Inset shows 2800-3000 cm^{-1} region of Natun Balijan meteorite.

The sub-features of both symmetric and anti symmetric C–H stretching vibrations of $–CH_2–$ and $–CH_3$ of aliphatic entitles with C–C single bond. At room temperature, the mid-infrared spectrum of Dergaon and Natun Balijan, shows weak absorptions feature of C-H stretching bands in the range 2842–2957 cm^{-1} which indicates polyatomic entitles with C bonded to two or three H. The strongest νCH band in the range 2920–2923 cm^{-1} assigned to symmetrical stretch of C–H mode of $–CH_2–$ group. The bands found in between 2842–2848 cm^{-1} is assigned to anti symmetrical stretch of $–CH_2-$ group. The infrared spectrum exhibits another band in the range 2954–2957 cm^{-1} which is due to the symmetric stretch of $–CH_3$ group. The infrared spectrum of Dergaon and Natun Balijanin the range 2700-3000 cm^{-1} is shown in Figure 2.

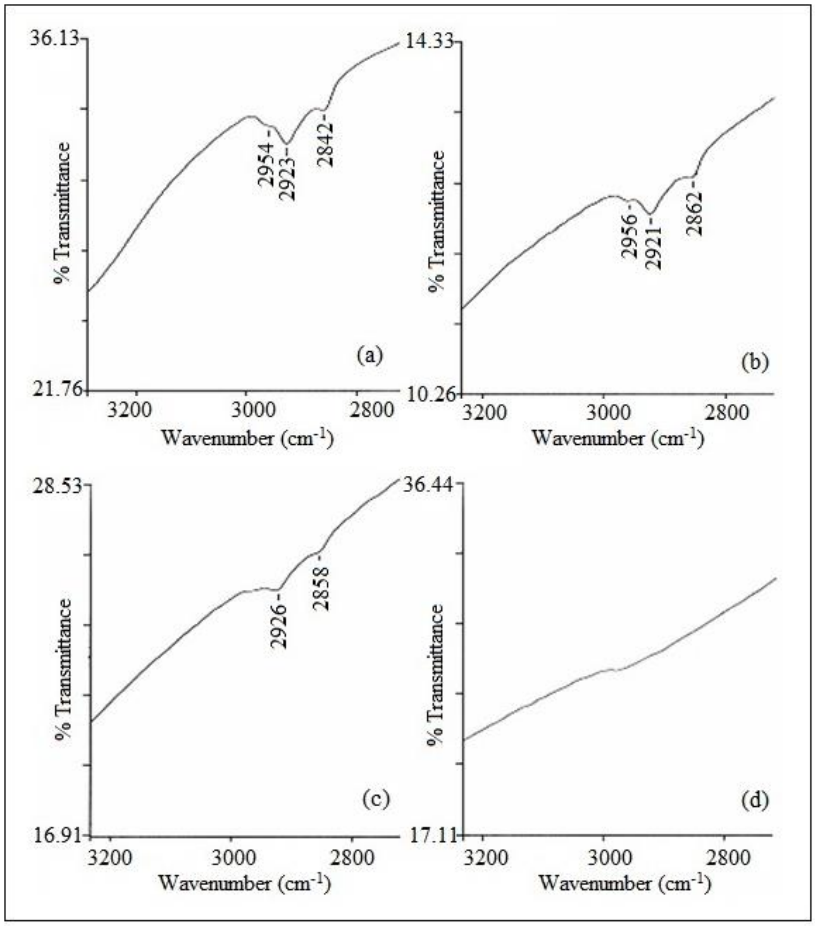

Figure 3. The infrared spectra in the 2700–3000 cm^{-1} region exhibit aliphatic hydrocarbon features in the Dergaon H5 chondrite. The infrared spectra demonstrate the change of peak positions with temperature, (a) at room temperature (29ºC), (b) heating at a constant temperature of 80ºC for 24 hours, (c) heating at a constant temperature of 80ºC for 48 hours, and (d) heating at a constant temperature of 80ºC for 72 hours. The spectra show the variation of peak intensities with time.

Table 2. The infrared band positions in 2700–3000 cm^{-1} (3.4 μm) region of the Dergaon H5 chondrite and their possible assignments.

Sample	Wavenumber (cm^{-1})	% Transmission	Intensity	Assignments
At room temperature	2954	33.0165	0.48127	CH_3 stretching vibration
	2923	31.8190	0.49313	CH_2 stretching vibration
	2842	33.2560	0.47813	CH_2 symmetric stretch
Heated at 80°C for 48 hours	2956	12.4985	0.90314	CH_3 stretching vibration
	2921	12.3628	0.90788	CH_2 stretching vibration
	2862	12.7698	0.89382	CH_2 symmetric stretch
Heated at 80°C for 48 hours	2926	24.9472	0.60298	CH_2 stretching vibration
	2858	25.8187	0.58807	CH_2 symmetric stretch

The variation of the peak intensity in the region 2700 – 3000 cm^{-1}region of the infrared spectra of these meteorites are observed by heating the pellet at a constant temperature 80°C with a time interval of 24 hours. The intensity of the peaks shows a discrepancy with time. On heating at this constant temperature for 48 hours, a significant change is observed in the CH_3 stretching vibrations around 2954-2956 cm^{-1}. The changes in infrared peaks of CH_3 stretching vibration region is shown in Figure 3 and their possible assignments are listed in Table 2. On further heating the pellets at that constant temperature (80°C) for another 24 hours, the bands of this region are disappeared. However, no significance change is observed in the Si-O stretching and bending regions due to this heat treatment. This weak absorption features in 2700 – 3000 cm^{-1}region of Dergaon and Natun Balijan, are indicative to the presence of organic compounds. Lawless et al. (1972) observed similar features observed in other H chondrites (Lawless et al.1972). Generally stretching features of aliphatic hydrocarbon are not observed in the meteorite of H types. However, the weathering of the meteorite sample cannot be overlooked for presence of these features. The infrared spectroscopic results provide the evidence for the possible existence of organic compounds in Dergaon and Natun Balijan chondrites. Further work on phase stability of C-H stretching region and nature of weathering are necessary for complete understand the presence of these phases in these chondrites.

Nanodiamonds in ordinary chondrites

Diamond is abundant in space, IDPs, meteors, and it exists inside the planets. The existence of interstellar or presolar nanodiamonds in the interstellar medium was first predicted by Saslaw and Gaustad in 1969s. (Saslaw and Gaustad, 1969). Lewis et al. (1987) first recognized the presolar nanodiamonds in meteorites (Lewis et al., 1987). The presolar diamonds are only a few nanometers in diameter; hence the term "nanodiamonds" was introduced. The extraterrestrial diamonds exist in different sizes (e.g. the mean crystallite sizes of these nanodiamonds are of the order of 1 to 3 nm) and they have different origins (Scott, 1972; Messenger, 2000; Norton, 2002; Busemann et al., 2006; Briani et al., 2009). Thus far, more than ten different minerals from primitive meteorites have been identified as presolar (Nittler, 2003). Nanodiamonds were recognized as presolar because of the isotopically anomalous noble gases that they contain, and the primitive chondritic meteorites contain up to ~1500 ppm of nano diamonds (Huss et al, 2006). The mechanism of the formation of diamonds is supposed to be mostly a chemical vapour deposition (CVD) process, which implies that they can be formed in the atmosphere of any star in which C/O > 1(Daulton et al., 1996). It is important that some stars are made of diamond. Madhusudhan et al. (2012) has proposed a diamond planet—"super earths" 55 Cancri e (eight times the mass of the earth and twice as the earth's radius in size)—with composition C/O = 1.12, which supports the presence of a carbon-rich environment in the planetary system (Madhusudhan et al., 2012). Nanodiamonds have been identified spectroscopically in a few stars, one of which HR 4049 is at the post-AGB phase of evolution (Winckel, 2003; Giridhar, 2011). Moreover, these presolar particles such as diamond, graphite, SiC, Al_2O_3 etc., allow us to understand the processes in stars and in interstellar regions. Carbon in primitive chondritic meteorites is commonly present as an organic compounds and graphite (Gilmour, 2003). Diamonds in meteorites are first discovered in the stony Novo Urei meteorite in 1888, then in the iron Canyon Diablo meteorites (1891). The findings of diamonds in different meteorite types e.g. achondrites (ureilites: Novo Urei, Goalpara, and Havero), ordinary chondrites (Bishunpur and Krymka), carbonaceous chondrites (Allende, Tagish Lake, Orgueil, Murchison, and Renazzo), and iron meteorites (Canyon Diablo and Magura), are remarkable.

The discovery of these presolar nanodiamonds or presolar grains in carbonaceous chondrites gives us the possibility to analyse the matter of stars and interstellar medium in our laboratories. Raman spectroscopy of terrestrial carbonaceous matter is a well-established tool to determine the degree of metamorphism (Pasteris and Wopenka, 1991; Beyssac, 2002; Nasdala et al., 2004). The early findings of diamond in meteorites stimulated experimental shock investigations (DeCarli and Jamieson, 1961; Hough et al., 1995; Koeberl et al., 1997; Masaitis, 1998; El Goresy et al., 2001), and the existence of extraterrestrial diamonds in meteorites and carbonados has been discovered by spectroscopic methods (e.g. Huss, 1990; Koscheev et al., 2001; Parthasarathy et al., 2005; Garai et al., 2006; Gucsik et al., 2008, 2012; Haggerty, 2014). Carbon in ordinary chondrites has been generally found to consist of components such as graphite and diamond (Grady, 2000). These meteoritic carbons can be characterized by the broad first-order carbon characteristic D (diamond) and G (graphite) bands of Raman spectrum. A well separated D and G bands suggest the presence of the high ordered graphite phase. The properties of characteristic D and G bands peak positions and their intensities in the Raman spectra behaves as a function of the degree of ordering of the carbonaceous material. Several methods for treating

Raman spectra can be found in the literatures. We used Raman spectral parameters such as width at half maximum (FWHM-G, FWHM-D), peak position (ωG, ωD) and ratio of peak intensity (I_D/I_G) of the G and D bands for analysis.

The Raman spectra of nanodiamonds reveal two broad bands centred at ~1326 cm^{-1} and ~1590 cm^{-1}. The first-order Raman band (F_{2g}) of diamond occuring at ~1332 cm^{-1} corresponds to carbon sp3 bonding (the main C–C bond vibration in diamond) and the Raman band (E_{2g}) at ~1590 cm^{-1} is assigned to carbon sp2 bonding graphitic structures (Nasdala et al., 2004). Figure 4 displays different carbon phases observed in Raman spectra of Dergaon, Mahadevpur and Natun Balijan ordinary chondrites in the range 1100 – 2000 cm^{-1}. The relative intensities of the diamond peaks (I_D) at 1331–1349 cm^{-1} and the graphite peaks (I_G) at 1588–1618 cm^{-1} of these meteorite samples and their peak width, expressed as the full width at half maximum (FWHM) reflect the degree of ordering (El Goresy et al. 2001; Saikia et al. 2017).The best fit of the Raman spectra using a least-squares moving average trend to minimize background fluorescence was applied for FWHM measurement and the authentication of the result can be found from different shock metamorphic environments (El Goresy et al., 2001; Kenkmann et al., 2002; Gucsik et al., 2008; Saikia et al., 2017). In shock-induced diamonds, the value of FWHM is usually found in a range 10–120 cm^{-1} (Miyamoto, 1998). Measured FWHM value of Dergaon, Mahadevpur and Natun Balijan chondrites are correspondingly 120 cm^{-1}, 70 cm^{-1} and 17.5 cm^{-1}, which reflects the natures of shock metamorphism in these meteorites.

According to Wopenka et al. (2013), the intensity ratio of diamond (I_D) and graphite (I_G) peaks in graphitic carbon range fairly well in ordered graphite ($I_D/ I_G< 0.5$), disordered graphite ($0.51 < I_D/ I_G< 1.1$), and glassy carbon ($I_D/ I_G> 1.1$) (Wopenka et al., 2013). The I_D/I_Gratio corresponding to Dergaon, Mahadevpur and Natun Balijan chondrites are: ~1.121, ~1.075 and ~0.532, which implies disordered graphite and glassy carbon present in these meteorites.

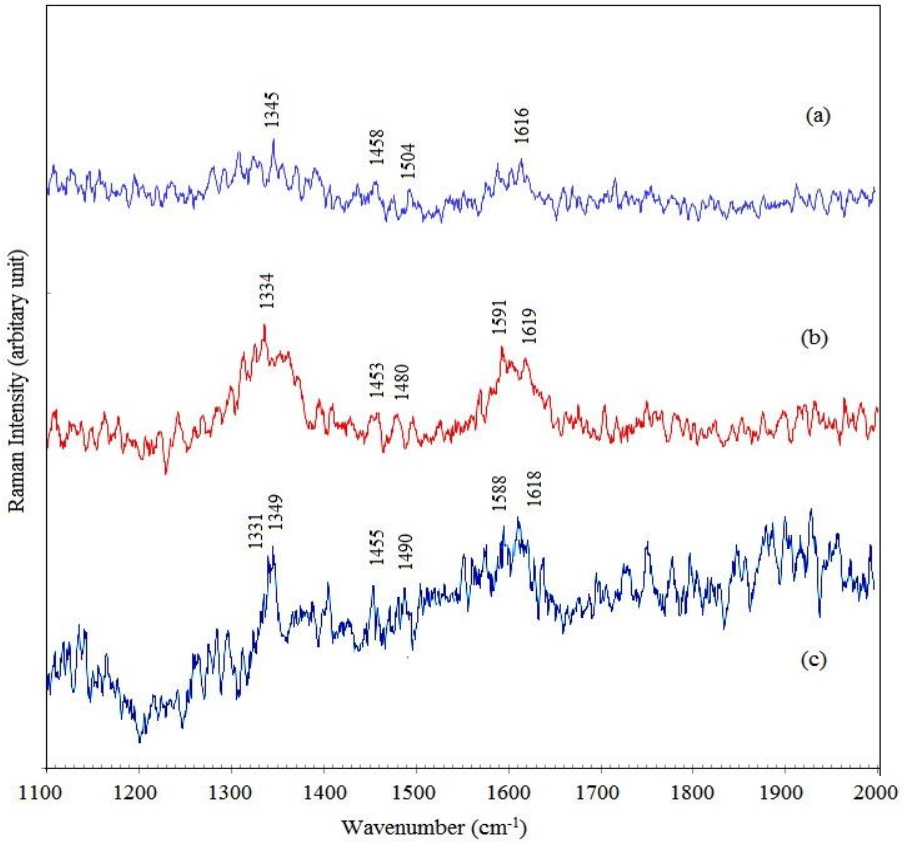

Figure 4. The Raman spectrum of a graphite nodule in (a) Dergaon H5, (b) Mahadevpur H4/5, and (c) Natun Balijan L4 chondrite samples showing two peaks, at ~1334–1349 cm^{-1} and a peak at ~1588–1618 cm^{-1}. The diamond peak appears at 1331 cm^{-1}. The peaks appear at ~1453–1458 $cm^{-1}$are significant to nanocrystalline diamond.

The presence of Raman peaks ~1616-1618 cm^{-1} is also evidence of disordered graphite in these meteorites (Figure 4). The Raman spectrum of Mahadevpur shows peaks at ~1334 cm^{-1} and 1591– 1619 cm^{-1} attributed to diamond and graphite (D and G carbon bands), respectively. Similar Raman peaks at 1331 cm^{-1}, 1349 cm^{-1} and 1588–1618 cm^{-1} are found for Natun Balijan. However, a moderate feature of D and G carbon bands has been observed in this region of the Raman spectrum of Dergaon. The intensity of peaks is generally used as a signature of crystalline quality. The peak intensities of these bands in these meteorites are relatively low, which indicates strong background fluorescence. This may be because of the amorphous nature of the sample or small grain size. In most cases, crystalline graphite can be identified by the dominance of the Raman band composed of merged peaks at around 1582 cm^{-1} and 1588 cm^{-1}(Kagi et al., 1991, 1994; Lapke et al., 2000), but owing to increasing disorder it moves to lower frequencies. Depending on the degree of disordering and orientation of the graphite grain, a second band around 1350 cm^{-1} and a shoulder at ~ 1620 cm^{-1} of lower intensity is present (Kagi et al., 1994). The Raman spectra of Dergaon exhibit the peaks at 1345 cm^{-1} and 1616 cm^{-1}, which can be explained by this disordered nature of graphite. Similar Raman peaks at 1349 cm^{-1} and 1618 cm^{-1} are observed in Natun Balijan. The relative intensities of the peaks (~ 1350 cm^{-1} and ~1620 cm^{-1}) reflects the degree of ordering or disordering in these meteorites. The shift of Raman peaks can also vary as a function of lattice stress, temperature and depends on the incident laser power (Miyamoto, 1998). Generally, the ~1350 cm^{-1} feature of the D band occurs because of Raman inactive A_{1g} mode, and it is activated only because of a finite crystal size (Filik et al., 2006). The presence of Raman peak at 1345 cm^{-1} and 1349 cm^{-1} in Dergaon and Natun Balijan respectively, are indicative of fine-grained carbon.

Both Raman spectra of Mahadevpur and Natun Balijan exhibit the peaks at 1334 cm^{-1} and 1331 cm^{-1} respectively, are accepted for diamond, such Raman peaks at ~1318–1333 cm^{-1} for apparently shock-produced diamond inside graphite nodules from Canyon Diablo were found by Miyamoto (1998) (Miyamoto, 1998). Diamond formation by chemical vapour deposition at low pressures and high temperatures is also possible in stellar atmospheres where the nanodiamonds of chondrites were generated (Ustinova, 2011). The artificially produced chemical vapour deposited nanocrystalline diamonds exhibits two significant bands at 1150 cm^{-1} and 1450 cm^{-1} (Brearley et al., 1989). The significant peaks at 1453 cm^{-1}, 1455 cm^{-1}, and 1458 cm^{-1} for Mahadevpur, Natun Balijan, and Dergaon respectively, are related to phonon modes with q_0, which are activated by the disorder induced by small grain sizes in nanocrystalline or amorphous diamond (Filik et al., 2006). Therefore, it may be believed that the formations of nanodiamonds in these chondrites are similar to this process (chemical vapour deposition).

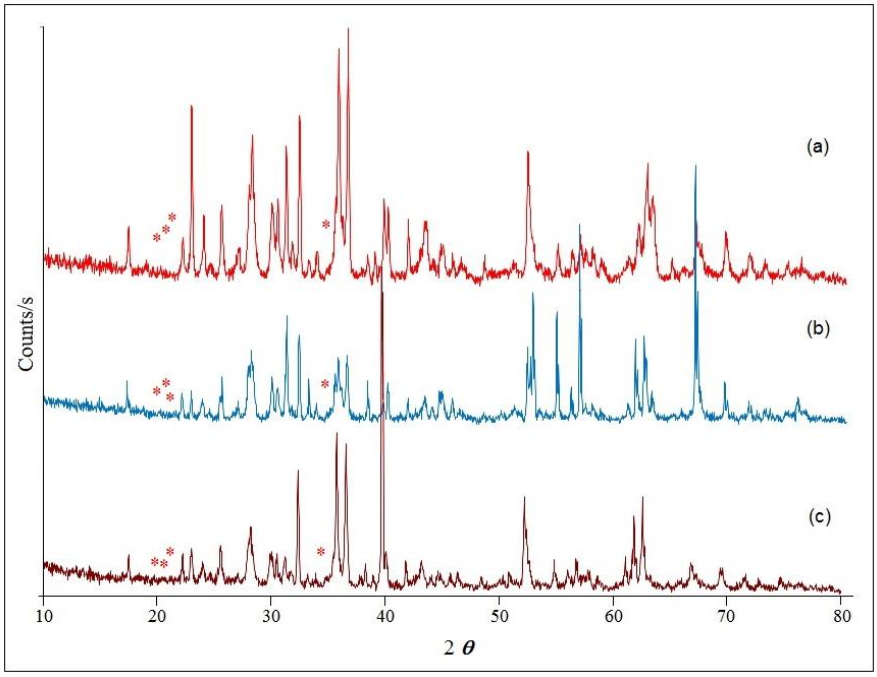

Figure 5. Powdered X- ray diffraction pattern of (a) Dergaon H5, (b) Mahadevpur H4/5, and (c) Natun Balijan L4 ordinary chondrites. The symbol indicates diamond phases.

Table 3. Powder X-ray diffraction data of observed diamond phases in the Dergaon (H5), Mahadevpur (H4/5) and Natun Balijan (L4) ordinary chondrites.

Dergaon (H5)		Mahadevpur (H4/5)		Natun Balijan (L4)		Assignment
d(nm)	*Intensity*	*d(nm)*	*Intensity*	*d(nm)*	*Intensity*	
0.219	10	0.219	27	0.218	40	H-diamond
0.206	10	0.204	26	0.206	40	diamond
0.192	14	0.193	17	0.194	22	H-diamond
0.126	8	0.126	11	0.125	10	diamond

Bhattacahrya and Dutta (2016) have reported shock-induced diamonds from ordinary chondritic meteorites (Bori Mirzapur, Kutppuram, and Chainpur) and proposed possible presence of ring woodite and lonsdalite with a Raman peaks at 1308, 1314, 1315, 1318, 1322, 1332, 1333, 1359, and 1360 cm^{-1} (Bhattacahrya and Dutta, 2016). However, the lonsdalite has been discredited as a distinct mineral phase, as it represents only twinned cubic diamond (Nemeth et al, 2014). Commonly, the X-ray diffraction (XRD) technique is used to determine the mineral abundances and classification of meteorites (Dunn et al., 2010). The powder XRD pattern collected for the studied meteorites are shown in Figure 5. Herein, we use XRD technique as a complementary tool for identification of diamond (Table 3). Conversely, for nanodiamond characterizations in meteorites, micro-Raman spectroscopy has proven to be much more powerful tool (Gucsik et al., 2008) as the grain size is very small. Moreover, the powder XRD technique has limitations in detecting traces of minor minerals, which occur as inclusions in olivine grains.

CONCLUSION

In the Raman spectra, the diamond and graphite (D and G carbon bands) peaks correspondingly observed at 1331-1349 cm^{-1} and 1588– 1618 cm^{-1} in Dergaon, Mahadevpur and Natun Balijan ordinary chondrites. The peak intensity of these peaks reflects the degree of ordering. The Raman peak position around 1616 cm^{-1} is the evidence of disordered graphite in these meteorite samples. The peak appears at 1331-1334 cm^{-1} is accepted for diamond. The Raman peak ~1450 cm^{-1} indicates the formation of nanodiamonds in these ordinary chondrites, which is similar to the chemical vapour deposition process. The full wave at half maximum value 120 cm^{-1}, 70 cm^{-1} and 17.5 cm^{-1} reflects the shock metamorphism in the meteorite samples. The diamond and graphite peaks intensity ratio ~1.121, ~1.075 and ~0.532, respectively indicates the disordered nature of graphite in Dergaon, Mahadevpur and Natun Balijan ordinary chondrites. The infrared analysis is consistent to the Raman spectroscopic results. The weak absorption bands found in 2700-3000 cm^{-1} of Dergaon and Natun Balijan are indicative to organic compounds. Infrared spectra indicate the presence of aliphatic hydrocarbons in the studied meteorites, which are essential in understanding of origin of hydrocarbons in meteorites.

ACKNOWLEDGEMENTS

The authors are grateful to Dr O.P. Pandey, Editor, for inviting this article. We thank Directors, Indian Institute of Technology, Guwahati (IITG) and North East Institute of Science and Technology (CSIR-NEIST), Jorhat for their support during this work. We also thank Dr. S. Sarmah, IIT Guwahati for his assistance in the spectroscopic analysis. GP is grateful to Indian National Science Academy, New Delhi, and National Institute of Advanced Studies, Indian Institute of Science, Bengaluru for their kind support and encouragement.

Compliance with Ethical Standards

The authors declare that they have no conflict of interest and adhere to copyright norms.

REFERENCES

Ahrens, T.J., 1990. in Origin of the Earth, Newsom, H. E. and Jones, J. H. (eds.), Oxford University Press, New York

Alexander, C.M.O'D., Russell, S.S., Arden, J.W., Ash, R.D., Grady, M.M. and Pillinger, C.T., 1998. The origin of chondritic macromolecular organic matter: a carbon and nitrogen isotope study.Meteorit. Planet. Sci., 33, 603-622.

Alexander, C.M.O'D., Fogel, M., Yabuta, H. and Cody, G.D., 2007. The origin and evolution of chondrites recorded in the elemental and isotopic compositions of their macromolecular organic matter. Geochim. Cosmochim. Acta., 71, 4380-4403.

Allamandola L.J., Sandford S.A. and Wopenka B., 1987. Interstellar polycyclic aromatic hydrocarbons and the carbon in interplanetary dust particles and meteorites. Science, 237, 56–59.

Allamandola, L.J., Sandford, S.A., Tielens, A.G.M., Herbst, T.M. 1992. Infrared spectroscopy of dense clouds in the C-H stretch region: Methanol and diamonds. Astrophys. J. 399, 134-146.

Basile, B.P., Middleditch, B.S. and Oró, J., 1984. Polycyclic aromatic hydrocarbons in the Murchison meteorite.Org. Geochem., 5, 211-216.

Bauschlicher, C.W. Jr., Liu, Y., Ricca, A., Mattioda, A.L. and Allamandola, L.J., 2007. Electronic and vibrational spectroscopy of diamondoids and the interstellar infrared brands between 3.35 and 3.55μm. Astrophys. J., 671, 458-469.

Becker, L., Bunch, T.E. and Allamandola, L.J., 1999. Higher fullerenes in the Allende meteorite. Nature, 400, 227-228.

Beyssac, O., Rouzaud, J.N., Goffe, B., Brunet, F. and Chopin, C., 2002. Graphitization in a high-pressure, low-temperature metamorphic gradient: a Raman microspectroscopy and HRTEM study. Contrib. Mineral. Petrol., 143, 19–31.

Bhattacahrya, A. and Dutta, A., 2016. Raman spectroscopic studies of shock induced diamonds from ordinary chondritic meteorites. (abstract #2150), 47th Lunar and Planetary Science Conference.

Bonal, L., Quirico, E., Bourot-Denise, M. and Montagnac, G., 2006. Determination of the petrologic type of CV3 chondrites by Raman spectrscopy of included organic matter. Geochim. Cosmochim. Acta., 70, 1849–1863.

Bonal, L., Bourot-Denise, M., Quirico, E., Montagnac, G. and Lewin, E., 2007. Organic matter and metamorphic history of CO chondrites. Geochim. Cosmochim. Acta., 71, 1605–1623.

Botta, O. and Bada, J.L., 2002. Extraterrestrial organic compounds in meteorites. Surv. Geophys., 23, 411–465.

Bouvier, A. and Wadhwa, M., 2010. The age of the Solar System redefined by the oldest Pb-b age of a meteoritic inclusion. Nature Geosci.. 3, 637-641.

Brearley, A.J., 2003. Nebular and parent body processing. In: Davis, A.M. (Ed.), Meteorites, Comets and Planets, Elsevier-Pergamon, Oxford, 247-268.

Brearley, A.J., Scott, E.R.D., Keil, K., Clayton, R.N., Mayeda, T.K., Boynton, W.V. and Hill, D.H., 1989. Chemical, isotopic and mineralogical evidence for the origin of matrix in ordinary chondrites. Geochim. Cosmochim. Acta., 53, 2081–2094.

Briani, G., Gounelle, M., Marrocchi, Y., Mostefaoui, S., Leroux, H., Quirico, E. and Meibom A., 2009. Pristine extraterrestrial material with unprecedented nitrogen isotopic variation. Proc. Natl. Acad. Sci.. USA 106, 10522–10527.

Briggs, M.H. and Mamikunian, G., 1964. Organic constituents of carbonaceous chondrites. Life Sci. Space Res.. 2, 57-85.

Burbine, T.H., McCoy, T.J., Meibom, A., Gladman, B. and Keil, K., 2002. Meteoritic Parent Bodies: Their Number and Identification. In W. Bottke, A. Cellino, P. Paolicchi, & R. Binzel (Eds.), Asteroids IIITucson: University of Arizona Press, 653-667.

Busemann, H., Young, A.F., Alexander, C.M.O'D., Hoppe, P., Mukhopadhyay, S., Nittler and L.R., 2006. Interstellar chemistry recorded in organic matter from primitive meteorites. Science, 312, 727-730.

Busemann, H., Alexander, C.M.O'D. and Nittler, L.R., 2007. Characterization of insoluble organic matter in primitive meteorites by microRaman spectroscopy. Meteorit. Planet. Sci., 42, 1387-1416.

Busemann, H., Nguyen, A.N., Cody, G.D., Hoppe, P., Kilcoyne, A.L.D., Stroud, R.M., Zega, T.J. and Nittler, L.R., 2009. Ultra primitive interplanetary dust particles from the comet 26P/ Grigg-Skjellerup dust stream collection. Earth Planet. Sci. Lett., 288, 44–57.

Cassen, P. and Boss, A.P. 1988, in Meteorites and the Early Solar System, Kerridge, J. F. and Matthews, M. S. (eds.), University of Arizona Press, Tucson.

Consolmagno, G.J., Britt, D.T. and Macke, R.J., 2008. The significance of meteorite density and porosity. Chemie der Erde-Geochemistry, 68, 1–30.

Cooper, G.W. and Cronin, J.R., 1995. Linear and cyclic aliphatic carboxamides of the Murchison meteorite: hydrolysable derivatives of amino acids and other carboxylic acids,Geochim. Cosmochim. Acta., 59, 1003-1015.

Cooper, G.W., Onwo, W.M. and Cronin, J.R., 1992. Alkyl phosphonic acids and sulfonic acids in the Murchison Meteorite. Geochim. Cosmochim. Acta., 56, 4109-4115.

Cooper, G., Kimmich, N., Belisle, W., Sarinana, J., Brabham, K. and Garrel, L., 2001. Carbonaceous meteorites as a source of sugar-related organic compounds for the early Earth. Nature, 414, 879-883.

Cronin J.R. and Pizzarello S., 1990. Aliphatic hydrocarbons of the Murchison meteorite. Geochim. Cosmochim. Acta, 54, 2859–2868.

Cronin, J.R. and Moore, C.B., 1976. Amino acids of the Nogoya and Mokoia carbonaceous chondrites, Geochim. Cosmochim. Acta, 40, 853–857.

Cronin, J.R., Pizzarello, S., and Gandy, W.E., 1979. Amino acid analysis with o-Phthalaldehyde detection: Effects on reaction temperature and thiol on fluorescence yields. Anal. Biochem., 93, 174-179.

Cronin J.R., Gandy W.E., and Pizzarello S., 1981. Amino acids of the Murchison meteorite: 1. 6 carbon acyclic primary alpha-amino alkanoic acids, J. Molec. Evol., 17, 265–272.

Cronin, J.R., Pizzarello, S. and Frye, J.S., 1987. C-13 NMR-spectroscopy of the insoluble carbon of carbonaceous chondrites. Geochim. Cosmochim. Acta, 51, 299-303.

Cronin, J.R., Pizzarello, S. and Cruikshank, D.P., 1988. Organic matter in carbonaceous chondrites, planetary satellites, asteroids and comets. In: Kerridge, J.F., Matthews, M.S. (Eds.), Meteorites and the Early Solar System, The University of Arizona Press, Tucson, 819-857.

Cronin, J.R. and Chang, S., 1993. Organic matter in meteorites: molecular and isotopic analysis of the Murchison meteorite. In Greenberg, J. M. (Eds) The Chemistry of Life's Origins. Kluwer, Boston, 209–258

Cronin, J.R., Pizzarello, S., Epstein, S. and Krishnamurthy, R.V., 1993. Molecular and isotopic analyses of the hydroxyacids, dicarboxylic-acids, and hydroxydicarboxylic acids of the Murchison meteorite. Geochim. Cosmochim. Acta, 57, 4745-4752.

d'Hendecourt, L. and Ehrenfreund, P., 1997. Spectroscopic properties of polycyclic aromatic hydrocarbons (PAHs) and astrophysical implications., Adv. Space Res., 19, 1023-1032.

Daulton, T.L., Eisenhour, D.D., Bernatowitz, T.J., Lewis, R.S. and Buseck, P.R., 1996. Genesis of presolar diamonds: Comparative high-resolution transmission electron microscopy study of meteoritic and terrestrial nano-diamonds. Geochim. Cosmochim. Acta, 60, 4853-4872.

DeCarli P.S. and Jamieson J.C., 1961. Formation of diamond by explosive shock. Science, 133, 1821–1822.

Derenne, S., and Robert, F., 2010. Model of molecular structure of the insoluble organic matter isolated from Murchison meteorite. Meteorit. Planet. Sci., 45, 1461–1475.

Dobrica, E.C., Engrand, E., Quirico, G., Montagnac and Duprat,J., 2011. Raman characterization of carbonaceous matter in CONCORDIA Antarctic micrometeorites. Meteorit. Planet. Sci., 46, 1363–1375.

Dunn, T.L., Gordon, C., Harry Y.M., and Timothy, J.M., 2010. Analysis of ordinary chondrites using powder X-ray diffraction:1. Modal mineral abundances. Meteorit. Planet. Sci., 45, 123–134.

Ehrenfreund, P. and Charnley, S.B., 2000. Organic molecules in the interstellar medium, comets, and meteorites: a voyage from dark clouds to the early Earth. Annu. Rev. Astron., 38, 427e483.

El Goresy, A., Gillet, P., Chen M., K¸nstler, F., Graup, G., and Stahle, V., 2001. In situ discovery of shock-induced graphite-diamond phase transition in gneisses from the Ries Crater, Germany. Am. Mineral., 86:611–621.

Engel, M.H. and Nagy, B., 1982. Distribution and enantiomeric composition of amino acids in the Murchison meteorite. Nature, 296, 837–840.

Epstein, S., Krishnamurthy, R.V., Cronin, J.R., Pizzarello, S. and Yuen, G.U. 1987. Unusual stable isotope ratios in amino acid and carboxylic acid extracts from the Murchison meteorite. Nature, 326, 477-479.

Frans, J.M.R., 2006. Natural Fullerenes and Related Structures of Elemental Carbon, Springer, Dordrecht, 299.

Filik, J., Harvey, N., Allan, N.L., May, P.W., Dahl, J.E.P., Liu, S. and Carlson, R. M. K., 2006. Raman spectroscopy of nanocrystalline dimond: An *ab intino* approach. Phys. Rev. *B*, 74, 035423-035433.

Flynn, G.J., Keller, L.P., Jacobsen, C. and Wirick, S., 2004. An assessment of the amount and type of organic matter contributed to the Earth by interplanetary dust. Adv. Space Res., 33, 57- 66.

Fraundorf, P., Walker, R.M. and Brownlee, D.E., 1982. Laboratory studies of interplanetary dust, In Comets (L. Wilkening, ed.), Univ. of Arizona, Tucson, 383–409.

Garai, J., Haggerty, S.H., Rekhi, S. and Chance, M., 2006. Infrared absorption investigations confirm the extraterrestrial origin of carbonado diamonds. Astrophy. J. Lett., 653, L153–L156.

Gardinier, A., Derenne, S., Robert, F., Behar, F., Largeau, C. and Maquet, J., 2000. Solid state CP/MAS 13C NMR of the insoluble organic matter of the Orgueil and Murchison meteorites: quantitative study. Earth. Planet. Sci. Lett., 184, 9–21.

Gillet, P., El Goresy, A., Beck, P. and Chen, M., 2007. High pressure mineral assemblages in shocked meteorites and shocked terrestrial rocks: Mechanisms of phase transformations and constraints to pressure and temperature histories. GSA Special Papers, 421, 57–82.

Gilmour, I., 2003. Structural and isotopic analysis of organic matter in carbonaceous chondrites, Meteorites, comets, and planets, edited by Davies A.M. Treatise on Geochemistry, vol. 1. Amsterdam: Elsevier, 269–280.

Giridhar, S. 2011. The progress in the study of post-AGB stars. ASI Conference Series, 3, 39 – 44

Grady, M.M., 2000. Catalog of Meteorites, 5th edition. Cambridge University Press, Cambridge UK.

Gucsik, A., Ott O., Marosits E., Karczemsk A., Kozanecki M. and Szurgot M., 2008. Micro-Raman study of nanodiamonds from Allende meteorite, Organic Matter in Space, 251, 335-339.

Gucsik, A., Nishido, H., Ninagawa, K., Ott, U., Tsuchiyama, A., Kayama, M., Simonia, I. and Boudou, J.P. 2012. Cathodoluminescence Microscopy and Spectroscopy of Micro- and Nanodiamonds: An Implication for Laboratory Astrophsyics. Microscopy and Microanalysis, 18, 1285-1291

Haggerty, S.E., 2014. Carbonado: Physical and Chemical properties, a critical evaluation of proposed origins, and a revised genetic model. Earth Sci. Rev., 130, 49-72.

Hiroi, T., Zolensky, M.E. and Pieters, C.M., 2001. The Tagish Lake meteorite: a possible sample from a D-type asteroid. Science. 293, 2234-2236.

Hough, R.M., Gilmour I., Pillinger C.T., Arden J.W., Gilkes K.W.R., Yuan J. and Milledge, H.J., 1995. Diamond and silicon carbide in impact melt rock from the Ries impact crater. Nature, 378, 41–44.

Huang, Y., Wang, Y., Alexandre, M.R., Lee, T., Rose-Petruck, C., Fuller, M. and Pizzarello, S., 2005. Molecular and compoundspecific isotopic characterization of monocarboxylic acids in carbonaceous meteorites, Geochim. Cosmochim. Acta, 69, 1073– 1084.

Huss, G.R., 1990. Ubiquitous interstellar diamond and SiC in primitive chondrites: Abundance reflect metamorphism, Nature, 347, 159–162.

Huss, G.R., Rubin, A.E., Grossman, J.N., 2006. Thermal metamorphism in chondrites, In: Lauretta, D.S., Mc Sween Jr., H.Y. (Eds.), Meteorites and the Early Solar System II. University of Arizona Press, Houston, 567-586.

Huss, G.R., and Lewis, R.S., 1995. Presolar diamond, SiC, and graphite in primitive chondrites: Abundances as a function of meteorite class and petrologic type. Geochim. Cosmochim. Acta, 59, 115-160.

Hutchison, R., 2004. Meteorites: a petrologic, chemical and isotopic synthesis, Cambridge: Cambridge Univ. Press.

Jenniskens, P, Laux, C.O., Packen, D.M., Wilson, M. and Fonda, M., 2000. Meteors as a vector for the delivery of organic matter to the early Earth. Earth, Moon Planets, 82-83, 57-70.

Kagi, H., Takahshi, K., Shimuzu, H., Kitajima, F. and Masuda, A., 1991. In situ micro Raman studies on graphitic carbon in some Antarctic ureilites, Proc. of the NIPR symposium on Antarctic meteorites, 4, 371–383.

Kagi, H., Tsuchida, I., Wakatsuki, M., Takahashi, K., Kamimura, N., Iuchi, K., and Wada, H., 1994. Proper understanding of downshifted Raman spectra of natural graphite: Direct estimation of laser-induced rise in sample temperature, Geochim. Cosmochim. Acta, 58:3527–3530.

Kenkmann, T., Hornemann, U., and Stöfler, D., 2002. Transformation of graphite to diamond in shock experiments: A Raman study. Lunar and Planetary Science Conference XXXIII, abs., 1052.

Koeberl, C., Masaitis, V.L., Shafranovsky, G.I., Gilmour, I., Langenhorst, F. and Schrauder, M., 1997. Diamonds from the Popigai impact structure, Russia. Geol., 25, 967–970.

Koga, T. and Naraoka, H., 2017. A new family of extraterrestrial amino acids in the Murchison meteorite, Sci. Rep., 7, 636.

Komiya, M., Naraoka, H., Mita, H. and Shimoyama, A., 2003. Amino acids and hydrocarbons in the Sayama and Antarctic Asuka carbonaceous chondrites (abstract), Proc. NIPR Symp. Antarct. Meteorites,p. 60. National Institute of Polar Research, Tokyo.

Koscheev, A.P., Gromov, M.D., Mohapatra, R.K. and Ott, U., 2001. History of trace gases in presolar diamonds inferred from ion-implantation experiments. Nature, 412, 615-617.

Kvenvolden, K., Lawless, J., Peterson, E., Flors, J., Ponnamperuma, C., Kaplan, I.R. and Moore, C., 1970. Evidence for extraterrestrial amino acids and hydro, Naturecarbons in the Murchison meteorite. Nature, 228, 923–936.

Kwok, S., 2004. The synthesis of organic and inorganic compounds in evolved stars. Nature, 430, 985–991.

Lapke, C., Schmitt, R.T., Kenkmann, T. and Stoffler, D., 2000. Raman microspectrometry of shocked graphite and impact diamonds from the Ries crater, Germany (abstract #1040), 31st Lunar and Planetary Science Conference.

Lawless, J.G., Kvenvolden K.A., Peterson, E., Ponnamperuma, C. and Jarosewich, E., 1972. Evidence for amino-acids of extraterrestrial origin in the Orgueil meteorite. Nature, 236, 66–67.

Lerner, N.R. and Cooper, G.W., 2005. Iminodicarboxylic acids in the Murchison meteorite: Evidence of Strecker reactions. Geochim. Cosmochim. Acta, 69, 2901–2906.

Lewis, R.S., Tang, M., Wacker, J.F., Anders, E. and Steel, E., 1987. Interstellar diamonds in meteorites. Nature, 326, 160-162.

Lodders, K. and Amri, S., 2005. Presolar grains from meteorites: Remnants from the early times of the solar system. Chem. Erde., 65, 93-166.

Love, S.G. and Brownlee, D.E., 1993. A direct measurement of the terrestrial mass accretion rate of cosmic dust. Science, 262, 550-553.

Madejova, J. and Komadel, P., 2001. Baseline studies of the clay minerals society source clays: Infrared methods. Clays Clay Miner., 49, 410-432.

Madhusudhan, N., Lee, K.K.M. and Mosis, O., 2012. A possible carbon-rich interior in super Earth 55 Cancri e. strophys. J. Lett., 759, 1–5.

Makjanic, J., Vis, R.D., Hovenier J.W. and Heymann, D., 1993. Carbon in the matrices of ordinary chondrites. Meteoritics, 28, 63–70.

Martins, Z., Watson, J.S., Sephton, M.A., Botta, O., Ehrenfreund, P. and Gilmour, I., 2006. Free dicarboxylic and aromatic acids in the carbonaceous chondrites Murchison and Orgueil. Meteorit. Planet. Sci. 41, 1073–1080.

Martins, Z., 2011. Organic Chemistry of Carbonaceous Meteorites, Elements, 7, 35-40.

Masaitis, V.L., 1998. Popigai crater: Origin and distribution of diamond-bearing impactites. Meteorit Planet Sci., 33, 349–359.

Mathis, J.S., Rumpl, W. and Nordsieck, K.H., 1977. The size distribution of interstellar grains. Astrophys. J., 217, 425-433.

Matrajt, G., Borg, J., Raynal, P.I., Djouadi, Z., d'Hendecourt, L., Flynn, G. and Deboffle, D., 2004. FTIR and Raman analyses of the Tagish Lake meteorite: Relationship with the aliphatic hydrocarbons observed in the Diffuse Interstellar Medium. Astron. Astrophys., 416, 983–990.

Matrajt, G., Muñoz, Caro, G.M., Dartois, E., D'Hendecourt, L., Deboffle, D. and Borg, J., 2005. FTIR analysis of the organics in IDPs: Comparison with the IR spectra of the diffuse interstellar medium. Astron. Astrophys., 433, 979–995.

McKinley, S., Scott, E.R.D., Taylor, G.J. and Keil, K., 1981. A unique type 3 chondrite containing graphite- magnetite aggregates Allan Hills A77011. Proc. Lunar Planet. Sci., 12B, 1039–1048.

McSween, Jr. H.Y., 1999. Meteorites and Their Parent Planets, Cambridge, New York.

Mennella, V., 2008. Activation of the 3.47 mm bond by H atom irradiation of carbon grains covered with a water ice layer at 12K, Astrophys. J. Lett., 682, L000.

Messenger, S., 2000. Identification of molecular-cloud material in interplanetary dust particles, Nature, 404, 968–971.

Misra, K.S., Hammond, M.R., Phadke, A.V., Plows, F., Reddy, U.S., Reddy, I.V., Parthasarathy, G., Rao, C.R.M., Gohain, B.N. and Gupta, D., 2007. Occurrence of fullerence bearing shungite suite rock in Mangampeta area, Cuddapah District, Andhra Pradesh. J. Geol. Soc. India, 69, 25–28.

Miyamoto M., 1998. Micro-Raman spectroscopy of diamonds in the Canyon Diablo iron meteorite: Implication for the shock origin. Antarct. Meteor. Res., 11, 171–177.

Montmerle, T., Augereau, J.C., Chaussidon, M., Gounelle, M., Marty, B. and Morbidelli, A. 2006. Solar System Formation and Early Evolution: the First 100 Million Years. Earth Moon Planets, 98, 39-95

Nasdala, L., Smith, D. C., Kaindl, R. and Zieman, M. A., 2004. In Spectroscopic methods in mineralogy. EMU Notes Mineralogy 6, edited by Beran, A. and Libowitzky, E. Eotvos University Press, pp. 281-343.

Nemeth, P., Garvie, A., Aoki, T., Dubrovinskaia, N., Dubrovinsky, L. and Buseck, P.R., 2014. Lonsdaleite is faulted and twinned cubic diamond and does not exist as a discrete material, Nat. Commun., 5. doi 10.1038/ncomms 6447.

Nittler, L.R. 2003. Presolar stardust in meteorites: Recent advances and scientific frontiers. Earth Planet. Sci. Lett., 209, 259–273.

Norton, O.R., 2002. The Cambridge Encyclopedia of Meteorites, Cambridge University, Cambridge.

Ott, U., 1993. Interstallar grains in meteorites, Nature, 364, 25-33.

Palme, H., 2000. Are there chemical gradients in the inner solar system?,Space Sci. Rev., 192, 237–262

Parthasarathy, G., Srinivasan, R., Vairamani, M., Ravikumar, K. and Kunwar, A.C., 1998. Occurrence of natural fullerenes in low grade metamorphosed proterozoic shungite from Karelia, Russia. Geochim. Cosmochim. Acta, 62, 3541–3544.

Parthasarathy, G., Bhandari, N., Vairamani, M. and Kunwar, A.C., 2008. High-pressure phase of natural fullerene C60 in iridium-rich Cretaceous–Tertiary boundary layers of Deccan intertrappean deposits, Anjar, Kutch, India, Geochim. Cosmochim. Acta, 72, 978–987.

Parthasarathy, G., Vairamani, M. 2011. Testing for fullerenes in geologic materials: oklo carbonaceous substances, karelian shungites, sudbury black tuff: comment and reply Geology, 31, e32-e33.

Parthasarathy, G., Haggerty, S. and Kunwar, A., 2005. Nano-Crystalline Osbornite from Carbonados: Spectroscopic Studies, Geochim. Cosmochim. Acta, 69(10) Supplement 521.

Pasteris, J.D. and Wopenka, B., 1991. Raman spectra of graphite as indicators of degree of metamorphism. Canad. Mineral., 29, 1–9.

Philip, A.B., Alex, W.R.B. and Tim Jull, A. J., 2000. Ancient Meteorite Finds and the Earth's Surface Environment. Quat. Res.**,** 53131-142.

Pirali, O., Vervloet, M., Dahl, J.E., Carlson, R, M.K., Tielens, A.G.G.M. and Oomens, J., 2007. Infrared spectroscopy of diamondoid molecules: New insights into the presence of nanodiamonds in the interstellar medium. Astrophys. J., 661, 919-925.

Pizzarello, S. and Cronin, J.R., 2000. Non racemic amino acids in the Murchison and Murray meteorites. Geochim. Cosmochim. Acta, 64, 329–338.

Pizzarello, S., Feng, X., Epstein, S. and Cronin, J.R., 1994. Isotopic analyses of nitrogenous compounds from the Murchison meteorite: Ammonia, amines, amino acids, and polar hydrocarbons. Geochim. Cosmochim. Acta, 58, 5579–5587.

Pizzarello, S., Cooper, G.W. and Flynn, G.J., 2006. Meteorites and the Early Solar System II, University of Arizona Press, Tucson, AZ.

Pizzarello, S., Huang, Y., Becker, L., Poreda, R.J., Nieman, R.A., Cooper, G. and Williams, M., 2001. The organic content of the Tagish Lake meteorite. Science, 293, 2236–2239.

Potiszil, C., Montgomery, W. and Sephton, M.A., 2017. Effects of Pressure on Model Compounds of Meteorite Organic Matter. ACS Earth Space Chem., 1, 475-482.

Quirico, E., Rouzaud, J.N., Bonal, L. and Montagnac, G., 2005. Maturation grade of coals as revealed by Ramanspectroscopy: Progress and problems. Spectrochim. Acta A, 61, 2368–2377.

Quirico, E., Montagnac, G., Rouzaud J.N., Bonal, L., Bourot Denise, M., Duber, S. and Reynard, B. 2009. Precursor and metamorphic condition effects on Raman spectra of poorly ordered carbonaceous matter in chondrites and coals. Earth Planet. Sci. Lett.. 287, 185–193.

Quirico, E., Bourot-Denise, M., Robin, C., Montagnac, G. and Beck, P., 2011. A reappraisal of the metamorphic history of EH3 and EL3 enstatite chondrites. Geochim. Cosmochim. Acta, 75, 3088–3102.

Quirico, E., Orthous-Daunay, F.R., Beck P., Bonal, L., Brunetto, R., Dartois, E., Pino, T., Montagnac, G., Rouzaud, J.N., Engrand, C. and Duprat, J., 2014. Origin of insoluble organic matter in type 1 and 2 chondrites: New clues, new questions. Geochim. Cosmochim. Acta, 136, 80–99.

Robert, F. and Epstein, S., 1982. The concentration and isotopic composition of hydrogen, carbon, and nitrogen in carbonaceous meteorites. Geochim. Cosmochim. Acta, 46, 81-95.

Saikia, B.J., Parthasarathy, G., and Sarmah, N.C., 2009a. Spectroscopic characterization of olivine[(Fe,Mg)2SiO4] in Mahadevpur H4/5 ordinary chondrite, Am. J. Sci., 5, 71–78.

Saikia B. J., Parthasarathy G. and Sarmah N. C., 2009b. Fourier transform infrared spectroscopic characterization of Dergaon H5 chondrite: Evedence of aliphatic organic compound. Nat. Sci., 7, 45–51.

Saikia, B.J., Parthasarathy, G. and Borah, R.R., 2017. Nanodiamonds and silicate minerals in ordinary chondrites as determined by micro-Raman spectroscopy. Meteorit. Planet. Sci., 52, 1146-1154.

Salisbury, J.W., Walter, L.S., Vergo, N., and D'Aria, D.M., 1992. Infrared (2.1−25 μm) spectra of minerals, The Johns Hopkins University.

Saslaw, W.C. and Gaustad, J.E., 1969. Interstellar dust and diamonds, Nature, 221, 160-162.

Schmitt-Kopplin, P., Gabelica, Z., Gougeon, R.D., Fekete, A. and Kanawati, B., 2010. High molecular diversity of extraterrestrial organic matter in Murchison meteorite revealed 40 years after its fall. PNAS, 107, 2763-2768.

Scott, E.R.D., 1972. Chemical fractionation in iron meteorites and its interpretation. Geochim. Cosmochim. Acta, 36, 1205–1236.

Scott, E.R.D., Brearley, A.J., Keil, K., Grady, M.M. and Pillinger, C.T., 1988. Clayton R.N., Mayeda T.K., Wieler R., and Signer P., Nature and origin of C-rich ordinary chondrites and chondritic clasts. Proc. 18th Lunar Planet. Sci. Conf., 513–523.

Sephton, M.A., 2002. Organic compounds in carbonaceous meteorites. Nat. Prod. Rep., 19, 292-311.

Shimoyama,A., Ponnamperuma, C. and Yanai, K., 1979. Amino acids in the Yamato carbonaceous chondrite from Antarctica. Nature, 282, 394-396.

Shimoyama,A., Naraoka, H., Harada, K. and Yamamoto, H., 1985. Carboxylic acid in the Yamato 791198 carbonaceous chondrite from Antarctica. Chem. Lett., 9, 1561-1564.

Smail, M., Claude, P., Ernst, Z. and Gerard, S., 2000. Metal-associated carbon in primitive chondrites: Structure, isotopic composition, and origin. Geochim. Cosmochim. Acta, 64, 1945–1964.

Socrates, G., 2001. Infrared and Raman characteristic group frequencies. (3rd ed.) Wiley and Sons.

Starkey N.A. and. Franchi, I.A., 2013. Insight into the silicate and organic reservoirs of the comet forming region. Geochim. Cosmochim. Acta, 105, 73–91.

Starkey, N.A. Franchi, I.A. and. O'd. Alexander, C.M., 2013. A Raman spectroscopic study of organic matter in interplanetary dust particles and meteorites using multiple wavelength laser excitation, Meteorit. Planet. Sci., 48, 1800–1822.

Thomas, K.L., Blanford, G.E., Keller, L.P., Klock, W. and Mckay, D.S., 1993. Carbon abundance and silicate mineralogy of anhydrous interplanetary dust particles. Geochim. Cosmochim. Acta, 57, 1551-1566.

Thomas, K.L., Keller, L.P., Blanford, G.E. and Mckay, D.S., 1994. Quantitative-analyses of carbon in anhydrous and hydrated interplanetary dust particles. Analysis of Interplanetary Dust, 165-172.

Ustinova, G.K. 2011.Production of anomalous Xe in nanodiamond in chondrites during the last supernova explosion predating the origin of the Solar System. Geochem. Int., 49, 555-567

Wang, D. and Chen, M., 2006. Shock-induced melting, recrystallization, and exsolution in plagioclase from the Martian lherzolitic shergottite GRV 99027. Meteorit. Planet. Sci., 41, 519–527.

Wang, A., Freeman, J.J., Jolliff, B.L. and Chou, I.-M., 2006. Sulfates on Mars: a systematic Raman spectroscopic study of hydration states of magnesium sulfates. Geochim. Cosmochim. Acta, 70, 6118–6135.

Wang, A., Kuebler, K.E., Jolliff, B.L. and Haskin, L.A., 2004a. Raman spectroscopy of Fe-Ti-Cr-oxides, case study: Martain meteorite EETA79001, Am. Mineral., 89, 665-680.

Wang, A., Kuebler, K., Jolliff, B. and Haskin, L.A., 2004b. Mineralogy of a Martian meteorite as determined by Raman spectroscopy , J. Raman Spectros., 35, 504-514.

Winckel, H.V., 2003. Post-AGB Stars. Annu. Rev. Astron. Astrophys., 41, 391–427

Wopenka, B., Xu, Y.C., Zinner, E. and Amari, S., 2013. Murchison presolar carbon grains of different density fractions: A Raman spectroscopic perspective. Geochim. Cosmochim. Acta, 106, 463–489.

Yabuta, H., Alexander, C.M.O.D., Fogel, M.L., Kilcoyne, A.L.D. and Cody, G.D., 2010. A molecular and isotopic study of the macromolecular organic matter of the ungrouped C2 WIS 91600 and its relationship to Tagish Lake and PCA 91008. Meteorit. Planet. Sci., 45, 1446–1460.

Received on: 09.01.2022; Revised on: 10.01.2022; Accepted on: 11.01.2022

GUIDE FOR AUTHORS

The Journal of Indian Geophysical Union (J-IGU), published bimonthly by the Indian Geophysical Union (IGU), is an interdisciplinary journal from India that publishes high-quality research in earth sciences with special emphasis on the topics pertaining to the Indian subcontinent and the surrounding Indian Ocean region. The journal covers several scientific disciplines related to the Earth sciences such as solid Earth geophysics, geology and geochemistry, apart from marine, atmosphere, space and planetary sciences. J-IGU welcomes contributions under the following categories:

- Research papers and short notes reporting new findings.
- Review articles providing comprehensive overview of a significant research field.

In addition, J-IGU also welcomes short communications, after communications and report on scientific activity, book reviews, news and views, etc.

The manuscript should be submitted electronically as a single word format (.doc file) including the main text, figures, tables, and any other supplementary information along with the signed "Declaration Letter". The manuscript should be submitted by email (jigu1963@gmail.com) to the Chief Editor.

After acceptance of the manuscript the corresponding author would be required to submit all source files (text and Tables in word format) and figures in high resolution standard (*.jpg, *.tiff, *.bmp) format. These files may be submitted to J-IGU as a single *.zip file along with the "Copyright Transfer Statement".

IMPORTANT INFORMATION

Ethics in publishing
J-IGU is committed to ensuring ethics in publication and takes a serious view of plagiarism including self-plagiarism in manuscripts submitted to the journal. Authors are advised to ensure ethical values by submitting only their original work and due acknowledgement to the work of others used in the manuscript. Authors must also refrain from submitting the same manuscript to more than one journal concurrently, or publish the same piece of research work in more than one journal, which is unethical and unacceptable. Editor of J-IGU is committed to make every reasonable effort to investigate any allegations of plagiarism brought to his attention, as well as instances that come up during the peer review process and has full authority to retract any plagiarized publication from the journal and take appropriate action against such authors if it is proven that such a misconduct was intentional.

Similarly, Editor and Reviewers are also expected to follow ethical norms of publishing by ensuring that they don't use any unpublished information, communicated to them for editorial or review purpose, in their own research without the explicit written consent of the author. They are also expected to keep manuscript/ data/ observations/ any other information related to the peer review confidential to protect the interest of the authors. Reviewers should refrain from reviewing the manuscripts in which they have conflicts of interest resulting from competitive, collaborative, or other relationships or connections with any of the authors, companies, or institutions connected to the manuscript.

Conflict of interest
All authors are requested to disclose any actual or potential conflict of interest including any financial, personal or other relationships with other people or organizations within three years of beginning the submitted work that could inappropriately influence, or be perceived to influence, their work.

Submission declaration
Submission of a manuscript implies that the work has not been published previously and it is not under consideration for publication elsewhere, and that if accepted it will not be published elsewhere in the same or any other form, in English or in any other language, without the written consent of the publisher. It also implies that the authors have taken necessary approval from the competent authority of the institute/organization where the work was carried out.

Copyright
After acceptance of the manuscript the corresponding author would be required to sign and submit the "Copyright Transfer Statement".

MANUSCRIPT PREPARATION

The corresponding author should be identified (include E-mail address, Phone/Mobile number). Full affiliation and postal address must be given for all co-authors.

Abstract:
An abstract of not more than 300 words must be included.

Text:
The manuscript should be structured to include a front page containing the title, Author(s) name, affiliation and address of the institute, where the work was carried out, a short title, and 5-to-6 Key words. Author(s) present address, if different from the above mentioned address, may be given in the footnote. The corresponding author should be identified with an asterisk and his/her email ID should be provided. This page should be followed by the main text consisting of Abstract, Introduction, Methods/ Techniques/ Area description, Results, Discussion, Conclusions, Acknowledgements, and References. Tables and Figures with captions should be inserted at the end of main text. It should not be inserted in the body of the text.

Figures/ Illustrations:
All figures should be provided in camera-ready form, suitable for reproduction (which may include reduction) without retouching. Figures in high-resolution (at least 300 dpi) standard formats (*.jpg, *.tiff, *.bmp) are acceptable. Figures should be numbered according to their sequence in the text. References should be made in the text to each figure. Each figure should have a suitable caption.

Tables:
Authors should take note of the limitations set by the size and layout of the journal. Table should not exceed the printed area of the page. They should be typed on separate sheets and details about the tables should be given in the text. Heading should be brief. Large tables should be avoided and may be provided as supplementary information, if required.

Equations:
Equations should be numbered sequentially with Arabic numerals and cited in the text. Subscripts and Superscripts should be set off clearly. Equation writing software that presents each equation as an object in MS Word will be accepted. Style and convention adopted for the equations should be uniform throughout the paper.

References:
All references to publications cited in the main text should be presented as a list of references in order following the text and all references in the list must be cited in the text. References should be arranged chronologically, in the text. The list of references should be arranged alphabetically at the end of the paper.

References should be given in the following form:
Kaila, K.L., Reddy P.R., Mall D.M., Venkateswarlu, N., Krishna V.G. and Prasad, A.S.S.S.R.S., 1992. Crustal structure of the west Bengal Basin from deep seismic sounding investigations. Geophys. J. Int., 111,45-66.

REVIEW PROCESS:

All manuscripts submitted to the journal are peer-reviewed. It is advisable to send the contact details of 4 potential reviewers along with the manuscript to expedite the review process. Editor has the option to select reviewers from the list or choose different reviewers. The review process usually takes about 3 months. All enquiries regarding the manuscript may be addressed to the Editor.

GALLEY PROOF:

Technical editing of manuscripts is performed by the editorial board. The author is asked to check the galley proof for typographical errors and to answer queries from the editor. Authors are requested to return the corrected proof within two days of its receipt to ensure uninterrupted processing. The editor will not accept new material in proof unless permission from the editorial board has been obtained for the addition of a "note added in proof". Authors are liable for the cost of excessive alterations to galley proof.

PUBLICATION CHARGES:

There are no page charges for publication and printing charges for b/w figures. However, in view of substantial cost involved in printing of color figures, author will be charged for printing of pages containing color figures @ Rs. 2,500/- per page. The charges may be revised at any time based on cost of printing and production. Author will receive an estimate/ invoice of the color figures reproduction cost along with the galley proof. It is the responsibility of the author to remit the color figures reproduction cost within one month of the receipt of the estimate/invoice.

The corresponding author will receive a soft copy (pdf format) of his/her published article. Should the author desire to purchase reprints of his/her publication, he/she must send the duly signed Reprint Order Form (accompanies the galley proof and contains price details) along with the corrected galley proof to the Editor. The reprint charges must be paid within one month of sending the Reprint Order Form.

Any payment related to printing of color figures and/or purchase of reprints should be made in the form of a Demand Draft in the name of Treasurer, Indian Geophysical Union, payable at Hyderabad.

You may download the pdf file from: http://www.j-igu.in/IGU-Guide-forAuthors.pdf